University of Strathclyde
Department of Physics

Micro-assembly of integrated photonic devices using a high accuracy transfer printing process

by

John McPhillimy

A thesis presented in fulfilment of the
requirements for the degree of
Doctor of Philosophy

August 2019

Declaration of authorship

This thesis is the result of the authors original research. It has been composed by the author and has not been previously submitted for examination which has led to the award of a degree.

Signed:

Date:

Abstract

The overall objective of this thesis is the development and implementation of a high accuracy transfer printing (TP) technique for the micro-assembly of integrated photonic devices. The method has particular relevance for the integration of hybrid photonic waveguides, and enables the production of passive/active photonic circuit technologies in a parallel and scalable manner.

The initial work involves the design of an optical microscopy based absolute cross-correlation alignment technique utilised within a custom-built TP system. Following this, the statistical characterisation of the method, with the measured absolute positional accuracy of fully fabricated devices integrated across multiple substrates is achieved. An absolute lateral alignment accuracy of $\pm$385 nm (3σ) and rotational accuracy of $\pm$4.8 mrad (3σ) are demonstrated. This is reported as the highest lateral alignment accuracy to date for transfer printing, lending itself a significant advantage for the micro-assembly of optical waveguiding components.

Utilising the high alignment TP system, the micro-assembly of fully fabricated single-mode Si membrane micro-ring resonators on a target silicon-on-insulator (SOI) substrate is presented. The ultra-thin membrane resonators are vertically integrated with Si bus waveguides situated on a receiver SOI chip in a highly controllable manner, demonstrating variation in resonant coupling conditions with respect to the lateral coupling offset. Further to this, the TP method provides a means to produce 3D device architectures without any limiting multi-step full wafer bonding methods. By vertical assembling 3D stacked membrane devices, a 100 μm^2 SOI distributed Bragg reflector (DBR) is produced taking advantage of high lateral and rotation placement accuracy. The structure exhibits a visible wavelength reflectance band in agreement with theoretical simulations.

The micro-assembly of hybrid AlGaAs-on-SOI micro-disk resonators is also presented, demonstrating the highly controlled integration of pre-fabricated waveguide devices across multiple material platforms. Control over the integrated resonator's vertical and lateral coupling to the bus waveguides enables the precise and selective excitation of different mode families within the resonator cavity. By using the high accuracy TP method, the vertical micro-assembly of hybrid micro-disk resonators also allows selective mode coupling, with loaded Q-factors reaching $\sim$40,000. The unique advantage of the assembled devices however come from the ability to perform $\chi^{(3)}$ nonlinear processes on SOI without being limited by two-photon absorption and free-carrier losses. Four-wave mixing is shown with efficiency levels of -25 dB at a low input power of 2.5 mW, with a nonlinear coefficient of 325 (Wm)$^-$1 demonstrated.

The measured nonlinearity is comparable to its monolithic silicon counterpart, whilst also detailing a clear reduction in the nonlinear losses inherent to this material platform.

Publications

Journals

1. John McPhillimy, Benoit Guilhabert, Charalambos Klitis, Martin Dawson, Marc Sorel, and Michael Strain, "High accuracy transfer printing of single-mode membrane silicon photonic devices", Opt. Express 26, 16679 (2018)

2. Benoit Guilhabert, John McPhillimy, Stuart May, Charalambos Klitis, Martin Dawson, Marc Sorel, and Michael Strain, "Hybrid integration of an evanescently coupled AlGaAs microdisk resonator with a silicon waveguide by nanoscale-accuracy transfer printing", Opt. Lett. 43, 4883 (2018)

3. D. Jevtics, A. Hurtado, B. Guilhabert, John McPhillimy, G. Cantarella, Q. Gao, H. H. Tan, C. Jagadish, M. J. Strain, and M. D. Dawson, "Integration of semiconductor nanowire lasers with polymeric waveguide devices on a mechanically flexible substrate, Nano Lett. 17, 5990 - 5994 (2017)

Conferences

1. John McPhillimy, Benoit Guilhabert, Charalambos Klitis, Stuart May, Martin Dawson, Marc Sorel, and Michael Strain, "High precision transfer printing for hybrid integration of multi-material waveguide devices", Advanced Photonics 2018 (IPR), July 2018, Zurich, Switzerland

2. John McPhillimy, Charalambos Klitis, Paul Hill, Stuart May, Benoit Guilhabert, Martin Dawson, Marc Sorel, and Michael Strain, "Towards 3D optical integration by micro-transfer printing of ultra-thin membrane devices", 2018 IEEE British and Irish Conference on Optics and Photonics (BICOP), Dec 2018, London, UK

3. John McPhillimy, Charalambos Klitis, Stuart May, Benoit Guilhabert, Martin Dawson, Marc Sorel, and Michael Strain, "High accuracy transfer printing of III-V/SOI micro-disk resonators for non-linear applications", ECIO, May 2019, Ghent, Belgium

4. Charalambos Klitis, Benoit Guilhabert, John McPhillimy, Stuart May, Ning

Zhang, Michael Strain, and Marc Sorel, "Heterogeneous Integration of Silicon And AlGaAs Micro-Ring Resonators by Transfer Printing", 2018 European Conference on Optical Communications (ECOC), Sep 2018, Roma, Italy

5. Benoit Guilhabert, Charalambos Klitis, John McPhillimy, Marc Sorel, Martin Dawson, and Michael Strain, "Nanoscale accurate heterogeneous integration of waveguide devices by transfer printing", 2018 IEEE Photonics Conference (IPC), Sept 2018, Reston, VA, USA

6. Antonio Hurtado, Dimitars Jevtics, Benoit Guilhabert, Joshua Robertson, John McPhillimy, Michael Strain, Fangfang Ren, Hoe Tan, Chennupati Jagadish, and Martin Dawson, "Transfer printing of semiconductor nanowire lasers for nanophotonic device fabrication", Smart Photonics and Optoelectronics Integrated Circuits XXI, March 2019, San Francisco, USA

Acknowledgments

Thank you!

To Michael Strain, who has been a great role model over the years. Your continuous encouragement has been a driving factor in this work, and I'm sure I'll always have something new and exciting to learn from you throughout my career.

To the staff within the Institute of Photonics, I'd like to thank you all for making the PhD so rewarding. This includes in particular Benoit Guilhabert for his invaluable experience, and James Sweeney for his continuous help and training in the cleanroom.

To all my PhD colleagues for both helping my research and making the experience incredibly enjoyable. I'd like to thank in particular Paul Hill, Dimitars Jevtics, and Marius Jankauskas who all started their PhD studies the same time as me and without which I'm sure the experience would have been a drag!

To all the researchers at University of Glasgow and James Watt Nanofabrication Centre who have played a key role in the PhD, especially Charalambos Klitis whose vital contribution has been paramount to the success of the work.

To Jennifer, thank you for everything. It wouldn't have been nearly as enjoyable an experience without you!

To my parents, who have just as much right over this PhD as I have with their unwavering mental and emotional support. Mike, Jim, and Andy...cheers guys. None of your support has gone unnoticed.

Contents

List of Figures

List of Tables

List of Abbreviations

A_{eff}	Effective Area
AFM	Atomic Force Microscope
AlGaAs	Aluminium Gallium Arsenide
ASE	Amplified Spontaneous Emission
BOX	Buried Oxide
CMOS	Complementary Metal Oxide Semiconductor
CW	Continuous Wave
DBR	Distributed Bragg Reflector
DFB	Distributed Feedback
DUV	Deep Ultra-Violet
EBL	Electron Beam Lithography
EDFA	Erbium Doped Fibre Amplifier
EM	Electro Magnetic
$\mathcal{F}$	Finesse
FCA	Free Carrier Absorption
FDE	Finite-Difference Eigenmode
FDTD	Finite-Difference Time-Domain
FOV	Field-Of-View
FSR	Free Spectral Range
FWHM	Full Width Half Maximum
FWM	Four Wave Mixing
GaAs	Gallium Arsenide
GUI	Graphical User Interface
HF	Hydroflouric
HSQ	Hydrogen Silsequioxane

ICP	Inductively Coupled Plasma
InP	Indium Phosphide
IR	Infrared
KOH	Potassium Hydroxide
LED	Light Emitting Diode
LS-PIC	Large Scale Photonic Integrated Circuit
MEMS	Micro Electro-Mechanical System(s)
Nd:YAG	Neodymium-doped Yttrium Aluminium Garnet
NIR	Near InfraRed
NW	NanoWire
OAM	Orbital Angular Momentum
OSA	Optical Spectrum Analyser
PDMS	Polydimethylsiloxane
PECVD	Plasma Enhanced Chemical Vapour Deposition
PIC	Photonic Integrated Circuit
PL	Photoluminescence
PMMA	Poly(methyl methacrylate)
Q-factor	Quality Factor
QIP	Quantum Information Processing
RGB	Red, Green, Blue
RIE	Reactive Ion Etching
ROC	Radius of Curvature
ROI	Region of Interest
SEM	Scanning Electron Microscope
SOI	Silicon-on-Insulator
SPDC	Spontaneous Parametric Down Conversion
Si	Silicon
SiO_2	Silicon Dioxide
TE	Transverse Electric
TIR	Total Internal Reflection
TM	Transverse Magnetic

TP	Transfer Printing
TPA	Two Photon Absorption
VCSEL	Vertical Cavity Surface Emitting Laser
VHF	Vapor Hydroflouric
WDM	Wavelength Division Multiplexing
WG	Waveguide
WGM	Whispering Gallery Mode

Chapter 1

Introduction

1.1 Role of optics in future information and communication technology

The expansion of the digital world is happening at a considerable rate in recent years, with billions of consumers alongside businesses and corporations collecting, sharing and storing massive amounts of information with the continuous pursuit of ever increasing performance levels [6]. This requirement for growth, combined with low power processing capabilities, has encouraged the production of more complex and dense multiprocessor chips. However, the interconnections between the sub-systems on-chip are starting to inhibit the continued system growth [7]. Many industrial companies are looking at new technologies to help increase bandwidths and reduce power consumption levels in order to keep up with current demands, with increasing focus on the development of chip-scale optical networks as a potential solution.

Optical fibre technology has already surpassed electronics with its use in long-haul communications [8]. As the performance requirements continue to increase, the use of optical technology has become prevalent for shorter and shorter links making use of optic's high bandwidth operation, capacity, and low power dissipation which has already made it such a key resource in long-haul transmission networks

[9]. With regards to achieving this, one of the current challenges in photonics is the development of power-efficient and high-speed chip-integrated optical devices [10], otherwise known as *photonic integrated circuits* (PICs).

1.2 Photonic integrated circuits

A PIC is an optical system integrating multiple optical/optoelectronic components onto a single platform for higher functionality, in a similar fashion to an electronic integrated circuit. Prior to PICs, optical systems typically consisted of discrete components communicating through point-to-point interconnections, using optical fibres to move information direct from transmitter to receiver. This approach satisfied low-level systems, however as the complexity and sophistication of system architectures increased alongside the performance requirements of current and predicted future networks, issues such as power consumption and scalability began to push networks to their limits.

The fundamental advantage of PIC architectures is the dense integration of optical components all into one common substrate, enabling the same scaling benefits in the manner of Moore's law for microelectronics to optical components helping increase performance levels. The implementation of many optical functions such as lasing, modulation, (de)multiplexing, and detection all into a single fibre-coupled platform can help address specific network scaling issues through the reduction of space and power requirements, simplifying the system design to improving reliability, all whilst reducing the overall system manufacturing costs [11]. The development of current PIC systems have already shown promise in applications ranging from multi-channel wavelength division multiplexing (WDM) [12], optical telecommunications [13], short-haul communications [14, 15], to lab-on-chip [16, 17]. Further to this,

the ability to merge PIC technology with electronics can be utilised to provide high functionality communications devices by taking advantage of the large data rates and high packing density of optical interconnects [18].

The manufacturing of PICs is still quite limited however, with one reason linked to the material systems' complexity. There has been large focus on both silicon and indium phosphide (InP) as promising platforms. An advantage of InP is that it can monolithically produce both passive and active components in the same substrate. One example of this being the production of PICs for extremely high data rate telecommunication networks with multi-Tb/sec capacities [19]. However, its lack of CMOS fabrication compatibility limits its manufacturing scalability and makes it an expensive option. There has also been a significant amount of interest with the use of silicon as a technology platform for future PICs.

1.2.1 Silicon PICs

Silicon-on-insulator (SOI) is a mature platform gaining a large amount of attention for its use in integrated photonics. This is partly due to its optical properties, with transparency across the telecommunications band (1270 nm - 1620 nm) due its indirect bandgap of 1.1 eV, along with its high refractive index contrast between the silicon and insulator cladding, 3.45 and 1.45 respectively. Such properties enable the production of highly compact and low-loss waveguide networks. Further to this, it exhibits a large $\chi^{(3)}$ nonlinear susceptibility, which when combined with the extremely small device footprint, can produce low power nonlinear effects [20]. SOI is also CMOS-compatible, therefore it can be manufactured at low cost and adapt easily to the current infrastructure in place for the production of high performance electronic systems-in-package. The fabrication of SOI large-scale PICs (LS-PICs) has

already been achieved with systems containing up to 12000 integrated optical devices, demonstrating a nano-antenna phased array for complex holographic imaging [21].

The realisation of most LS-PICs requires the dense integration of a wide range of both passive and active optoelectronic devices from multiple different platforms, with one example for applications into high data rate communication networks requiring a highly dense wavelength division multipling (WDM) passive system as well as active transmitter and receiver components [22]. The SOI platform has the capacity for nearly all optical functionalities specific to PIC systems offering an almost complete suite of optical components, including passive components such as filters, (de)multiplexers, splitters, and active components such as modulators and photodetectors [23]. However, silicon's inability to produce efficient light generation components, as well as its lack of $\chi^{(2)}$ nonlinearity inhibits the production of many important photonic components required for future LS-PICs. What is required is a platform with the passive component performance and CMOS fabrication of Si, whilst also providing the desirable active optics necessary for LS-PIC technologies. One method of achieving this is through heterogeneous integration of multiple optical materials.

1.3 Heterogeneous integration

Heterogeneous integration in photonics is the combination of two or more materials on a single chip, producing a hybrid platform incorporating the unique optical properties of each material. The technique has already been used for the production of hybrid silicon PIC technologies [24], with one example demonstrating the integration of Si and a III-V semiconductor material (InP) combining the passive component

performance of Si with the light generation capability of InP [25]. There are several different competing integration methods which are explained in this section: flip chip bonding, hetero-epitaxial layer growth, wafer bonding, and more recently, transfer printing.

1.3.1 Flip chip bonding

Flip chip bonding is the alignment and integration of two fully fabricated circuit systems, where one chip is flipped top-down and bonded in contact with a second chip. This can be achieved by wafer-to-wafer surface integration, or by aligning solder bumps and bonding pads with a final high temperature re-flow bonding each together. The integration method is a well-established procedure used throughout microelectronics and photonic systems. In microelectronics, it can be utilised to bond electronic chips and components components directly to external circuitry with micron scale accuracy [26]. Whilst in photonics, past research includes the integration of laser diode and VCSEL arrays with SOI PICs to produce multichannel, high density light sources [27, 28].

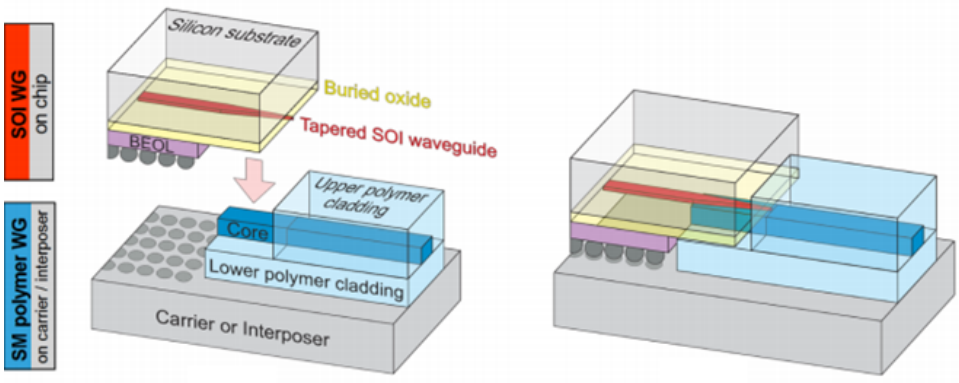

Figure 1.1: Schematic illustration of a waveguide flip chip assembly technique. With the schematics showing the structure (a) prior to assembly and (b) after assembly. From [1]

Flip chip bonding has the advantage that all devices are fabricated on their native platforms prior to integration, however requires precision alignment for efficient device integration. Further to this, having multiple solder bumps and bonding pads can account for a large chip-area limiting the achievable device packing density.

1.3.2 Hetero-epitaxial layer growth

Heteo-epitaxial integration involves the growth of non-native materials directly onto the main material platform, followed by subsequent fabrication steps to produce hybrid integrated components. Hetero-epitaxial growth allows for the front-end, wafer-scale integration of III-V materials onto SOI making it a potential method of producing hybrid PICs. The technique has previously been demonstrated for InP distributed feedback (DFB) laser arrays grown and fabricated directly onto the SOI platform without a buffer layer [2], as well as being widely used for the integration of NW lasers [29, 30].

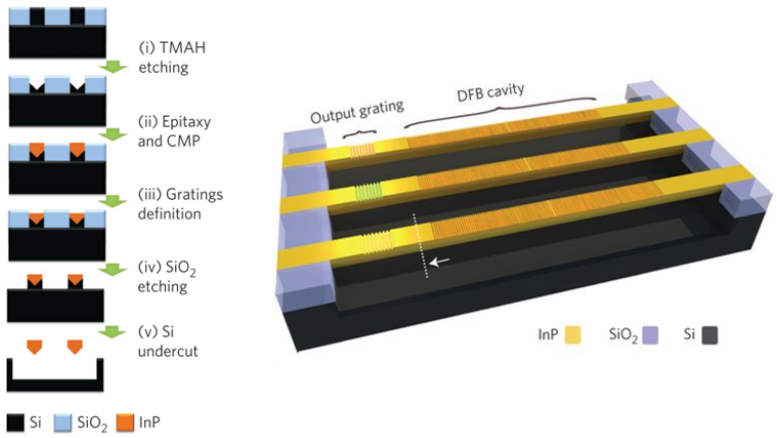

Figure 1.2: Schematic illustration of an epitaxial grown InP-on-Si laser and relevant fabrication process flow. From [2]

As the system is back-end processed, such that there includes fabrication after the material growth, the fabrication enables extremely high device alignment essential

for the facilitating of efficient coupling waveguiding devices. However, each specific hybrid platform requires its own growth process with many still in early development, with the manufacturing of high quality III-V layers onto silicon as well as the integration within current silicon foundries both on-going challenges.

1.3.3 Wafer Bonding

Wafer bonding is a method of integrating high quality III-V layer stacks from their native growth substrate to a receiver chip by the bonding of wafers prior to back-end processing. Either full wafer bonding, multiple die-to-wafer bonding, or individual die bonding can be achieved dependent on the component count and area of integration required, with multiple mechanisms used such as molecular [31], adhesive [32], anodic [33], and metallic bonding [34] depending on the material composition or specific requirements of the system. After the interface bond is achieved, the growth substrate will be removed followed by the fabrication of the desired components, figure 1.3.

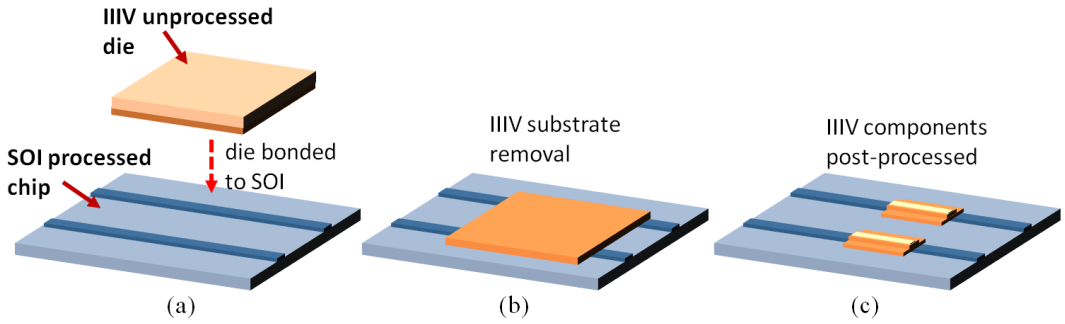

Figure 1.3: Schematic of a die-to-wafer bonding process; (a) an unprocessed III-V die is bonded to a fully processed SOI receiver; (b) the III-V growth substrate is removed; (c) device components are fabricated into the remaining III-V core layer, including any further fabrication steps i.e. metal deposition.

Wafer bonding has been used for the fabrication of a wide range of optical PIC components. Some of these include a hybrid III-V-on-Si nanolaser integrated for use

in on-chip data communications [35], to on-chip hybrid photodetectors [36], and the development of a III-V-on-Si transceiver for both chip-to-chip and on-chip optical interconnect technologies [37]. Although there has been successful development across a variety of state-of-the-art demonstrators, the technique has several issues with regards to large-scale manufacturing. Firstly, the method prohibits the dense co-integration of many different material layer structures at the same time onto a single SOI platform, with integrated wafers/die minimum dimensions in the millimetre-scale. Further to this, the final device fabrication is achieved post-bonding such that the technique is not compatible to full CMOS foundry processing.

1.4 Transfer Printing

Transfer printing (TP) is an integration method permitting the wafer-scale parallel assembly of micro/nanoscale devices across almost any material platform in a heterogeneous fashion. It was first developed by John Rogers group at the University of Illinois, with the desire to integrate thin-film flexible integrated electronic and optoelectronic circuits [38, 39]. Since then, it has been implemented for many device types spanning active nanomembrane laser sources [40], micro-LED displays [41], and photodetector technologies [42].

1.4.1 Transfer print procedure: advantages and challenges

The TP process involves the removal of coupons/devices from their donor material platforms, followed by the integration with pre-processed components situated on a receiver PIC in a wafer-scale parallel and scalable operation, as shown in figure 1.4. The device fabrication is achieved in a dense array on the native platform, with sparse integration of selected devices on the receiver cutting down on material wastage

and overall manufacturing costs. The availability to fully fabricated components on their native platforms prior to the printing procedure means the fabrication is not limited by wafer mechanical and chemical instabilities, as well as providing the ability to combine CMOS-compatible material platforms with non compatible materials. Further to this, the printable coupon sizes can vary from sub-micron up to mm-scale dimensions. TP is implemented through the use of an elastomeric stamp, adhering to the coupons and enabling the highly controllable pick-and-place across multiple substrates in a non-destructive manner. Specially designed stamps can pick-and-place either individual devices, or provide the parallel integration of many devices in a single operation [43], with the highly compact integration of devices spanning across many different material platforms possible. The advantages of TP depict it as a potential future technology for the development of wafer-scale PIC technologies for a wide range of applications.

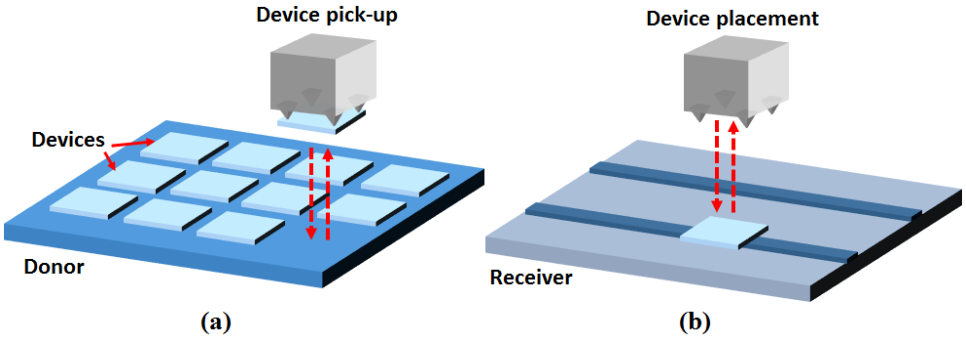

Figure 1.4: Schematic illustration of the transfer printing procedure. (a) Fully fabricated device is selectively picked up from donor chip using a PDMS elastomeric stamp. (b) Device is released from stamp and bonded to receiver chip, where it is coupled to pre-fabricated receiver components.

An open challenge for TP has been the realisation of passive/active waveguide PICs, requiring the ability to perform nanoscale device alignment as a means to efficiently couple integrated waveguiding devices, reducing losses through lower po-

sitional misalignment. The measure of transfer printing alignment accuracy is given by a device's relative misalignment from its expected printing position, which can be measured in both lateral and rotational dimensions. The alignment accuracy is typically measured by using an empirical (3σ) error based across a sample of repeated instances of printed device misalignments. The 3σ error is defined by the error band in which three standard deviations (σ) of the mean error value (μ) lies within, which is ≈99.7 % of all measured values. The standard deviation is given by:

$$\sigma = \sqrt{\frac{\sum |x - \mu|^2}{N}}, \tag{1.1}$$

where N is the total number of measured values. The 3σ error is an independent measurement for both lateral and rotational dimensions.

Current research groups have only demonstrated absolute alignment accuracy of devices limited to ±1.5 μm (3σ) [44]. So far, such waveguide coupled devices have required either post bonding fabrication processing steps to lithographically align structures [45], or the design of tapered couplers to decrease the necessary alignment tolerances [46]. A reliable TP method providing nanoscale device integration available to a wide range of device architectures without inhibiting CMOS fabrication is key in providing a solution to this challenge.

1.4.2 System components

There are several components making up the utilised TP set-up, illustrated in figure 1.5. The machine is a modified NanoInk dip-pen lithography tool, with a further description of the NanoInk system provided in section 1.4.3.

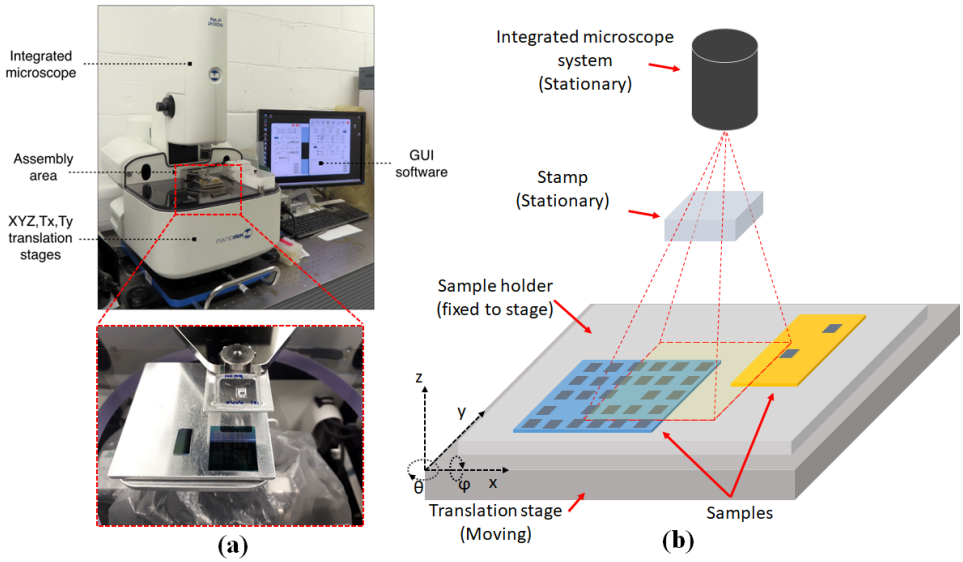

Figure 1.5: (a) Image of modified NanoInk tool with magnified view of sample holder and stamp. (b) Schematic illustration detailing the different components in which the TP system is composed.

The components of the set-up are listed:

Integrated microscope

This section contains a high resolution camera, optical column and an objective lens allowing high magnification of the samples with a field-of-view (FOV) ranging from 844 μm $\times$ 629 μm to 143 μm $\times$ 110 μm. The imaging set-up position is fixed in place above the assembly area providing a stationary, real-time optically resolved view of the pick-and-place procedure, as well as the ability to capture top-view images and recordings.

Stamp

The TP relies upon the use of a specially designed elastomeric *adhesive* stamp to pick-up the coupons of material from their source wafer, followed by the printing within the non-native receiver target. This is further explained in section 1.4.4. This section is composed of a PDMS stamp, bonded to a glass coverslip and situated between the stage and optics with the samples illuminated and imaged through the

transparent stamp. It is a stationary component of the system, fixed in position by a magnetic holder to the base of the set-up as shown within the inset of figure 1.5a.

Sample holder and stages

The final section contains the stage and sample holding block. The translation stage is the only moving part in the set-up, and is used to align and bring devices into contact with the stamp in order to both release and bond to the receiver. The samples are wax bonded to the holding block prior to TP, with the holder locked into place on top of the stage causing each move of the stage to move the samples in tandem, providing high positional control over the sample placement within the system.

1.4.3 NanoInk NLP 2000 nanolithography system

The custom-built TP machine used throughout this work is a modified commercial dip-pen nanolithography system (NanoInk, NLP 2000) where the initial application was the controlled deposition of inks with sub-micron precision and accuracy using specially mounted AFM micro-tips. Dip-pen lithography has been used for many applications such as multiplexed patterning of hydrogels with accompanied floures-cent dyes [47, 48] and the direct assembly of single-walled carbon nanotubes [49] demonstrating the systems flexibility. The system contains a stationary optical microscope system with a sub-μm optical resolution, providing digital control over both the magnification for FOV variations and focus. This combined with a high precision 5-axis translation stage, covering lateral, rotational and tilt movements, with a lateral position accuracy of $\pm$25 nm and optical encoder resolution of 5nm enables the accurate position of objects over an area of $\pm$10 cm. It is controlled by an easy to use GUI, which can be programmed for automated use.

Rotation stage

The rotational control was previously limited to manual rotational movements of the samples of interest relative to each other and the stage by using hand held tweezers. The work detailed in this thesis is highly dependent on the precision control of the sample and stage relative rotation. This was accounted for by adapting the current stage set-up by the fitting of a commercial high precision rotational controller. The implemented system is a rotary positioner (Smaract, SR-2013) with a diameter of 15mm slotting easily into the current system and requiring minor changes to the initial design without reducing on any current precision capabilities. The rotational accuracy is <35 nrad with a closed-loop rotation control.

1.4.4 PDMS stamp development and printing technique

The benefits from TP are reliant on the ability to move devices from their native wafer to a target substrate in a precise and repeatable manner. To achieve this, a great amount of thought has to go into optimising the pick-and-place procedure, with the key component being the elastomeric polydimethylsiloxane (PDMS) stamp. The following sections detail the stamp development as well as specific printing techniques.

Fabrication

There are two stages in the stamp fabrication: Firstly, the development of a re-usable stamp mould cast providing a hollow negative reproduction of the stamp geometry. Secondly, the pouring of PDMS into the mould, such that when cured the PDMS will form a finished stamp head. This full procedure is shown in figure 1.6a-d.

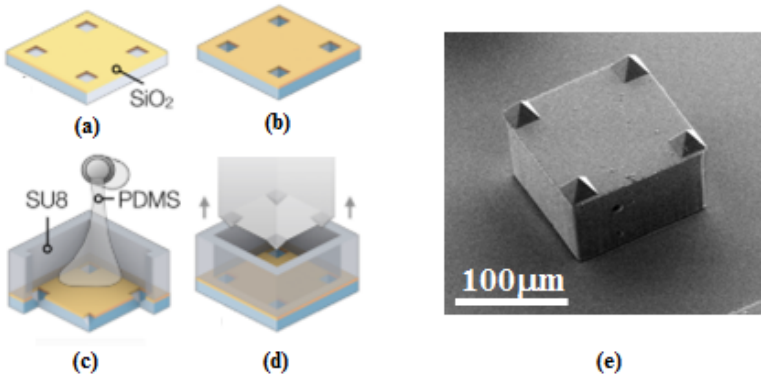

Figure 1.6: Stamp fabrication process. (a) Si wafer is patterned with a layer of silica, leaving square vias exposing the silicon. (b) The Si wafer is etched producing the corner pyramidal micro-tips, making use of the silicon 100 wafer etch planes. (c) SU-8 patterning of PDMS pouring to produce stamp head. (d) Removal of PDMS cured stamp from the mould cast. (e) SEM image of stamp head containing pyramidal features at each corner. Adapted from [3]

The stamp mould process begins by the deposition of a silica etch mask onto a Si (100) wafer, such that the openings match precisely to the crystallographic planes. A Potassium Hydroxide (KOH) etch of the Si follows the crystal lattice of the wafer, as to produce pyramid features in the exposed Si squares. By coating with an SU-8 photoresist the stamp head region is formed, with the mould ready for the PDMS pouring stage. PDMS is an organic silicone-based polymeric material. It is optically clear, and is known for its conforming and deformable nature. The production of PDMS begins with the mixing of a base material and curing agent. The weight ratio (base:curing) between both components control the PDMS rigidity and surface adhesion, with a ratio of 6:1 providing a more rigid PDMS than 8:1. Prior to annealing, the liquid mixture is poured into the stamp mould where it conforms to the stamp imprint. The mixture is thermally annealed over a set time before being released from the mould, where the end product is a solid and clear viscoelastic material, figure 1.6e. This structure is then wax bonded to a solvent cleaned coverslip ready to be attached to the TP system.

Reversible adhesion transfer printing

PDMS is viscoelastic meaning it exhibits both viscous and elastic attributes sensitive to the deformation rate, causing the adhesion forces between stamp and solid objects to become a kinetically controllable process. This is advantageous for TP, which requires both the ability to pick-up a device through strong adhesion to the stamp, as well as releasing it from the same stamp on demand. Two specific stamp designs and techniques are used throughout this work, reversible adhesion control and competitive adhesion.

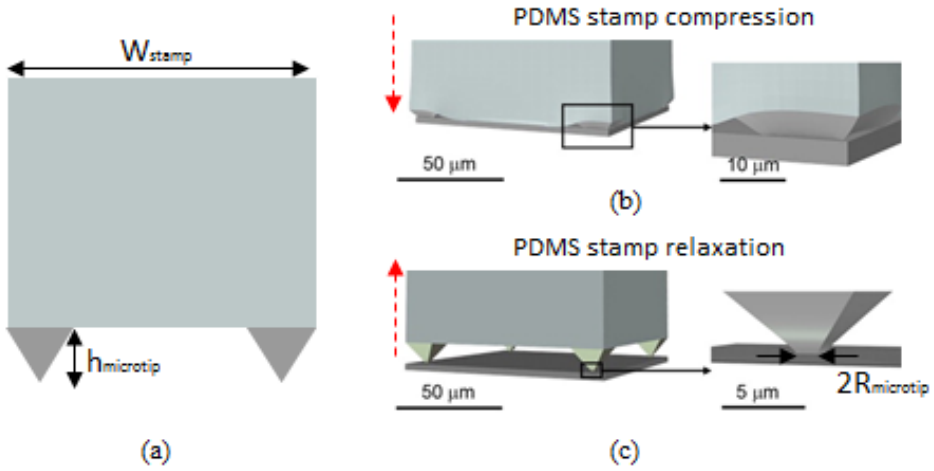

Figure 1.7: (a) Cross-sectional schematic of the TP stamp with labelled parameters. (b) An illustration of the initial stage of the reversible adhesion procedure, showing the stamp collapsing onto the object surface maximising the stamp-to-object interface adhesion. (c) Illustration of the stamp relaxation, minimizing the stamp-to-object adhesion enabling the objects release. Adapted from [4]

Reversible adhesion transfer printing refers to the process of varying the stamp to device adhesion force in order to both pick-up a device from its initial substrate, and release it onto a secondary substrate within the same process. The stamp head design can be adapted as to control the reversible adhesion properties of the stamp, with one specific design being a stamp head containing pyramid micro-tip structures

as shown in figure 1.7 [4]. As the stamp is placed into contact with the device, the compressive force causes the pyramid tips to flatten until the stamp roof collapses onto the device surface. The stamp collapse adheres the underside of the stamp to the device with a large contact area causing a high adhesion level between the two surfaces. Due to the PDMS viscoelasticity, during any quick forces the PDMS stamp will act as a solid followed by a slow return to its initial conformal state. Such as, a quick retraction of the stamp from the surface allows the device pick-up to be performed during the high adhesion state helping the release of the device from its initial substrate. Following this, the reversible adhesion protocol requires the reduction of the surface area lowering the stamp/device interface adhesion. The strain introduced by the pyramid features help promote the stamp retraction from the devices surface over a relaxation time of several seconds. This substantially reduces the contact region with the device solely held in place by the pyramid tips of the stamp head, as shown in figure 1.7c. With the reduced contact area, the stamp-to-device adhesion is now at a low enough level to allow bonding of the device onto the receiving substrate.

To successfully utilise reversible adhesion requires the ability to switch between competing compression and relaxation states of the stamp. This can be controlled by altering the stamp dimensions, with the pyramids having a height $h_{microtip}$, width $w_{microtip}$, and tip radius $R_{microtip}$ whilst the stamp head has an overall width of w_{stamp} as detailed in figure 1.7a. The stamp head will collapse onto the device surface over a length given by $2cw_{stamp}$, with the factor of $2c$ representing the collapse percentage on the stamp surface. This will in turn yield a total potential energy U_{total} within the system of:

$$U_{total} = U_{collapse} - 2c.w_{stamp}.\Gamma, \tag{1.2}$$

with $U_{collapse}$ the strain energy, and Γ the work of adhesion [50]. The percentage of the roof collapse ($2c$) is determined by minimizing the total potential energy ($\mathrm{dU}_{total}/\mathrm{dc} = 0$), which is in turn dependant on both the ratio of the pyramid radius of contact to stamp head width ($\mathrm{R}_{microtip}/\mathrm{w}_{stamp}$) and the ratio of the adhesion energy to strain energy due to the collapse, given by:

$$\frac{3.\Gamma.w_{stamp}}{E.h_{microtip}^2}, \tag{1.3}$$

in which E is the Young's modulus of the stamp material. For an overall positive potential energy the stamp will not remain collapsed on the device surface and instead can relax back to its initial shape, allowing reversible adhesion to take place.

Reversible adhesion is used in order to transfer print micro-disk resonator structures across multiple chips, chapter 4. The limited surface area of the micro-disk structures reduces the total adhesion force to the receiver substrate. Therefore, the stamp design has to be carefully tailored to minimize the contact area to the micro-disk in order to reduce the bond strength. By reducing the stamp-disk bond strength reversible adhesion transfer printing can be achieved for even ultra-small footprint devices. A PDMS curing ratio of 8:1 is used in order to promote the stamp conformation and subsequent retraction.

Competitive adhesion transfer printing

Competitive adhesion is a much simpler mechanism than reversible adhesion. Therefore, if properly optimised as a TP technique it can contribute to an extremely robust

and repeatable procedure. However, the process does require much stricter interface conditions in order to work.

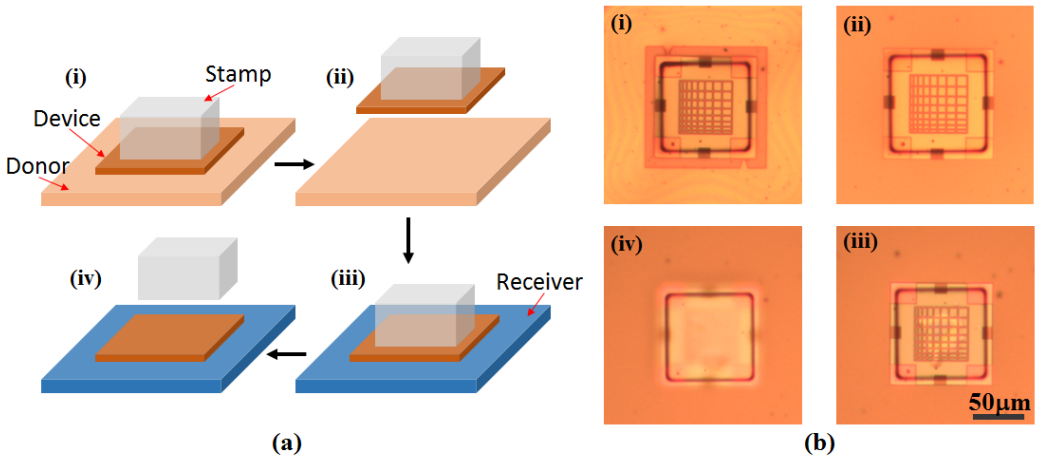

Figure 1.8: (a) Schematic of full competitive adhesion TP protocol. (i) Stamp is placed into contact with the device situated on the donor chip. (ii) A quick retraction of the stamp removes the device from donor chip where it is now bonded to the stamp head. (iii) The stamp/device is brought into contact fully with the receiver chip. (iv) As the stamp is removed, the receiver/device adhesion overcomes the stamp/device adhesion causing the device to bond to the receiver chip. (b) Top-view optical images corresponding to each separate stage of the TP procedure ((i)-(iv)).

It relies on several mechanisms. One is the varying adhesion properties of both donor and receiver as a function of their interface to the device. The second is the PDMS stamp's kinetically controlled viscoelasticity, with the procedure as follows, and depicted in figure 1.8. Firstly the stamp, containing no pyramidal structures, is placed into contact with the device. The van der Walls interactions cause the stamp to conform and fully collapse onto the surface producing an intimate bond between both interfaces. A high release velocity of the stamp-to-surface promotes a strong adhesion which overcomes the substrate/device adhesion to release the device from the surface. If the device is suspended, this stage can be further controlled by varying the support anchor dimensions as to reduce the forces necessary to break and release the device. The second stage is the release procedure, and relies on the

device/substrate interface. If the device/substrate interface adhesion is preferential to the device/stamp interface, a sufficiently slow release of the stamp will allow the device to separate and release onto the substrate surface. One crucial factor is the PDMS adhesion stength. It is required that the stamp/device adhesion strength lies between both the device adhesion to donor (lower adhesion) and receiver (higher adhesion), controlled by varying the ratio of PDMS to curing agent during the stamp fabrication.

In this work, the competitive adhesion technique is used for the ultra-thin silicon membrane devices detailed in chapters 2 and 3, supported by their high surface quality and conformal nature which produces an extremely high adhesion to the receiving surface. The PDMS curing ratio used is 6:1.

1.5 Photonic devices

Throughout this thesis, the most commonly used photonic device is known as an optical waveguide. These come in many forms, from straight waveguides, ring resonators, and WGM disk resonators and are used for a range of passive and active PIC components, such as optical interconnects, (de)multiplexers, modulators, and optical filters. With device geometries at the sub-micron scale, the requirement for a high precision integration scheme is key for the efficient incorporation within PICs. As such, this makes them perfect tools for the characterisation of the newly developed high accuracy transfer printing method.

1.5.1 Optical waveguides

Optical waveguides are used for the on-chip confinement and transmission of light across a given distance, ranging from μm-scale in integrated photonic systems to

km-scale in long-distance fibre optics. They are generally composed of two materials, a high refractive index core region and a lower refractive index cladding with light propagating within the core in the longitudinal (z) direction. Many different waveguide architectures exist, and throughout the work we will focus on chip-scale waveguide structures as shown in figure 1.9.

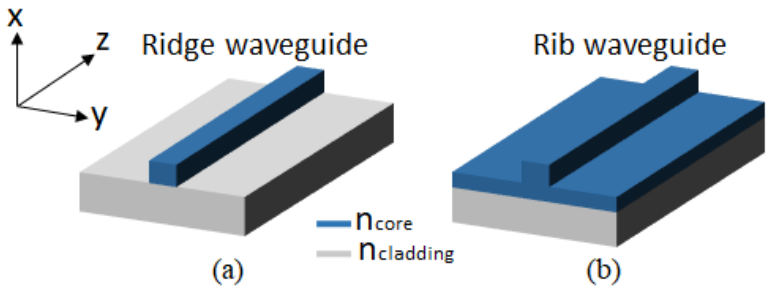

Figure 1.9: Schematic illustration of different optical waveguide types; (a) ridge waveguide; (b) rib waveguide. Core layers refractive index (n_{core}) is larger than cladding refractive index ($n_{cladding}$) within both designs.

The two geometries in figure 1.9 are channel waveguides. In channel waveguides light is confined within the transverse (x,y) directions with a corresponding refractive index profile given as n(x,y). For the ridge waveguide, the high refractive index core is situated on top of the lower refractive index cladding layer and the three remaining sides are air clad in order to produce a high optical confinement. The rib waveguide contains a high refractive index slab region separating the core and substrate, with light confined partially between both regions. The ridge design is used for the all-pass resonator bus waveguides throughout this work, whilst the rib waveguide design enables the production of the shallow-etch silicon suspended membrane devices as further detailed in chapter 3.

The lateral confinement of guided waves within the waveguide structures exist in the form of guided modes or "standing waves", which have a transverse field pattern

whose amplitude and polarisation profiles remain constant along the propagation direction [51]. The only criteria allowed to vary in propagating modes are the overall phase, as well as any loss or gain of the total optical power which are properties related to the propagation constant. When considering a two-dimensional refractive index profile n(x,y), the electromagentic field components of the guided modes are found in the form:

$$E_v(x, y, z, t) = \mathcal{E}_v(x, y)e^{(i\beta_v z - i\omega t)}, \tag{1.4}$$

$$H_v(x, y, z, t) = \mathcal{H}_v(x, y)e^{(i\beta_v z - i\omega t)}, \tag{1.5}$$

where v is the waveguide mode index, $\mathcal{E}_v(x, y)$ and $\mathcal{H}_v(x, y)$ are the relevant field profiles, and β_v is the waveguide mode propagation constant. If the propagation constant is far from the cut-off state ($\beta_v \approx \mathrm{k_0 n_{cl}}$) the light is guided, where $\mathrm{k_0}$ is the free-space propagation constant ($\mathrm{k_0} = \omega$ / c) and $\mathrm{n_{cl}}$ is the cladding refractive index.

Marcatili's method is an approximate analytic method which desribes the behaviour of light propagating in a rectangular channel waveguide. It is used to derive the propagation constants and effective (modal) refractive index of guided fields of rectangular channel wavegudies based on the separation of the spatial variables (x,y) [52]. The model treats the waveguide core as having a rectangular cross-sectional geometry of refractive index n_1 with height a_h and width a_w, whilst the surrounding region is split into transverse quadrants with refractive indices $n_{2,3,4,5}$ as depicted in figure 1.10.

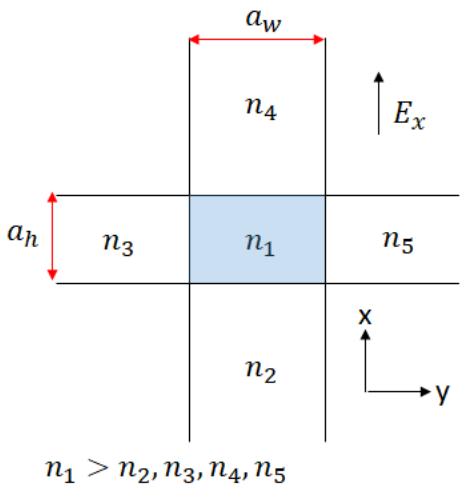

Figure 1.10: Cross-section of a rectangular waveguide illustrating the core (blue) and cladding refractive index regions. The high refractive index is given by n_1, low refractive indices for each cladding region as $n_{2,3,4,5}$ and a_w, a_h are the waveguide width and height.

The model requires the appropriate boundary conditions between the core and cladding region, as stated:

(i) The tangential components of both the electric field $\boldsymbol{E}$ *and magnetic field* $\boldsymbol{H}$ *must be continuous across the core cladding interface.*

(ii) The normal components of the electric displacement $\boldsymbol{D}$ *and the magnetic induction* $\boldsymbol{B}$ *must be continuous across the core cladding interface.*

The derivation of the longitudinal propagation constant k_z and the effective refractive index are given as:

$$k_z = ({k_1}^2 - {k_x}^2 - {k_y}^2)^{\frac{1}{2}}, \tag{1.6}$$

$$n_{eff} = \frac{k_z \lambda}{2\pi}, \tag{1.7}$$

where k_x and k_y are the transverse propagation constants in the x and y plane,

which are stated below:

$$k_x = \frac{p\pi}{a_w}\left(1 + \frac{A_3 + A_5}{\pi a_w}\right)^{-1}, \tag{1.8}$$

$$k_y = \frac{q\pi}{a_h}\left(1 + \frac{{n_2}^2 A_2 + {n_4}^2 A_4}{\pi {n_1}^2 a_h}\right)^{-1}, \tag{1.9}$$

with p and q indicating the number of extrema of the sinusoidal field components within the waveguide core, and the values of the field amplitude of each region $A_{2,3,4,5}$:

$$A_{2,3,4,5} = \frac{\lambda}{2({n_1}^2 - {n_{2,3,4,5}}^2)^{\frac{1}{2}}}. \tag{1.10}$$

The guided modes are subject to electromagnetic field orientations known as their polarisation states, with waveguide modes subject to polarisation in two directions, transverse electric (TE) and transverse magnetic (TM). The TE polarisation is characterised by its electric field being perpendicular to the plane of incidence and magnetic field lying in the incident plane. The opposite is true for TM with the magnetic field perpendicular to the plane of incidence and the electric field lying along the incident plane. Control over the waveguide polarisation state is important for a range of applications, such as coherent receiver technologies [53] and polarisation multiplexing [54]. The fundamental polarised modes can be described by TE_{00} and TM_{00} and correspond to the waveguide mode with the lowest critical frequency, with figure 1.11 containing simulated mode profiles of both TE_{00} and TM_{00} states for a silicon waveguide with cross-sectional dimension of 220x500 nm at 1550 nm.

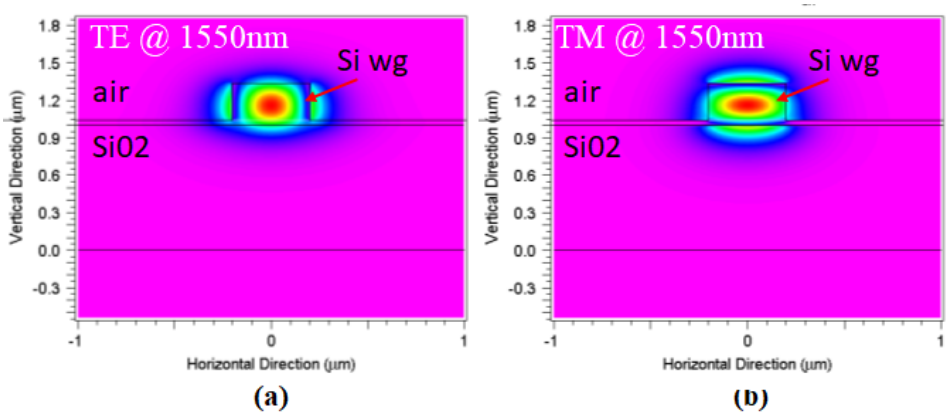

Figure 1.11: Fundamental mode profiles for a silicon waveguide with a cross-section of 220x500 nm at 1550nm input wavelength. (a) Fundamental TE_{00}; (b) fundamental TM_{00}.

Optical waveguides can either be multi-mode or single-mode, controlled by the waveguide cross-sectional dimensions and material composition of the core and cladding. Multi-mode refers to a structure with a relatively large core diameter allowing propagation of many modes at any one time. They are typically used for short-haul communications as they can transmit a large amount of information, however over larger distances can have high losses through mode cross-talk and dispersion effects [55]. Single-mode waveguides have much smaller core dimensions. They only support the propagation of one individual guided mode due to their compact size, removing losses from modal cross-talk. They are generally favoured for integrated photonics where they are valuable for applications such as chip-to-chip or on-chip optical data links across generally longer distances than their multi-mode counterpart [56]. Throughout the work, SOI single-mode waveguides with TE_{00} are the most commonly studied. They are made up of a core of Si with refractive index of n=3.45 and a cladding of silica of refractive index n=1.44, both at λ=1550 nm. For strip waveguides, a top cladding is either composed of silica, a resist with similar refractive index, or an air cladding. Due to the high refractive index contrast, the standard

cross-sectional dimensions exhibited for Si waveguides are 500nm width and 220nm height.

1.5.2 Resonators

Optical resonators are important components in integrated optics, primarily due to their compact design capabilities and high versatility. They are used for spectral filtering, with applications ranging from wavelength (de)multiplexers within WDM systems [12] and network-on-chip matrix switches for photonic interconnection networks [57]. Further applications such as sensor systems take advantage of their high sensitivity to environmental changes within a system [58], whilst their strong resonant enhancement capabilities make them highly applicable in low-power chip-scale nonlinear systems [59]. This section will briefly cover the background theory of micro-resonators, focusing on standard all-pass micro-ring and disk resonators coupled to bus waveguides.

Properties of all-pass resonators

A resonator is a device or system which exhibits natural oscillations at specific resonant frequencies, producing higher amplitudes than non-resonant frequencies. These oscillations can be in the form of mechanical (acoustic) or electromagnetic (optical), with the primary use being the generation or selection of these specific frequencies from a signal. An optical resonator is formed when a waveguide is looped, forming a closed waveguiding geometry. When the resonator is put in close proximity (or contact) with a second bus waveguide, the two components interact in such a way to produce a coupling mechanisms enabling the routing of light on/off the resonator. An optical resonator can satisfy any looped waveguide geometry, with standard all-pass

ring resonator and disk resonator geometries shown in figure 1.12.

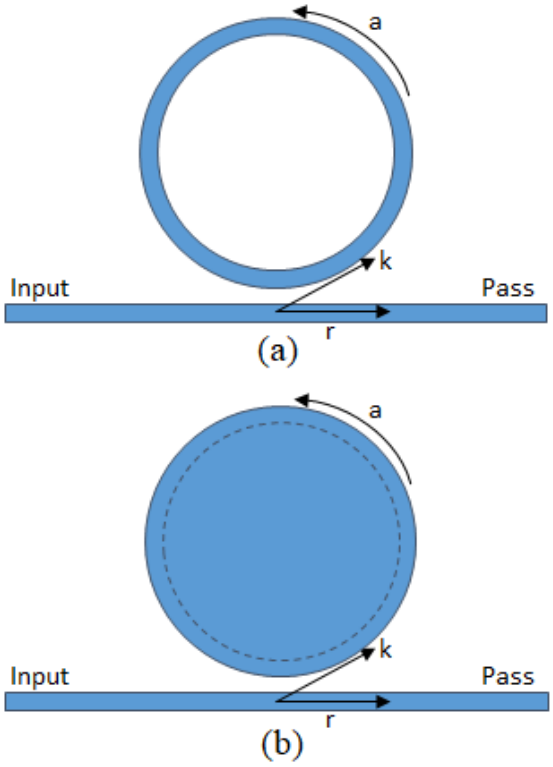

Figure 1.12: Illustration detailing (a) an all-pass ring resonator with the single-pass amplitude transmission a, the cross-coupling coefficient k and the self-coupling coefficient r labelled; (b) an all-pass disk resonator.

When EM waves are coupled into the resonator from the bus waveguide, they travel continuously around the cavity until they are either coupled back into the bus waveguide or diminished through internal/external loss mechanisms. When they are at a specific wavelength such that they fit an integer number of times inside the cavity optical length they are in resonance with the cavity, the waves constructively interfere causing an increase in the field intensity, otherwise it is off-resonance which causes subsequent destructive interference which reduces the power within the cavity. The transmission intensity of the bus waveguide when on-resonance sees a transmission drop as the light is confined fully in the resonant cavity, detailed in figure 1.13. The

resonant wavelength λ_{res} of a resonator is calculated by:

$$\lambda_{res} = \frac{n_{eff}L}{m}, m = 1, 2, 3... \tag{1.11}$$

L is the cavity round-trip length and n_{eff} is the effective refractive index, with $L \times n_{eff}$ corresponding to the optical path length of the resonant cavity structure. The final parameter is the integer number of wavelengths which make up the cavity length and are given by m.

For a continuous wave operation, the basic output spectral properties of an all-pass resonator can be written as the ratio of the transmitted field (E_{pass}) to the incident field (E_{input}) [60]:

$$\frac{E_{pass}}{E_{input}} = e^{i(\pi+\phi)}\frac{a - re^{-i\phi}}{1 - rae^{i\phi}}. \tag{1.12}$$

ϕ=βL is the round-trip phase shift of the circulating mode, a the single-pass amplitude transmission, and r the self-coupling coefficient. The above equation corresponds to the ratio of light which passes through the bus waveguide - without interacting with the resonant cavity - to the light which enters the cavity due to the coupling conditions of the system, and measures the output electric field intensity of the resonator. Further to this, the ratio of the transmitted intensity to the incident intensity - otherwise known as the buildup factor or transmission intensity - is given by the squared modulus of equation and provides the output power of the resonator system 1.12 [61]:

$$T = \frac{I_{pass}}{I_{input}} = \frac{a^2 - 2ra\cos\phi + r^2}{1 - 2ar\cos\phi + (ra)^2}. \tag{1.13}$$

The two power splitting ratios of the system are the self-coupling coefficient r

and the cross-coupling coefficient k, and satisfy $r^2 + k^2 = 1$, such that no losses are produced within the coupler region. The all-pass transmission intensity equation 1.13 is used within this work to theoretically fit and characterise any produced resonator devices.

The coupling factor falls within three regimes, under-coupled, critically coupled and over-coupled. For the situation when r=a and ϕ=0, the on-resonance intensity of the transmitted light drops to zero such that it has a larger extinction. This case is known as critical coupling, where the coupled power is equal to the power loss within the cavity. The two other coupling regimes can be distinguished by the same relationship, such that over-coupling of the waveguide/resonator is achieved for $r > a$ and under-coupled for $r < a$. Critically coupled resonator devices exhibit highly sensitive variation in transmitted power based on small changes in the coupling coefficient into the resonant cavity, this makes them typically suited for switches and modulators [62].

Figures of merit

A resonators performance level is characterised using specific figures of merit relating to the shape of the devices optical output, with this section detailing the range of criteria which are commonly used which are shown in figure 1.13.

The full width at half maximum (FWHM) is the name given to the width of the resonance dip at half of its maximum intensity drop value, used to measured the resonance width. The derivation of the FWHM for an all-pass ring resonator is given by:

$$FWHM = \frac{(1 - ra){\lambda_{res}}^2}{\pi n_g L \sqrt{ra}}, \tag{1.14}$$

with L being the cavity lengths, and n_g the group refractive index. A resonators free spectral range (FSR) is given by:

$$FSR = \frac{\lambda^2}{n_g L}. \tag{1.15}$$

It is a measure of the separation between two adjacent resonances produced by a resonator, and is strongly linked to the resonant cavity length. Both FWHM and FSR are defined by the group refractive index n_g rather than n_{eff}:

$$n_g = n_{eff} - \lambda_0 \frac{dn_{eff}}{d\lambda}, \tag{1.16}$$

with n_g also given by the ratio of vacuum velocity of light to the group velocity within the medium ($n_g = \frac{c}{v_g}$), with v_g a measure of the velocity at which the envelope of a propagating pulse travels. The importance of n_g relates to the measure of a devices dispersion which can significantly influence the resonant conditions. As it is a measure of the variation in n_{eff} over a wavelength range, a change in n_{eff} primarily alters λ_{res}.

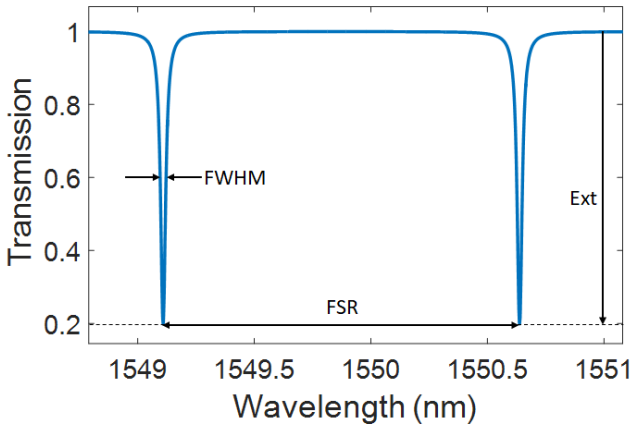

Figure 1.13: Theoretical transmission spectrum of a waveguide coupled to an all-pass single-mode ring resonator with resonant wavelength depicted by a drop in the output transmission intensity. The spectral features displayed include the free spectral range, full width half maximum and the resonance extinction.

There are two main parameters used for the characterisation of resonator performance, the finesse ($\mathcal{F}$) and the quality factor (Q-factor) with both utilising the described figures of merit. Each are measurements of the resonance sharpness, however the finesse measures the sharpness as a function of the resonance separation and the Q-factor as a measure of the central frequency component. For each parameter, a larger calculated value corresponds to a resonator device with a higher performance level. The relationship between the resonators FSR and FWHM defines the finesse:

$$\mathcal{F} = \frac{FSR}{FWHM}. \tag{1.17}$$

Whilst the Q-factor provides a measure of the resonant wavelength with regards to the resonance FWHM:

$$Q = \frac{\lambda_{res}}{FWHM}. \tag{1.18}$$

A ring resonators Q-factor can be characterised by two distinct configurations, loaded and unloaded (intrinsic). The unloaded Q-factor is an independent measure of the resonators internal properties, accounting solely for internal loss mechanisms, whilst the loaded Q-factor is a measure of the full system, including such factors as the coupling loss introduced by the bus waveguide. Overall, the losses experienced by a resonator can be broken down into propagation loss, losses in the coupler section, and bend losses and are summarised by:

$$A_{dB} = A_{propagation}L + 2A_{coupler} + 4A_{bend}, \tag{1.19}$$

with $A_{propagation}$ the propagation loss per unit length and expressed in (dB/cm), $A_{coupler}$ the coupler loss and A_{bend} the bend loss. The unloaded Q-factor will only

measure the propagation and bend losses produced within the resonator cavity, whilst the loaded Q-factor measured everything. This work will focus solely on the loaded Q-factor value as it provides a better representation of the resonant device and its contribution within a larger system.

In the case of an all-pass ring resonator, the loaded and unloaded Q-factors can be expressed by the following [63]:

$$Q_L = \frac{\pi n_g L \sqrt{ra}}{(1 - ra)\lambda_{res}}, \tag{1.20}$$

$$Q_{UL} = \frac{2Q_L}{1 \pm \sqrt{T_0}}, \tag{1.21}$$

where $Q_{UL,L}$ are the unloaded and loaded Q-factors, L is the ring length and T_0 is the normalised transmitted power at the resonance wavelength. For the unloaded Q-factor, the + and - signs correspond to the under- and over-coupled regimes, respectively. Equation 1.20 is used for the calculation of the Q-factor for all resonator devices produced throughout this work.

Overall, the resonator theory within this section gives an understanding of the spectral properties of both ring and disk resonator devices and their subsequent measurement criteria. However, the implementation of disk resonators introduces the concept of whispering gallery modes (WGM).

Whispering gallery modes

The definition of a whispering gallery mode was first introduced by Lord Rayleigh who studied the phenomenon of the whispering gallery, the circular gallery running around the interior of the dome within St. Pauls cathedral in London. It got this

name because a whisper against its wall at any point around the circular dome is noticeably audible at the opposite end of the dome when a listener puts their ear up against the wall. This was due to the refocusing effect of the sound as it travelled around the curved surface, combined with the constructive interference of the signal at given intervals around the gallery [64]. Following this, it was proven that such surface propagating modes can exist for electromagnetic waves within looped cavities, and since then optical WGM resonator devices have been used for a wide range of research spanning applications from nonlinear optics [65], as on-chip filters and switches in optical communications [66], and even as microlasers [67].

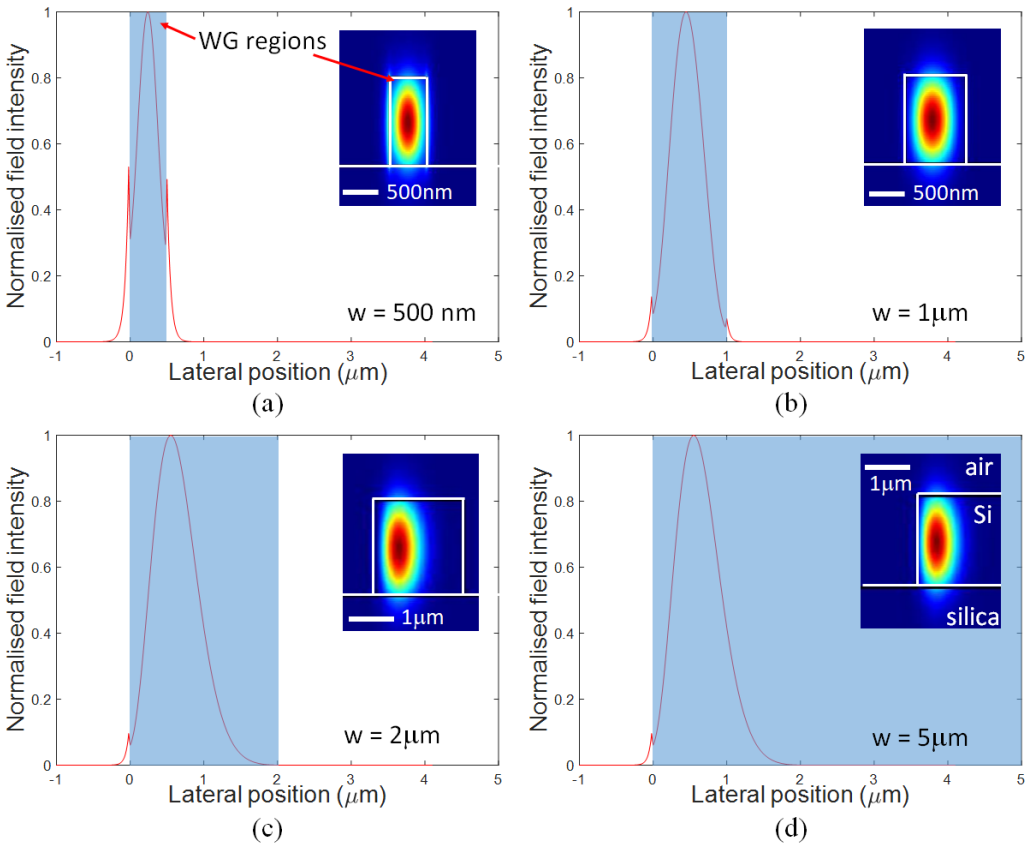

Figure 1.14: Transition of a normal looped waveguide mode into a whispering gallery mode by a variation in the waveguide width, simulated with a bend radius of 20 μm. Plots contain the normalised field intensity as a function of the lateral position from the resonator edge (0 μm offset) for waveguide widths of (a) 500 nm; (b) 1 μm; (c) 2 μm; (d) 5 μm. The blue region represents the waveguide cross-sectional width, with WGMs exhibited for width of 2 μm and upwards. The inset contains the corresponding simulated mode profiles using a FDE mode solver.

The propagation of supported WGM in optical resonators comes into effect as the width of the looped waveguide region is increased. The increased width changes the supported mode profile which eventually leads to the structure becoming multi-modal. However, if the core width is increased beyond a certain limit, a regime is reached where the bend modes become guided solely by the outer periphery surface with the inside surface interaction becoming irrelevant. This guiding mechanism is what is known as whispering gallery modes [68], depicted within 1.14. WGM are exhibited within disk resonators, however they can also be present in both spherical

and toroidal shaped resonators with the ability to produce extremely high Q-factors and low mode volumes [69].

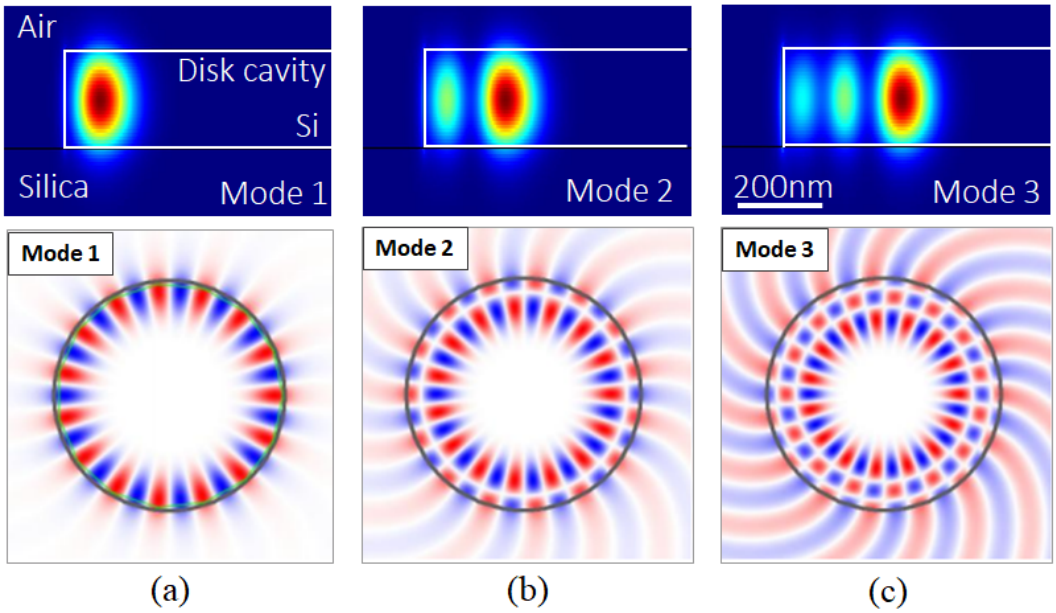

Figure 1.15: Simulated mode profiles for the fundamental and higher order WGMs confined to a disk resonator, depicted by a disk resonator cross-section and top-view of the field profile as the light travels around the cavity. Each resonator has an azimuthal mode number of m=15, and a radial mode number of (a) N=1; (b) N=2; (c) N=3.

In the same fashion as the fundamental outer periphery mode, higher order WGMs can propagate within the cavity with shorter propagating circumference, as shown in figure 1.15. For a growing mode number, the propagating wave experiences a shift of the profile intensity maxima inwards into the cavity, an increase in the exterior field intensity, and a wider radial profile causing an increase in the mode volume. An advantage in utilising the higher order WGMs comes from the reduction in the edge localisation, reducing the sidewall interaction which can lead to the lowering of scattered loss, allowing a reduction in the fabrication tolerances. Past research has shown that the higher order WGMs can also provide increased sensitivity suitable for specific biosensing applications [70].

The photonic device section provides insight into the understanding and characterisation of resonator devices, focusing on the theory behind all-pass resonators incorporating both ring and disk resonator geometries. The performance measurements of resonator devices is utilised throughout the work by Q-factor calculations where the produced devices are compared to existing monolithic and state-of-the-art research.

1.6 Thesis outline

This work will be focused on the development of an integration method, utilising the technique of TP, as a means to produce LS-PIC technologies. The main focus will be on the development of a nanoscale alignment procedure to use alongside TP allowing the efficient vertical integration of waveguiding components such as optical waveguides and resonators across multiple material platforms.

The thesis will be split into several chapters. Chapter 2 will focus on the development and implementation of a high alignment accuracy technique used alongside a custom-built TP system for precision integration of hybrid passive photonics components. This includes both systematic alignment accuracy measurements as well as statistical analysis of device integration of the implemented alignment method.

Chapter 3 will focus on the vertical assembly of silicon ultra-thin membranes with nanoscale accurate placement accuracies. Si membranes containing ring resonators are micro-assembled with bus waveguides on a receiver SOI platform with controlled lateral coupling gaps. The accuracy will be demonstrated through SEM image measurement of the placement accuracy and the varying resonant coupling conditions of each device with respect to the coupling offset. This is followed by a section describing the work into 3-D micro-assembly of stacked Si membranes, including the

production of a stacked membrane DBR composed of a silicon and silica interlayer structure of nanoscale thicknesses. The assembly technique demonstrates high lateral and rotational placement accuracy across multiple layers, with the DBR exhibiting reflectance across the visible spectrum comparable to theoretical simulations.

Chapter 4 details the micro-assembly of hybrid micro-disk resonators, with III-V micro-disks TP to a Si bus waveguides on a non-native SOI platform. The controlled lateral placement of the disks demonstrate the ability to selectively couple to different mode families within the WGM resonators. Further to this, the hybrid device's non-linear capabilites are measured through FWM experiments, exhibiting high FWM efficiencies at low input powers. After this, conclusions drawn from the presented work are given, alongside descriptions of future possible research directions.

Chapter 2

Nanoscale absolute alignment for transfer printing

2.1 Introduction

Transfer printing (TP) is a promising micro-assembly technique for chip-scale intergated optics, with research spanning a wide range of material platforms and device technologies. Several demonstrations include integrated micro-LEDs [71], flexible integrated circuitry [72], and the manipulation of nanowire lasers [73]. However, the back-end integration of waveguide PIC technologies has not yet been fully capitalised. One main reason for this is the need for nanoscale precision integration when considering the efficient coupling of multiple waveguiding layers, with the state-of-the-art absolute placement accuracy of transfer printing limited at ± 1.5 μm (3σ). Different techniques exist to reduce the alignment tolerances, such as back-end processing [45] or the design of tapered couplers as a means to decrease the necessary alignment tolerances [46]. However, to fully capitalise on transfer printing as a reliable method for the micro-assembly of waveguide PICs requires nanoscale device placement accuracy.

A high precision cross-correlation alignment technique implemented within a TP

system is presented within this chapter. The technique enables the alignment resolution to be reduced to below that of the current optical imaging limit, enabling chip-to-chip absolute alignment. The chapter is split into four different sections. The first section is an overview of cross-correlation alignment, with the characterisation of an optimised alignment mark geometry for increased autocorrelation resolution. After this, the implementation of correlation alignment into the TP system is explained, with subsequent testing of the absolute systematic alignment accuracy achievable. A chip-to-chip alignment procedure is explained, followed by the statistical analysis and measurement of the absolute device TP placement accuracy of silicon membrane devices between two SOI substrates. The final section details the implementation of alternative cross-correlation alignment techniques for different device types, including the cross-correlation alignment of free-standing disk structures and the high accuracy TP of nanowires lasers (NWs) for the large-scale controlled manipulation of NWs.

2.2 Cross-correlation

This section explains the technique of cross-correlation alignment, followed by the characterisation of optimised alignment marks helping improve on the obtainable resolution.

With the continual decrease in photonic component feature sizes, the demand for increased resolution limits in lithography is extremely high. Particular interest is paid to the alignment technology, as this plays a large part in the restricted resolution capabilities of the systems. As such, the development of a high precision alignment technique for transfer printing can be heavily influenced by the development of past optical and electron-beam lithography techniques. Many methods

exist, such as Moiré-based interferometry. This involves the superposition of two periodic structures producing Moiré fringes, with the lateral misalignent measured as a function of the phase relationship. This method has achieved alignment accuracies at the nanoscale [74]. Another method uses physical means to force structure alignment, similar to flip chip bonding. Using micro-mechanical passive alignment, pitted structures slot multiple wafers into place, side-stepping the optical resolution of the imaging system [75]. Resolution using this method has been shown to be below 200 nm as well as having a good interlayer bond quality.

In electron-beam lithography (EBL), it is possible to pattern nanoscale (sub-10 nm) features. This can exploited with nano-scale precision alignment across multiple lithographic steps helping to produce extremely compact and complex photonic systems. One particular alignment method adopts correlation, with research employing a cross-correlation algorithm as a repeatable, non-destructive manner to produce absolute alignment accuracies below a nanometre [76, 77]. The goal of the following work is to adapt cross-correlation as a solution to achieve optically resolved nanoscale positional alignment with our custom-built TP system.

2.2.1 Overview

Cross-Correlation is a signal processing technique measuring the similarity between two identical signals as a function of displacement between each [78]. The cross-correlation scale ranges from -1 to 1 with identical signals producing a correlation value of 1, which allows the relative positional measurement of two signals. This technique is versatile and has been implemented within technologies such as single particle analysis [79], and fingerprint matching [80]. It is interpreted by equation 2.1, in which A and B correspond to two signals. Signal A varies either by a time-lag

or positional displacement with respect to a non-varying (stationary) signal B. The cross-correlation value can be interpreted as an offset in an x and y displacement from the initial position (i,j), where $\mu_{A,B}$ and $\sigma_{A,B}$ are the mean and standard deviation of their respective signals A and B:

$$Corr(A,B)[x,y] = \frac{\sum_{i=1}^{N}\sum_{j=1}^{N}(A(i,j)-\mu_A)(B(i+x,j+y)-\mu_B)}{\sigma_A\sigma_B}. \tag{2.1}$$

The measurement accuracy is obtained from the resolution of the object displacement. As such the alignment of two signals can be achieved over extremely small length scales, which is what makes this a desirable technique.

Cross-correlation alignment as a function of positional displacement is used within this research, and graphically shown for two objects A (grey) and B (red) in figure 2.1.

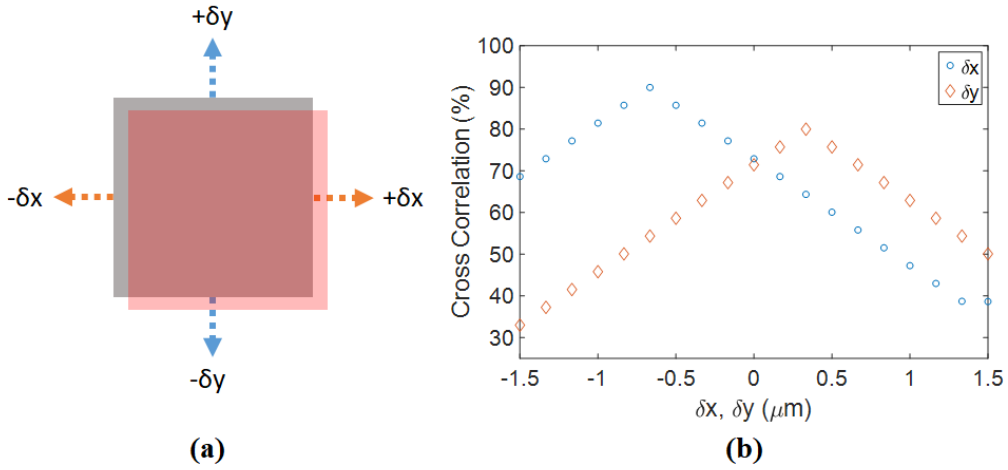

Figure 2.1: (a) Schematic of cross-correlation as a function of object displacement. (b) Cross-correlation strength as a function of object displacement.

When A and B are initially overlapped they have a correlation strength (%) mea-

suring the similarity at that position within a fixed imaging region, with the initial overlap position δx,δy=0. The movement of object A adds a relative displacement between the two objects, with the object similarity varying as a function of the displacement. This is measured as a change in the cross-correlation strength (%). At a specific displacement, the correlation will reach a peak when the objects achieve their maximum point of similarity. This is illustrated by a plot in figure 2.1b where the maximum correlation strength has been measured for both horizontal and vertical displacements, depicted over a displacement range of several μm.

The particular alignment marks used for cross-correlation can significantly improve or detract from the cross-correlation sensitivity and therefore the resolution limit of the technique. As such, work has been carried out to determine the design achieving highest sensitivity.

2.2.2 Alignment mark

In this section various different alignment mark geometries will be introduced, some used for typical lithography processes whilst others which have been optimised solely for cross-correlation. This is followed by the theoretical comparisons of each design.

Simple designs

A variety of different marker geometries have been used in both lithography and wafer alignment processes [81]. These range from simplified shapes to more complex geometric designs, with the most widely used based upon simple geometric shapes composed primarily of rectangles and squares, with several examples shown in figure 2.2.

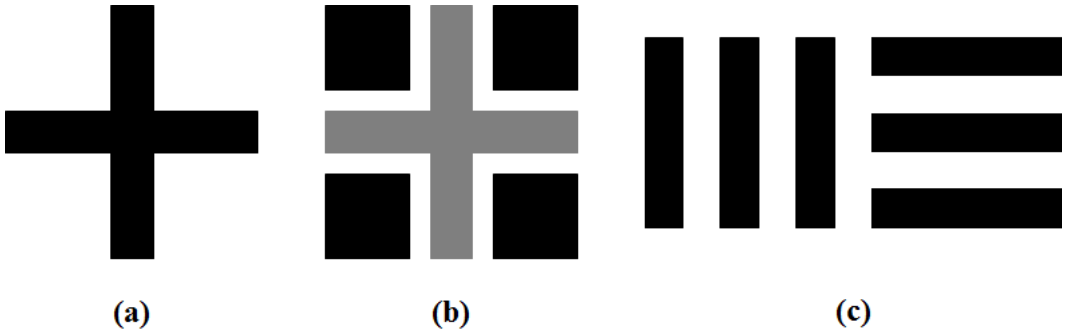

Figure 2.2: Illustrations of a range of simple geometric alignment mark designs. (a) Cross; (b) multi-layered cross design (black - layer 1; grey - layer 2); (c) periodic lines (USAF resolution chart).

The advantage of such designs come from the ease of replication for high-yield production of defect free markers, with the typical use for edge-detection overlay alignment. The usage of high contrast materials and an optimised fabrication process will improve the alignment capabilities, captilising on the simple design. Figure 2.2a depicts a cross structure composed of two orthogonal rectangles of identical width and height with overlapping centres. An overlay of multiple crosses provides edge profile information for both x and y directions, limited by the resolution limit of the microscope and camera system. Slightly more sophisticated designs can improve on the alignment resolution. Figure 2.2b is an alignment marker composed of two sections situated on two different lithography layers. For example, the pattern of squares may be written in a first lithography stage. The cross pattern is incorporated in the mask for the second lithography stage. Alignment of the second stage mask to the already realised first layer features is achieved by aligning these two patterns in the lithography system, typically using an optical microscope. This type of complementary pattern is commonly used for multi-layered alignment processes in photolithography. The overlay of the simple designs creates a third more complex alignment mark. One strategy to improve the alignment resolution is the increase in

number of edges, such as the design shown in figure 2.2c. The increased number of lines will improve on the overall positional information which can be extracted.

Complex designs

More sophisticated marker geometries can be implemented to further improve alignment resolution, this has been previously achieved for cross-correlation alignment within EBL systems [76, 82]. Several design conditions help optimise the correlation sensitivity of the alignment mark. Firstly, the alignment mark requires a sharply peaked autocorrelation signal [83], indicated by a broad spectral density. This is achieved by having a large frequency range implemented within the signal. With regards to a two-dimensional pattern, to fully incorporate this requires a non-centrosymmetric pattern, which is aperiodic in nature.

There are a number of alignment mark designs exhibiting this aperiodic characteristic, several are shown in figure 2.3. Figure 2.3a is a design based upon a Barker sequence [84], a finite sequence of integers each having a value of +1 or 0. Its ideal autocorrelation properties are depicted by its relatively uniform distribution of information. Further to this, it's easily fabricated by standard lithography processes. As both the x/y-axis positional information are separate, a Barker sequence alignment mark is required using multiple rotated sequences. Figure 2.3b details a fractal pattern known as a Sierpinski carpet, which includes a self-similar design of squares at increasingly smaller scales. An advantage of this being that the design can be used over multiple magnifications, therefore useful over different resolution scaled imaging systems.

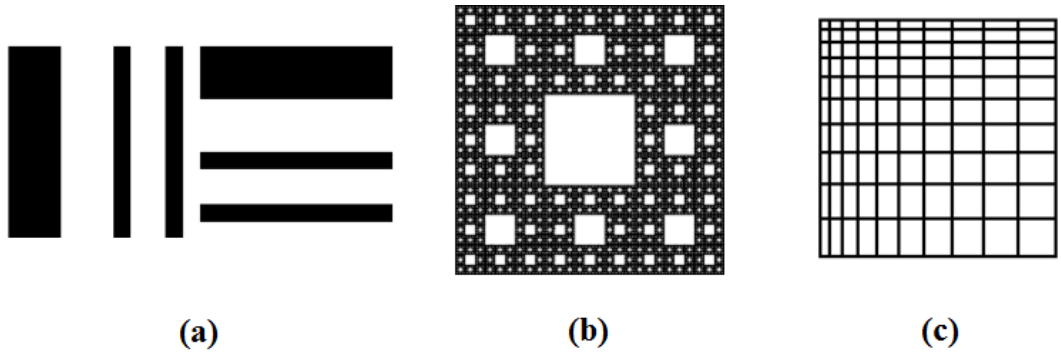

Figure 2.3: Illustations of different complex alignment mark designs. (a) Barker sequence; (b) sierpinski carpet fractal pattern; (c) tapered grid design.

Another design is a tapered grid, as shown in figure 2.3c. It is formed by the repetition of lines with a varying pitch across the full area. The simplified geometry, similar to the designs in section 2.2.2, helps improve on the fabrication yield in particular when the linewidths are kept at micron-scale. Further to this, a greater number of lines increases the amount of extracted positional information.

Alignment mark comparisons

The comparison of different marker designs will determine the optimised marker to be employed for cross-correlation alignment. However, prior to the comparison some specific design conditions for helping improve the sensitivity are discussed. Firstly, the design should be made up of easy to produce micron scale simple geometric structures. This is to minimise on the fabrication errors which can cause variations from marker to marker. Further to this, it enables highly resolved and well-defined objects within optical resolution limited systems. Secondly, the alignment marks must be aperiodic in nature to maximise their autocorrelation sensitivity. The method of comparison involves measuring the cross-correlation sensitivity as a function of lateral misalignment and magnification offsets. Therefore, the cross-correlation of theoretical versions of each marker design is calculated with variations in one of the

two markers' lateral position within the FOV as well as its overall magnification. The steeper the gradient drop in the correlation strength with respect to any positional offset signifies the marker sensitivity. Figure 2.4 includes a range of alignment mark designs user for theoretical cross-correlation comparison tests, in which they're autocorrelated across a lateral displacement offset (± 2 μm) and magnification variation (± 10 %). The effectiveness of the marker is assessed using the gradient of the cross-correlation as a function of offset. The higher the gradient, the easier it is to define the maximum correlation point, and hence the absolute position of the marker. In addition, any secondary maxima in the cross-correlation are detrimental to the effectiveness of the marker design.

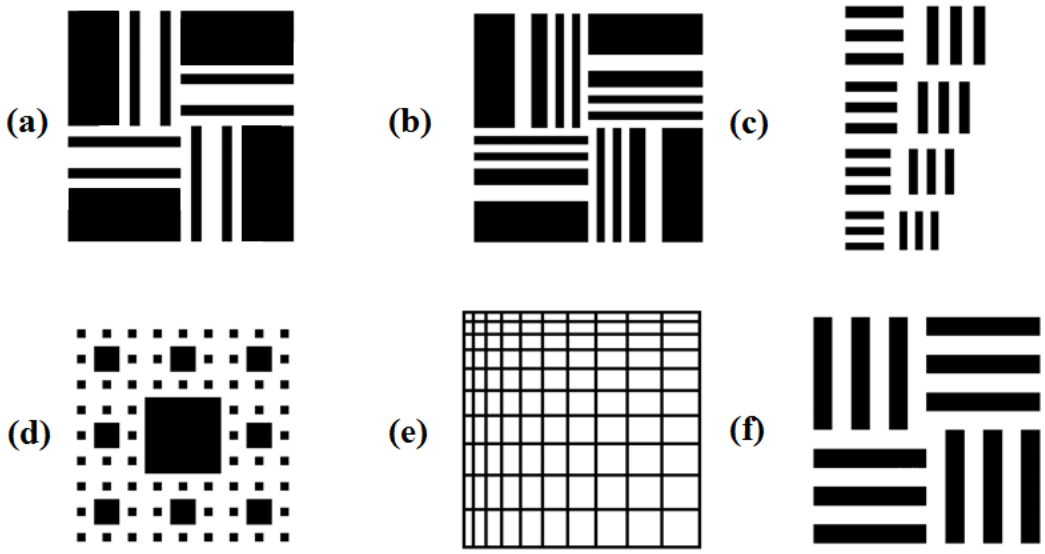

Figure 2.4: Range of alignment marker designs used for theoretical comparisons. (a) Barker 11 (rotated); (b) barker 13; (c) USAF resolution target; (d) sierpinski carpet; (e) tapered grid design; (f) periodic lines.

The autocorrelation sensitivity is shown to vary between the different alignment marker designs. This is detailed in figure 2.5 which plots the lateral and magnification offsets separately, including the cross-correlation percentage values at the maximum

lateral and magnification offsets. Each alignment markers lateral cross-correlation is identical for both x and y translation axes, except for the USAF resolution target which varies between each axes.

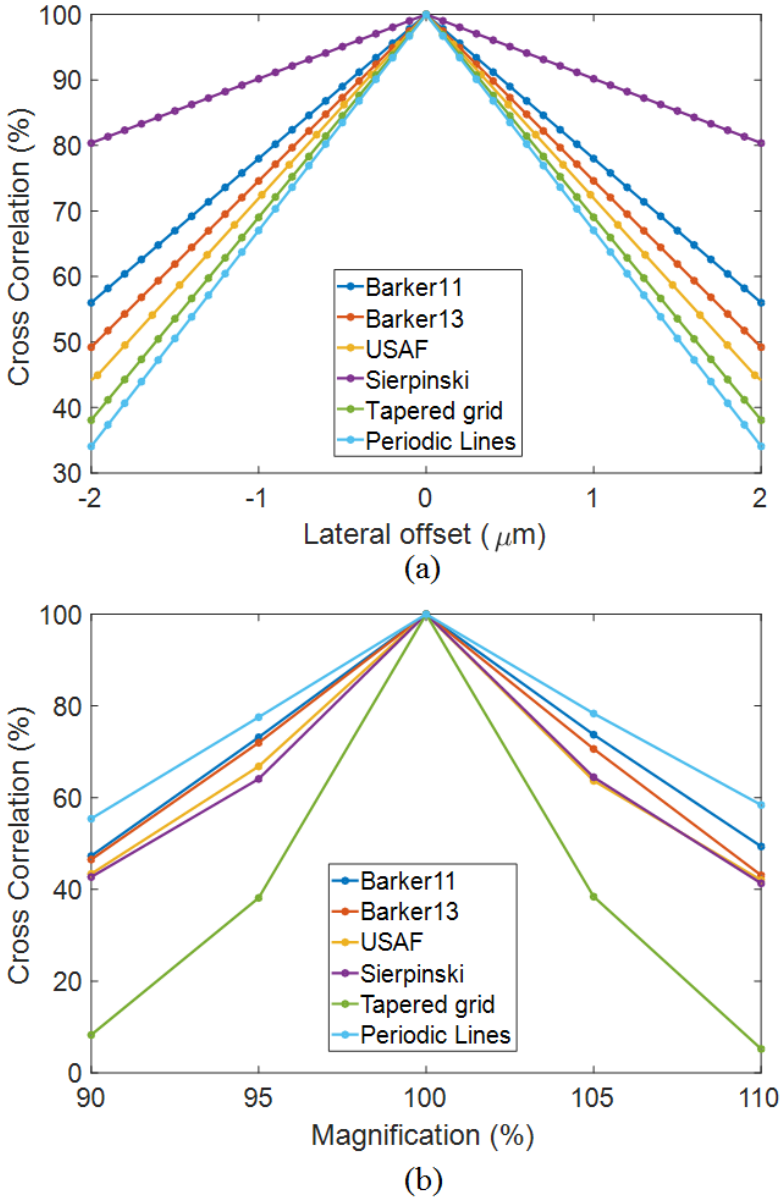

Figure 2.5: Each alignment mark design's comparative cross-correlation gradient drop as a function of (a) lateral offset; (b) magnification offset.

Two alignment marks have considerably higher autocorrelation sensitivity, the

Alignment mark cross-correlation strength		
	Cross-correlation strength value (%)	
Marker design	For a 2 μm lateral offset	For a 10 % magnification offset
Periodic lines	34.1	55.4
USAF res. chart	44.2	44.1
Sierpinski	80.4	42.7
Barker 11	56.0	47.3
Barker 13	49.2	46.5
Tapered grid	38.0	8.6

Table 2.1: Measured cross-correlation for alignment markers after a measured displacement offset for both lateral and magnification variations. Smaller cross-correlation values at the maximum offset and magnification positions correspond to sensitive marker designs.

tapered grid and periodic lines alignment markers, with respective cross-correlation values measured at the full lateral offset of 38.0 % and ∼34.1 %. The magnification cross-correlation value for the tapered grid shows a greater drop than the periodic line design detailing a higher aperiodicity in the design, with respective cross-correlation values of ∼8.6 % and ∼55.4 %. The performance of the marker can be further tested by increasing the lateral offset in order to measured any possible repetitions in the cross-correlation designs, which correspond to unwanted cross-correlation peaks. The theoretical plots are shown in figure 2.6 measuring the cross-correlation as a function of a further lateral offset of ±3.5 μm. The periodic line marker design delivers an increased cross-correlation value past the linewidth lateral displacement, whilst this is much less severe in the tapered grid which continues to drop in correlation strength. The tapered grid alignment marker design enables the ability to measure the variation in cross-correlation across a wide range of lateral and magnified offsets, with higher sensitivity than any other marker design. Further to this, as it is composed solely of micron-scale lines it allows a high yield fabrication with minimal defects. Given this performance, the tapered grid marker is used in the rest of the

work presented here.

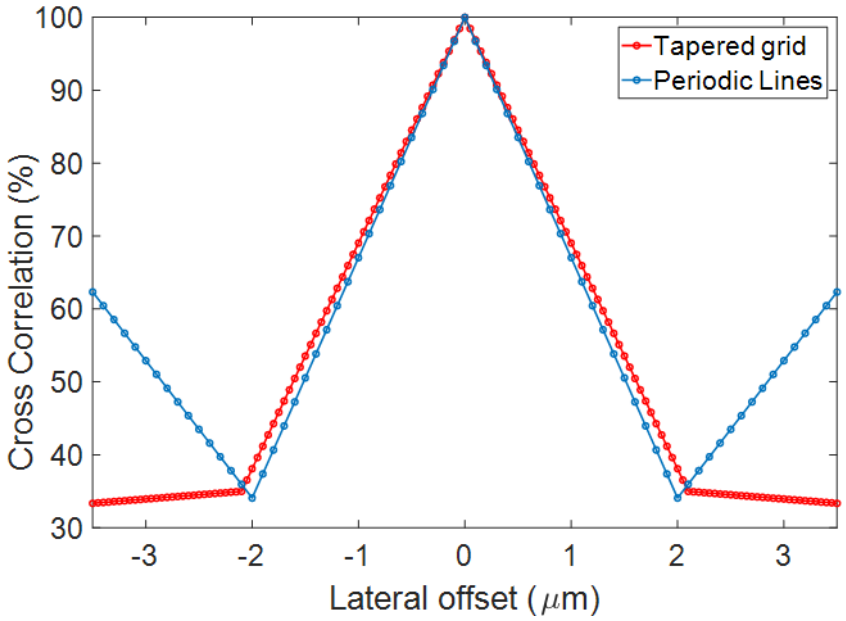

Figure 2.6: Comparison of the tapered grid and periodic line alignment mark design aperiodicity. This is achieved by expanding the lateral offset range in order to measure the pattern repetition within each design.

A fabricated grid alignment mark is shown in figure 2.7 which is used for all high accuracy transfer printing work throughout the thesis. It contains repeated lines with linewidths of 2 μm with a full marker area of 152 μm^2. The material platform is SOI, with the marker lines produced by fully etching the silicon core layer as to expose the silica cladding as to promote the line contrast. The pitch gradually increases from 4 μm to 22 μm in steps of 2 μm.

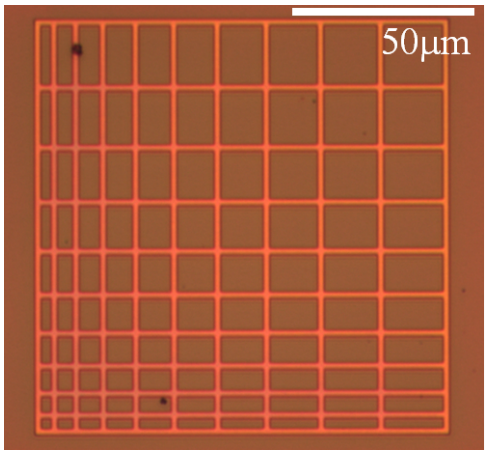

Figure 2.7: Top-view optical micrograph of tapered grid alignment mark fabricated within SOI chip.

2.3 TP system-to-chip alignment

This section details the operation of cross-correlation within the TP system. It will focus on the procedure required to align a single on-chip alignment mark to an absolute position relative to the system coordinate map. Techniques in achieving the relative displacement between both markers are discussed, followed by the development of the software used for processing the output correlation data and implementing alongside the TP method.

2.3.1 Absolute alignment

When it comes to alignment protocols, it is important to know the difference between relative and absolute alignment. An object's relative alignment corresponds to its position with respect to another object. Previous TP research has demonstrated relative structure alignment reaching nanoscale accuracies [41]. However, relative alignment requires the initial knowledge of an object's position in order to align with respect to it. This initial positional information is known as its absolute position. An object's absolute position does not take into account any other object. The absolute

alignment used in current TP (edge detection) is limited by factors including the optical resolution of the system, and fabrication defects in the utilised markers. The implementation of cross-correlation alignment could significantly reduce this limit, enabling TP with extremely high absolute alignment accuracies.

To utilise cross-correlation for TP, the process must provide the absolute position of an on-chip alignment mark (A) with regards to the coordinate map of the system. Therefore, the second alignment mark (B) must have a coordinate position known by the TP system. This is achieved by using a virtual alignment mark, which has a pre-determined position within the imaging FOV. Figure 2.8 shows both a top-view image of an on-chip alignment mark and an identical virtual mark with a known position within the same imaging window FOV. The virtual alignment mark image is created through MatLab image processing, therefore its position is known to the accuracy of the pixel resolution. By using the cross-correlation alignment method to measure both markers positional overlap, the relative displacement provides an absolute position of the on-chip marker to the TP systems FOV and therefore the translation stage coordinate map.

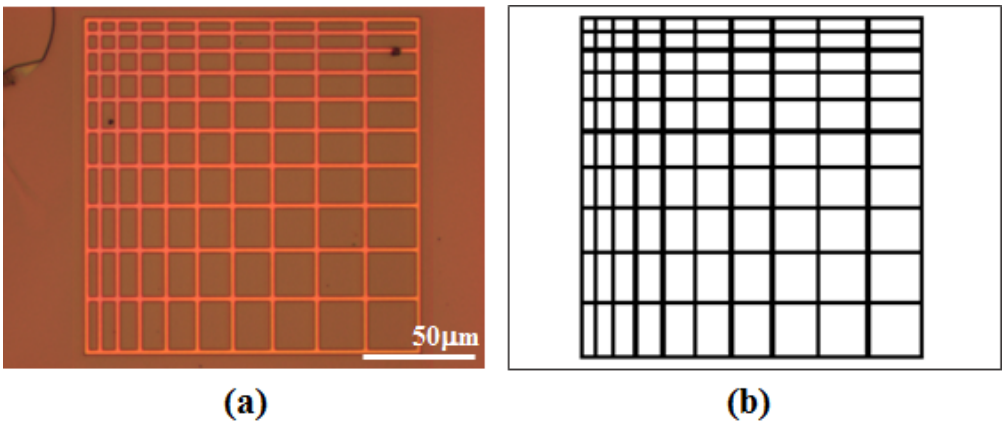

Figure 2.8: (a) Optical micrograph of fabricated alignment mark, captured from TP system's optical imaging system FOV. (b) Virtual alignment mark with known position within system FOV with which the fabricated marker image within (a) is cross-correlation against.

2.3.2 Marker alignment procedure

The cross-correlation is measured via a displacement offset. As such, prior to this a standard visual inspection of the marker alignment is carried out with an accuracy of ∼500 nm. This is implemented within the full range of translation required to carry out the cross-correlation procedure.

Standard overlay alignment A standard optical overlay alignment between the on-chip marker and virtual marker position determines the initial overlap position (δx,δy). The step accuracy is limited by the system resolution. As this is the case, the displacement offset used for cross-correlation must always be greater than a minimum ± 1 μm.

Cross-correlation alignment Once the overlay alignment is achieved, the marker-to-marker relative displacement is implemented. The direct measurement of the cross-correlation is achieved by measuring the similarity between the known pattern (virtual mark) against an integrated intensity image of the on-chip marker for

each individual displacement step. By tracking the displacement across nanoscale incremental movements, the variation in the marker cross-correlation strength can be plotted as a function of its displacement. Multiple plots over both horizontal and vertical axes are shown in figure 2.9. The positions of maximum similarity in the markers are detailed by the peak positions of correlation strength. The measured peak position is relative to the initial overlay alignment, therefore provides information on the absolute position of the alignment mark at the resolution of the incremental step size.

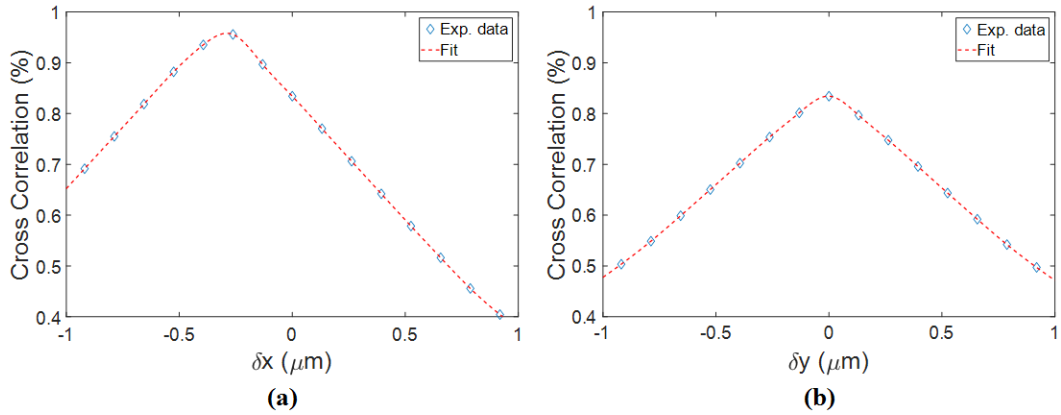

Figure 2.9: Plot of alignment mark images correlated against the virtual marker. Cross-correlation is measured as a function of lateral offset relative to the absolute position of the virtual marker detailing (a) cross-correlation in x-axis; (b) cross-correlation in y-axis.

By curve fitting the experimental data, the resolution can be further reduced by calculating the point of best fit without being constrained by the limited step sizes of the measurement technique. This is achieved by providing a fitting curve with the maximum possible overlap of the experimental data. This best fit from the calculated data trend enables a predicted maximum cross-correlation with a higher degree of accuracy than the experimental data output. There are multiple curve fitting algorithms which can be applied depending on the resolution and therefore

shape of the varying cross-correlation curve. These are a nonlinear least squares Gaussian fit, as shown in figure 2.9, or by linear fitting the two sides of the curve and calculating the intersect point corresponding to the maximum. The second method suits a sharper peaked correlation. However, when the cross-correlation curve starts to resemble a more Gaussian model, the Gaussian curve fit provides a more flexible fitting mechanism, suitable for lower resolution images.

2.3.3 Marker displacement techniques

Now that the cross-correlation method has been explained, mechanisms to provide the on-chip and virtual alignment mark relative displacements are investigated. The relative marker displacement can be achieved by different methods. Two are explained and used throughout this research: mechanical cross-correlation, which measures the cross-correlation alignment as a function of the systems translation stage lateral movements; and digital cross-correlation, which measures the cross-correlation alignment with regards to pixel offsets of the virtual alignment mark within the imaging windows FOV.

Mechanical cross-correlation As the sample is fixed to the TP systems translation stage, the displacement offset of the on-chip alignment mark can be achieved by controlled nanoscale incremental movements of the translation stage. The translation stage within the set-up has a lateral encoder resolution of 5 nm as well as a repeatability of ± 25 nm. As such, the sample can be accurately positioned below the systems optical resolution limit. By choosing lateral steps of 100nm, we minimize the measurement resolution size whilst reducing any positional errors from the translation stage repeatability error. The full process is described by a flowchart in figure

2.10. By using the stage, the alignment mark (A) is laterally translated around the virtual mark (b) which has a pre-registered position of δx,δy = 0. Each stage incremental movement is recorded by taking a top-view image of the alignment marks position within the imaging window. By cross-correlating each individual image to the stationary virtual alignment mark image the cross-correlation as a function of lateral translation is plotted.

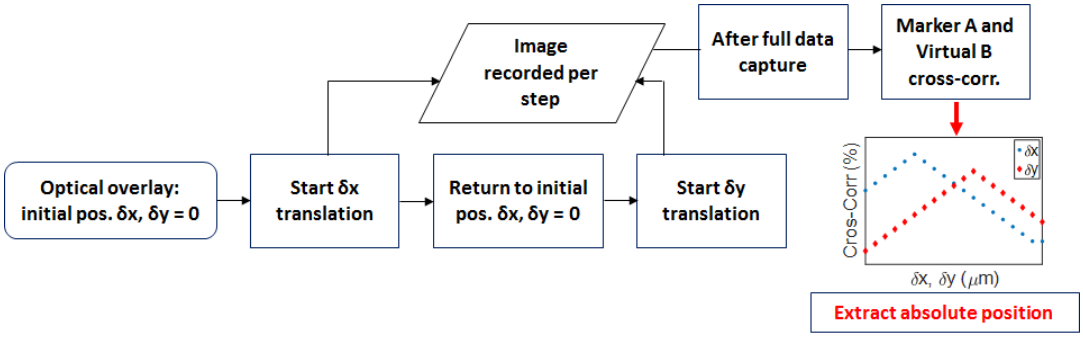

Figure 2.10: Flow chart describing the cross-correlation alignment procedure. This process utilises relative displacements of the translation stage in order to measure the variation in cross-correlation strength between an on-chip alignment mark and virtual mark.

Digital cross-correlation A second method follows the same principle, however using the high-resolution pixel size as a means to measure the variation in cross-correlation as a function of displacement.

This is achieved by recording the position of the on-chip alignment mark within the systems imaging FOV after the initial overlay alignment. By adding pixel offsets to the virtual alignment mark, its position within its imaging window is moved. As such, the variation in cross-correlation between the stationary alignment mark (A) as a function of the displaced virtual alignment mark (B) as a function of the pixel offset is measured, with the technique demonstrated in figure 2.11.

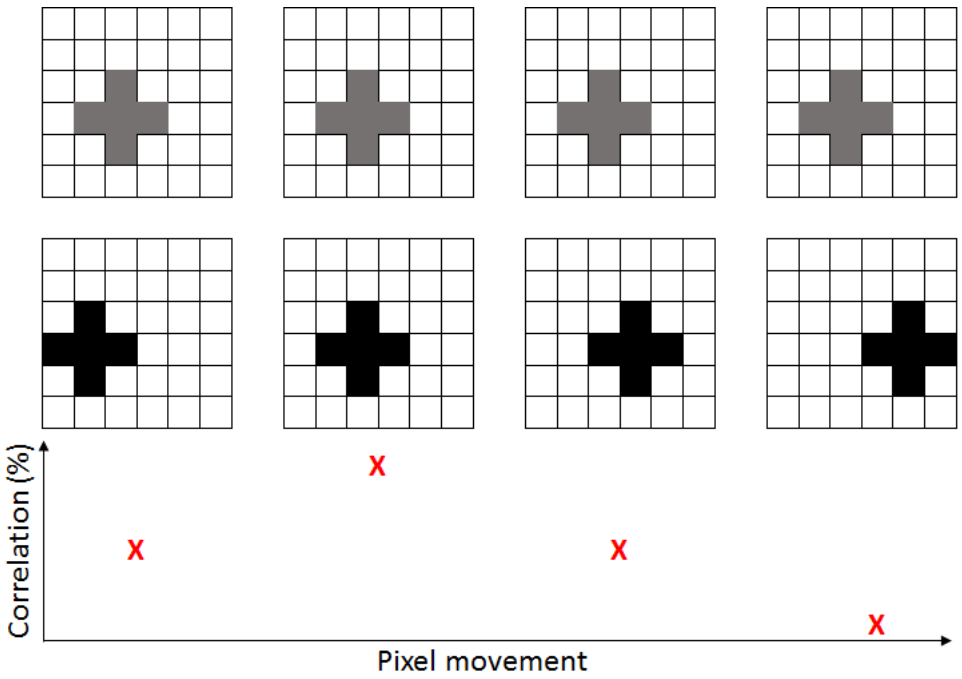

Figure 2.11: Variation in cross-correlation strength between an alignment mark (top; grey) and identical virtual mark (bottom; black) as a function of pixel offset.

This method requires an accurate measurement of the corresponding pixel size within the TP optical imaging system. This is achieved by calibrating the pixel size to an object of known dimensions. Figure 2.12 shows an optical micrograph and corresponding intensity line plot of a tapered grid marker. As the fabrication method used was EBL, the line pitch is known to an accuracy of several nm. By measuring the number of pixels from the centre-to-centre positions of each line and comparing against the pitch, we can determine very accurately the size of each pixel. The alignment mark rotation was corrected relative to the imaging system prior to the images being captured, such that rotational variations in the line separation does not give different measurements of the pixel size. The pixel size was measured multiple times per marker image for both x and y directions across the full scale of the marker, as well as for multiple magnifications of 80, 90, and 100 % optical magnification within the imaging system of the TP machine.

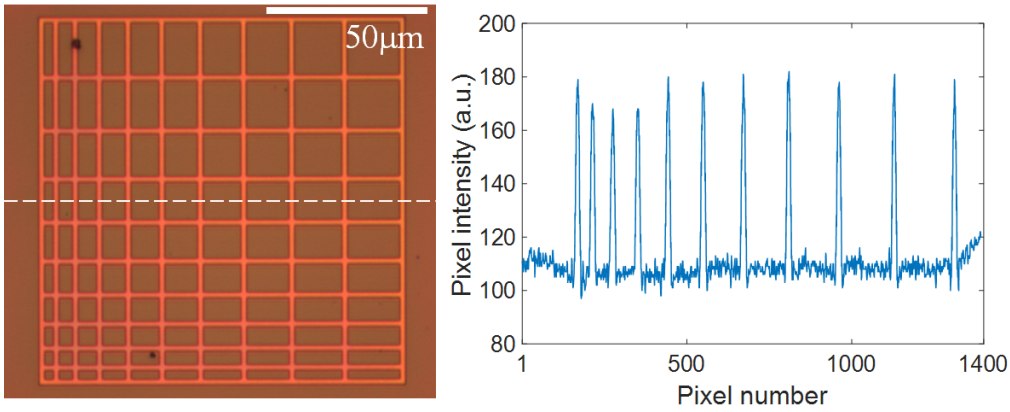

Figure 2.12: (a) Top-view optical micrograph of an alignment mark with a known linewidth of 2 μm and varying line pitch. (b) Line profile across alignment mark which plots RGB pixel intensity as a function of pixel number. The pixel number corresponds to each pixels position from left to right of image.

Table 2.2 details the different pixel sizes calculated as well as the standard deviations for the multiple optical magnifications of the system. It is also shown that the error in the pixel resolution is reduced as we increase the magnification, such that the higher magnifications will achieve a greater accuracy cross-correlation measurement.

Magnification and corresponding pixel size (nm)	
Optical magnification (%)	Average pixel size ± Std Dev.
80	157 ± 2
90	131 ± 1
100	109 ± 1

Table 2.2: Pixel size as a function of the optical magnification of the TP imaging system.

2.3.4 Software

The cross-correlation technique is programmed and implemented into the TP system using Matlab software, developed by the thesis author. A GUI interface is split up into several sub-GUI with the full interface detailed in figure 2.13.

The first sub-GUI (red dashed region) contains the image processing procedure

of the top-view FOV images containing the alignment marks. The process uses a Matlab image threshold function converting the bitmap image of the marker into a black and white representation. A threshold level is determined by the user which splits the pixel colour scale into either black or white. Following this, any dirt or unwanted features can be removed by an object size threshold. The user determines the size of the unwanted features as a function of the number of pixels they're composed of.

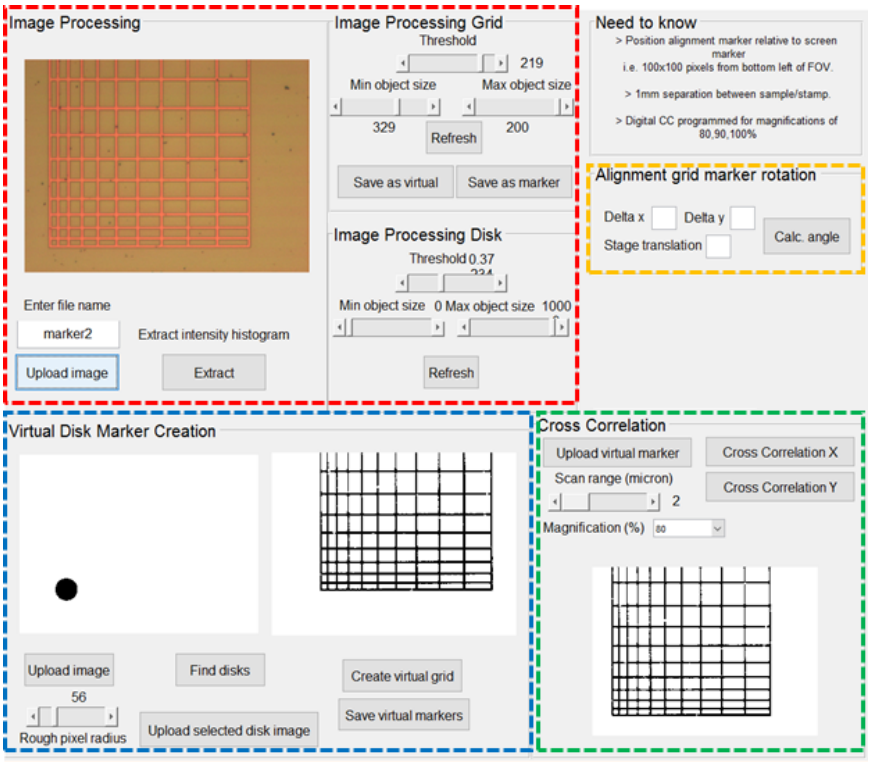

Figure 2.13: Screenshot of the Matlab GUI split into different zones; red: image processing tab, orange: sample rotation calculation, blue: virtual disk creation and green: cross-correlation tab.

A sub-GUI (orange dashed region) calculates the sample rotation. This is achieved by determining the lateral positional offsets of two identical fabricated on-chip alignment marks of a known distance with respect to the translated distance. This procedure is further detailed in section 2.4.1 where it is used as a measurement method

of the systems alignment accuracy. The equation for calculating the sample rotation is given by ($\theta = \arctan \frac{\Delta y}{x+\Delta x}$) where θ is the samples rotation angle, Δx and Δy are the measured lateral displacement offsets from the expected alignment position in the no rotation case, and x is the lateral translation of the stage to move between each marker as shown in figure 2.14.

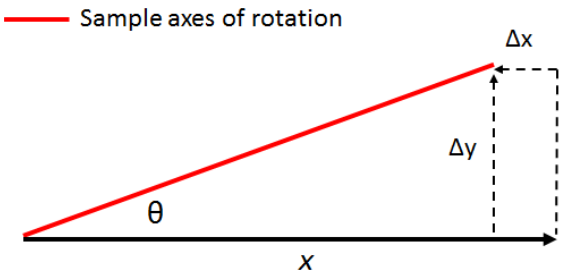

Figure 2.14: Diagram of sample rotation relative to stage rotation, containing parameter sets for calculating the sample-to-stage rotational offset.

The blue dashed region of figure 2.13 contains a sub-GUI used for the process of aligning micro-disk objects free-standing on their native substrates with the alignment marks. This is explained in section 2.6.1 however uses the same image processing method as the standard multi-chip alignment mark protocol. The final sub-GUI (green dashed region) controls the cross-correlation procedure, where the virtual mark is uploaded and the displacement scan length is chosen when using the digital cross-correlation method.

2.4 System alignment accuracy

This section details the experimental measurement of the system alignment capability. Two complementary methods are studied. First, the accuracy of detecting a pre-defined position within the TP system is assessed by the alignment of two identical markers. The markers are fabricated within the same lithographic step on

a single sample and have a known separation to the accuracy of the EBL fabrication error. By translating the sample between each marker by our known separation we can calculate their positional offset - as a function of the system-to-stage rotational misalignment - using the cross-correlation alignment procedure. The comparison of multiple positional offset measurements calculates the absolute error within the alignment procedure. Second, the accuracy of depositing two physical structures with a target separation on a single sample is assessed. The two structures are created by physically marking lines into a soft photoresist layer using a micro-tip array, where the position of each structure is determined by using cross-correlation alignment with respect to a single marker. The positional accuracy is measured using standard AFM technology with the calculated error in the separation a direct measurement of the system's absolute alignment accuracy.

2.4.1 Positional alignment accuracy

The measurement utilised a SOI sample containing EBL fabricated grid alignment markers spaced by a distance of 2 mm, with one shown in figure 2.15a. Any separation error is a factor in the fabrication, estimated at the nanoscale, an order of magnitude below the predicted measurement accuracy. The aim is to calculate the positional offset of two alignment marks after each are translated to the centre-point of the camera FOV by the known separation. The measured misalignment offset will be a combination of both the error of the alignment technique and a lateral offset due to the sample-to-stage relative rotation. Repetition of the measurement procedure will disentangle both offsets, as any residual deviations across multiple scans is dependent on the error in the cross-correlation alignment.

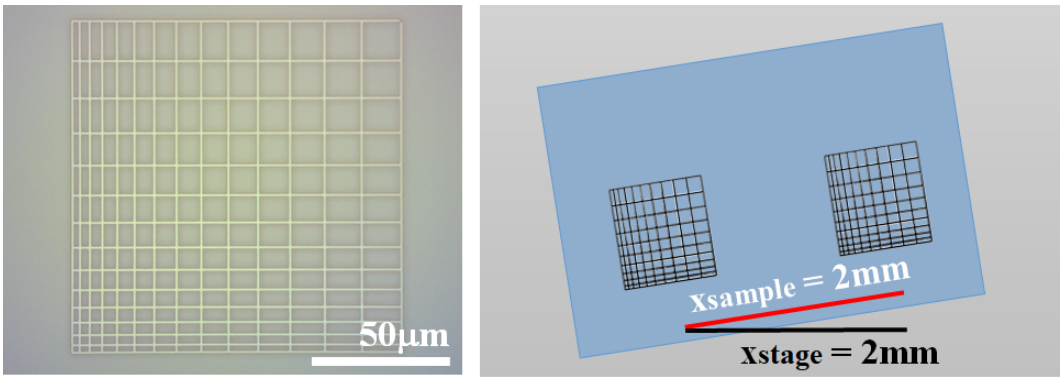

Figure 2.15: (a) Optical micrograph of a fabricated alignment marker. (b) Schematic illustration of a sample containing two identical on-chip alignment marks with a known separation of 2mm with a relative rotational offset between the sample and stage.

The marker-to-marker positional offset calculations for repeated measurements is shown in table 2.3. An overall alignment accuracy of 56±37.5 nm for the x-axis and 45±29 nm for the y-axis is achieved.

Positional error using cross-correlation alignment method.		
Meas. number	Error: x-axis (nm)	Error: y-axis (nm)
1	90	10
2	10	70
3	80	10
4	90	67
5	11	70
Average error ± Std dev	56±38	45±29

Table 2.3: Calculated alignment error values for both axes. Alignment error offset has been separated from rotational offset by multiple measurements.

2.4.2 Structure deposition accuracy

Prior to the modification of the dip-pen nanolithography system for TP its function was to enable the deposition of controlled amounts of materials onto surfaces by use of silicon nitride probe tip arrays [47]. By using these probe tip arrays in the modified set-up it is possible to produce physical indentation lines on a sample with

the same positional accuracy as the TP pick-and-place procedure. This technique enables the direct measurement of objects aligned by cross-correlation.

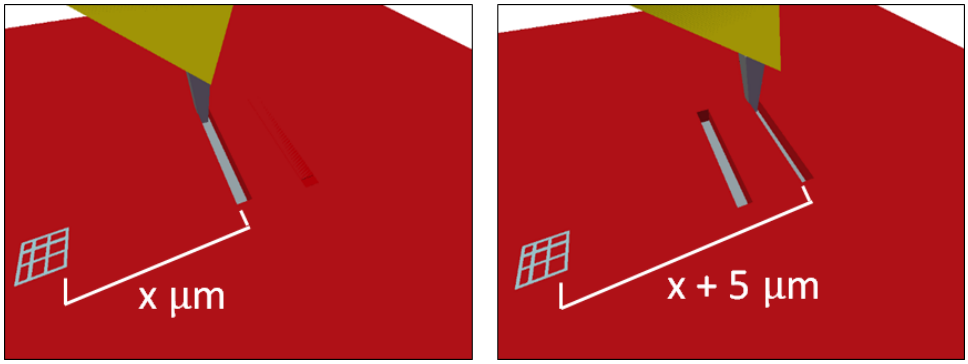

Figure 2.16: Schematic illustration of probe tips physically patterning controlled indents into the photoresist layer. The indent positions are relative to an alignment mark absolute position within the sample.

A schematic of the process is shown in figure 2.16. Alignment marks are patterned into a positive S1805 photoresist layer by direct-write laser lithography with their absolute position measured by cross-correlation. A physical indentation line is then formed at a position relative to the alignment mark using the micro-tip array. This is achieved by first making contact between the photoresist layer and the probe tips before physically dragging the tip through the resist in the axis perpendicular to the target separation. Multiple lines are produced in separate alignment steps with a target separation of 5 μm. The separation is measured by using atomic force microscopy (AFM) technology and compared to the expected separation.

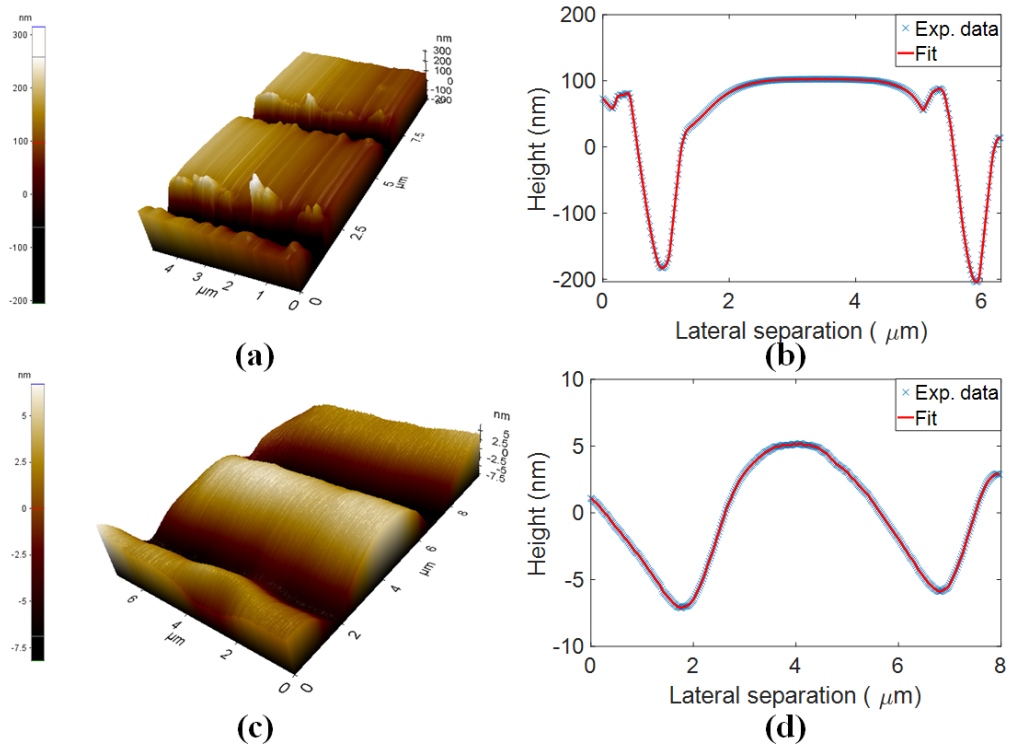

Figure 2.17: (a) and (c) are 3D topographic images obtained by AFM scan measurement of micro-tip indentations with controlled separation; (b) and (d) are respective line profiles of the two relatively aligned indentations.

3D AFM topographic scans of the two indent lines are shown in figure 2.17. Figure 2.17a details two lines which penetrate the photoresist to a depth of roughly 300 nm. The respective line profile of the 3D plot is shown in 2.17b in which the trough height is calculated as a function of the lateral separation. The same process is achieved for a second probe tip with a reduced penetration depth, figure 2.17c and d. Due to the separation being measured from the minimum height in the scan the difference in probe tips will not affect the measurement accuracy. The lateral resolution of the AFM is ≈30 nm, limited by the AFM probe tip shape. However, the measurement resolution is further reduced by curve fitting the measured data. Multiple measurements spanning the full length of the lines take into account any rotational offset or fluctuations from unexpected shifting of the probe tip during its

movement through the photoresist. The average positional error over multiple tests is calculated as 45nm with a standard deviation of ±40 nm.

AFM alignment error calculations: Target separation is 5 μm	
Scan 1: Measurement number	Positional error (nm)
1	20
2	0
3	20
Scan 2: Measurement number	Positional error (nm)
1	68
2	110
3	50
Average error ± Std dev	45 ± 40

Table 2.4: Experimentally measured positional offset, measured as the difference between the experimental separation and target separation of 5 μm.

Both measurement techniques are promising in that they show sub-100 nm alignment accuracies. The next stage will be measuring the implementation of the alignment procedure with the actual TP of devices between multiple chips.

2.5 Chip-to-chip alignment

In micro-fabrication the alignment marks are typically written in the same step as the first level patterned devices, this provides an absolute coordinate map of each on-chip device with a known position relative to the alignment marks. Therefore, by calculating the absolute position of an on-chip alignment mark as a function of the TP system, effectively we know the relative coordinate positions of all on-chip devices with an alignment accuracy determined jointly by the lithography resolution and the alignment procedure. This procedure can be utilised for multi-chip procedures. By aligning each chips marker to the same virtual alignment mark, their absolute positions are calculated relative to each other to the accuracy of the measurement

technique. Therefore, the positions of all devices across both chips are calculated within the same system coordinate map.

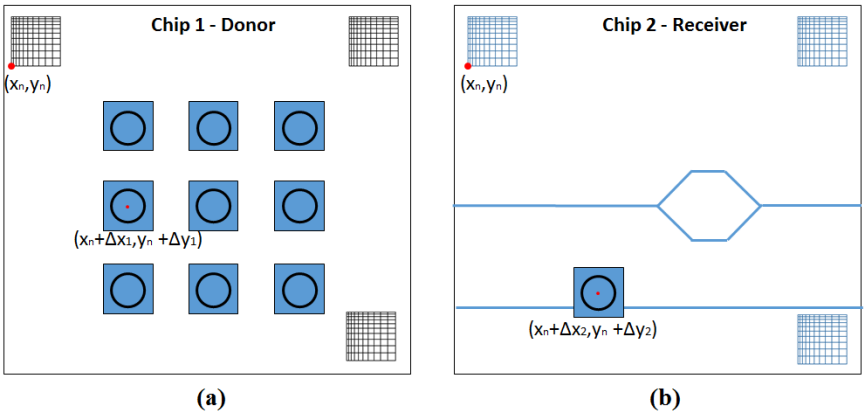

Figure 2.18: (a) Illustration of a donor chip containing alignment marks and suspended membrane devices with relative on-chip. (b) Receiver chip containing identical alignment marks and relative positioned devices. Membrane devices are bonded to receiver chip relative to the absolute alignment mark position.

This is shown in figure 2.18 where the positions of two devices on separated chips, device (1) and device (2), are known by $x_n + \Delta\ x_{1,2}$,$y_n + \Delta\ y_{1,2}$ where x_n,y_n corresponds to the shared alignment mark system coordinate point. In order to compensate for the variations in rotation across both donor and receiver chips, a three-point cross-correlation alignment is measured using three alignment marks placed across the two chips with known lateral separations. Their absolute rotations (θ) are calculated to determine the relative rotational offset ($\Delta\ \theta$) to the TP system, which is minimized using the TP systems rotation stage. By implementing this technique alongside TP, devices can be accurately moved between different substrates with a positional accuracy of the cross-correlation procedure. The following section details the systematic analysis of the achievable alignment accuracy of chip-to-chip TP.

2.5.1 Device transfer printing

The TP of a large array of membrane devices to a receiver substrate is discussed, followed by statistical analysis of the obtainable alignment accuracy. The membranes are individually printed, with both lateral axes and the rotational accuracy measured per device to obtain an overall accuracy.

Vernier alignment measurement

To precisely measure the lateral and rotational accuracy, a vernier calibration scale is applied, depicted in figure 2.19. The advantage of using a vernier scale comes from the ability to magnify small variations in the displacement through the beat frequency of two vernier gratings with slightly different periodicities. The obtainable resolution comes from the variation in the line pitch, such that if the top vernier pitch is P_1=1 μm and the bottom vernier pitch is P_1=1.1 μm the vernier resolution, known as the vernier constant, is 0.1 μm. A displacement offset is calculated by observing which lines are co-incident between the top and bottom scales. The vernier scales used for this work are composed of lines with linewidths of 500 nm, P_1 and P_2 are 1 μm and 1.1 μm, and N_1 and N_2 are 12 and 11, respectively. This gives an overall vernier constant of 100 nm resolution. Both lateral and rotation misalignments are measured by using the vernier design shown in figure 2.19b.

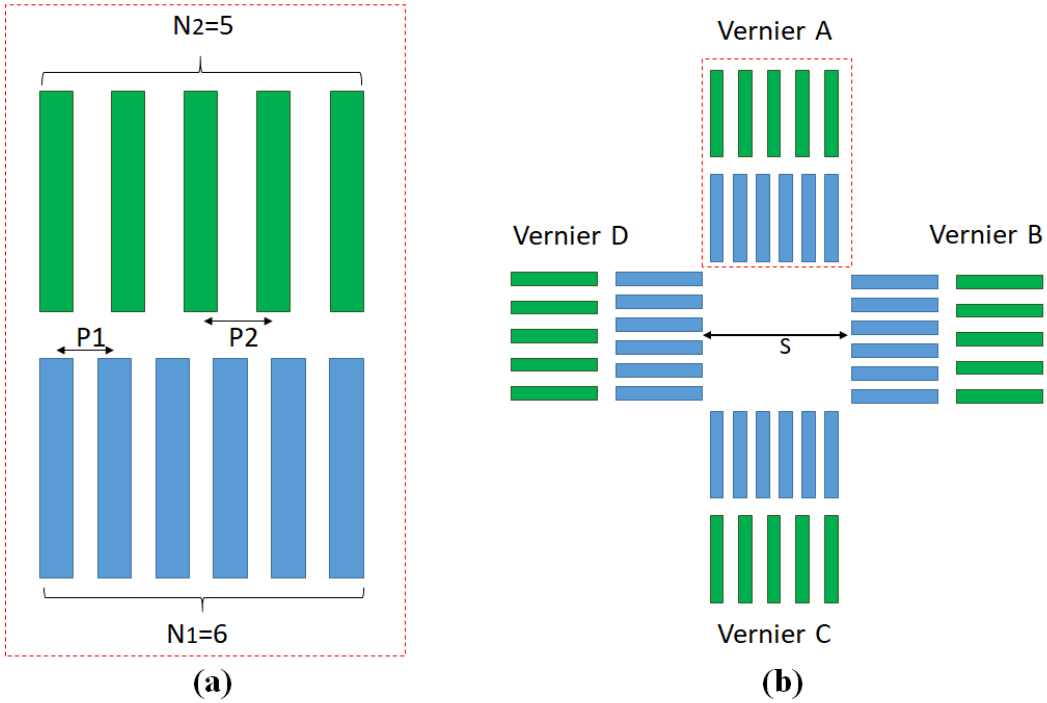

Figure 2.19: (a) Schematic illustration of a vernier scale detailing the pitch differences P_1 and P_2, and the number of lines N_1 and N_2 for the main scale (blue) and vernier scale (green). (b) Vernier calibration scale for lateral and rotational offset measurements, composed of four vernier scales at a 90 degree offset to each other. Scale separation (S) is labelled alongside each scales corresponding letter.

It consists of four scales of identical dimensions each rotated by a 90deg offset. The lateral and rotation displacement misalignment are interpreted from the vernier scale using:

$$Horiz. = \frac{\Delta x_A - \Delta x_C}{2}, \tag{2.2}$$

$$Vert. = \frac{\Delta y_D - \Delta y_B}{2}, \tag{2.3}$$

$$Rot. = tan^{-1}\frac{\Delta_{H,V}}{S}. \tag{2.4}$$

$\Delta x_{A,B,C,D}$ and $\Delta y_{A,B,C,D}$ correspond to the measured displacement offsets for

each vernier scale, labelled in figure 2.19b. The scale separation distance is given by S, with the separation of vernier scales A and C identical to the separation of vernier scales B and D. The final parameter set is the overall horizontal and vertical misalignments, ΔH and ΔV, which are a measure of the difference between the individual measured displacements for both separate axes ($\Delta H = \Delta_{xA} + \Delta_{xC}$ and $\Delta H = \Delta_{YD} + \Delta_{YB}$).

Membrane devices

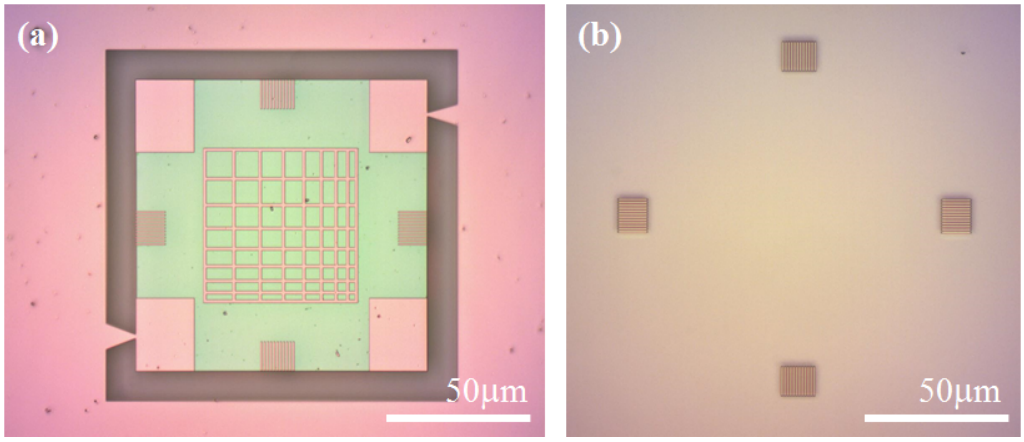

Figure 2.20: Optical microscope images of (a) a suspended Si membrane containing main scale divisions; (b) receiver substrate with corresponding vernier scale divisions.

The micro-assembled devices used for the alignment experiment are ultra-thin (220 nm) silicon membranes. Vernier scale marking are patterned into the devices by shallow-etching (to a depth of 70 nm) alongside an alignment mark and support structures at the corners reinforcing the device anchors. The anchors suspend the membrane above the substrate and taper from 9 μm at the substrate to 1 μm contacting the membrane. A full description of the fabrication procedure is given in chapter 3.

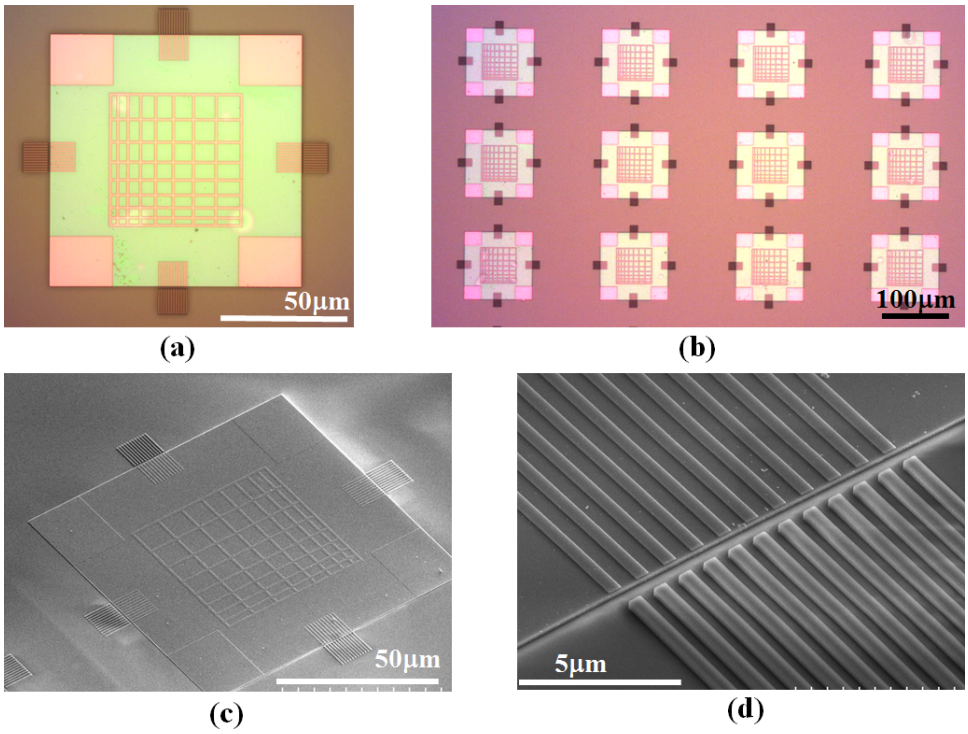

Figure 2.21: (a) Transfer printed single membrane device aligned to receiver vernier scale. (b) Array of printed membrane devices on receiver chip. (c) Angled SEM image of a printed device. (d) Magnified SEM image detailing single aligned vernier scale of printed device.

Figure 2.20 contains images of both a single silicon membrane suspended on the native SOI platform and the corresponding vernier scale markings on the receiving SOI substrate. The receiver is fully etched to the silica layer with the vernier marks patterned into the remaining silicon top layer. Overall there were 20 devices individually TP onto the receiver chip. A single membrane device as well as a section of the finished array are shown in optical micrographs in figures 2.21a,b post printing. Further to this, there are SEM angled images captured of a single membrane detailing the ultra-thin nature of the membrane device and the etched vernier markings on both the shallow-etched membrane and fully etched receiver in figures 2.21c and d.

Results and analysis

The characterisation of the alignment accuracy involved the production of top-view SEM images of the four vernier scales on each edge of the membrane devices, these are shown for one device in figure 2.22.

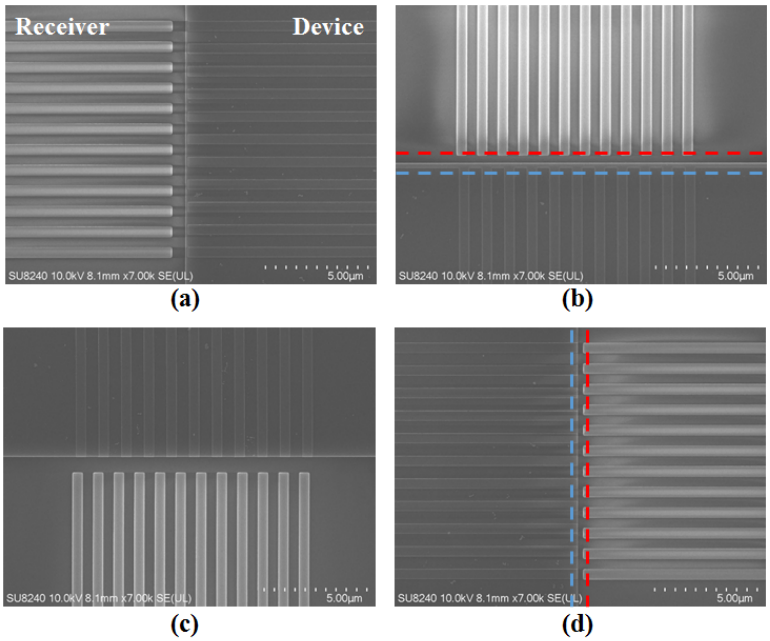

Figure 2.22: Magnified SEM images of the vernier scales on each edge of the membrane and receiver for characterisation of the alignment accuracy; (a) left; (b) top; (c) bottom; (d) right

Figure 2.22 shows the magnified images of the aligned vernier scales on the membrane and receiver, where the horizontal misalignment is measured by (b) and (c) and the vertical misalignment is measured by (a) and (d). The calculated offsets for all four are combined when measuring the overall rotational misalignment, equation 2.4. The exposure dose variation, produced by SEM charging from the silica insulating substrate, reduces the reliability of line edge measurements. However, the line spacing is unaffected by such problems. Therefore the measurements utilise the pitch variation over the two vernier scales to measure any misalignment. Figure 2.22b &

c contains dashed lines situated at the edges of both membrane and receiver scales, indicating the positions used during the cross-correlation alignment process. By producing an intensity profile across both the main and vernier scales, the equivalent centre-points of the vernier lines were calculated.

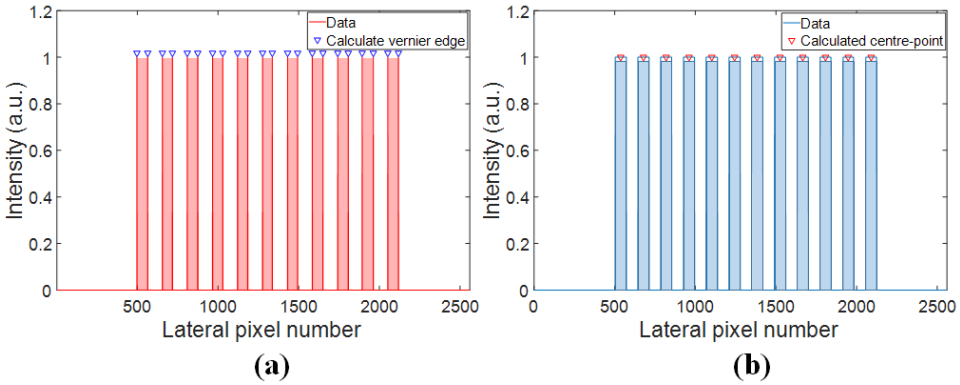

Figure 2.23: Intensity profiles calculating pitch and corresponding misalignment for both (a) shallow-etched membrane vernier marks; (b) receiver vernier marks.

Figure 2.23 shows the intensity profiles of the corresponding verniers with the calculated edges and centre points. An accurate measurement of each scale's positional misalignment ($\Delta\ x_{A,B,C,D}$) was produced by calculating the accumulated top and bottom scale lateral displacements, with the corresponding lines having an expected misalignment dependant on the variation in the pitch ($\Delta X_i, Y_i = \Delta P \sum_{i=1}^{N} N_i$). ΔX_i and ΔY_i are the manufactured vernier scale displacement offsets provided by a perfect alignment, with ΔP the difference in the two vernier scale pitches given by $\Delta P = P2 - P1$. Comparing the vernier misalignment as a function of the expected misalignment calculates the membrane's displacement offset:

$$\Delta x, y = \frac{\delta X_i, Y_i - \sum_{i=1}^{N} \delta x_i, y_i}{N}, \tag{2.5}$$

where N is the total number of vernier lines and $\delta_{xi,yi}$ the calculated vernier

misalignment. Using the above method has produced a set of lateral and rotation misalignment measurements for each of the 20 printed devices, detailed in figure 2.24.

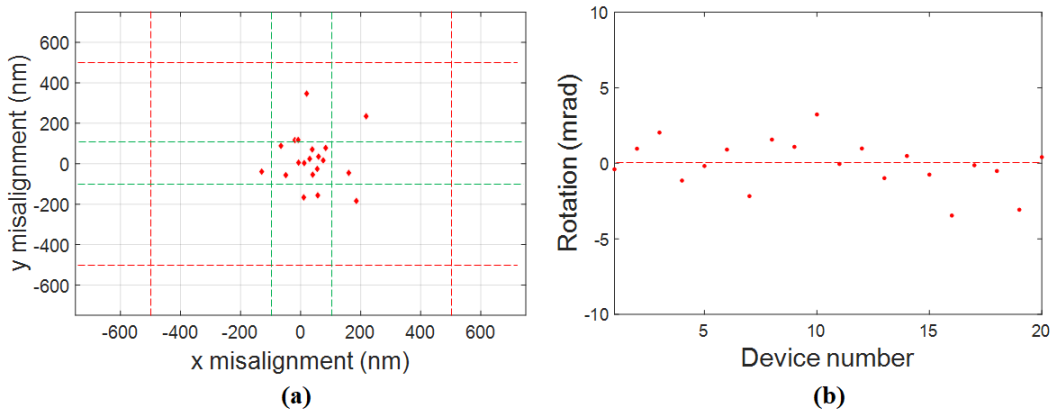

Figure 2.24: (a) Lateral misalignment measurement for the printed membranes detailing the 100 nm boundary (blue dashed lines) and 500 nm boundary (red dashed line). (b) Rotational misalignment of all devices.

The red dashed area in figure 2.24a contains the experimental data below the ±500 nm lateral misalignment limit whilst the green dashed area contains the below ±100 nm lateral misalignment data. The rotational misalignment in figure 2.24b details the rotational error for each device, with the rotation centred around the zero rotation error point. The lateral and rotation alignment offset average error analysis is given in table 2.5 with a maximum lateral offset measured at ±385 nm (3σ), the best achieved alignment accuracy for the TP method to date when compared against the current state-of-the-art (±1.5 μm (3σ)) [85, 46]. The significant improvement of this method presented here over the current state-of-the art in the literature is due to the use of a cross-correlation alignment scheme rather than edge detection overlay schemes. Edge detection schemes suffer from two main limitations. Firstly, the accuracy of the marker position registration is limited by the optical resolution of the microscope and computer aided edge detection algorithms, typically in the few

hundreds of nanometres region. Secondly, the markers themselves must be fabricated by lithography, so any errors in their geometry, and in particular their edge positions, will have a negative effect on the achievable position registration accuracy. The technique detailed in this thesis overcomes these issues by using the cross-correlation technique on carefully designed, non-repeating, asymmetric registration marks. This removes the requirement for accurate detection of lithographically defined edges, instead using a distributed pitch registration. Furthermore, the cross-correlation relies on the accuracy of the translation stage to detect the correlation function peak, again removing the dependence on the microscope resolution and allowing positional accuracy beyond this limit.

Averaged alignment offsets			
Axis	Average error	Std dev	3σ
Horizontal (±nm)	38	83	248
Vertical (±nm)	20	128	385
Rotational (±mrad)	0	2	5

Table 2.5: Lateral and rotational alignment calculations.

2.6 Alternative cross-correlation alignment methods

2.6.1 Free-standing micro-disk alignment

The high accuracy alignment method depicted so far has been aligning multiple samples with positions relative to identical alignment marks situated on both donor and receiver. However, free-standing structures on substrates containing no alignment marks requires an alternative method for producing high precision positional alignment across multiple samples. This section details the alignment procedure for the high accuracy alignment of free-standing micro-disk structures to alignment marks

fabricated on non-native chips.

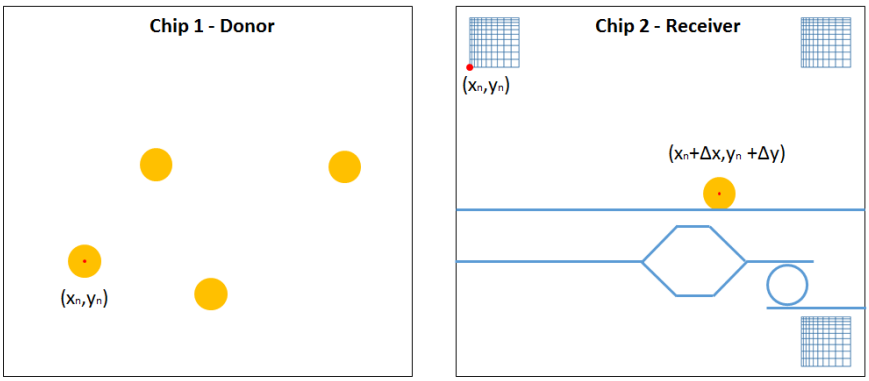

Figure 2.25: Schematic illustration of the micro-disk alignment method shown (a) donor substrate with free-standing micro-disks; (b) receiver containing alignment marks and relative waveguiding devices.

The method involves determining the centre-point of a micro-disk within the imaging system's FOV window, based upon its pixel position (x,y), shown in figure 2.26a. Following this, an alignment marker's position is determined within the same FOV, with the pixel position of the bottom left corner of the marker measured as (a,b), figure 2.26b. The alignment marker image is altered by translating the full marker design until the bottom left corner position aligns up to the same pixel position of the disk centre-point. This new virtual marker image (2.26b, vi) can then be used to align further alignment markers within the receiver chip to the position of the micro-disk, based upon the disk's absolute position within the TP coordinate system. A detailed description of each stage of the full process is explained in further detail.

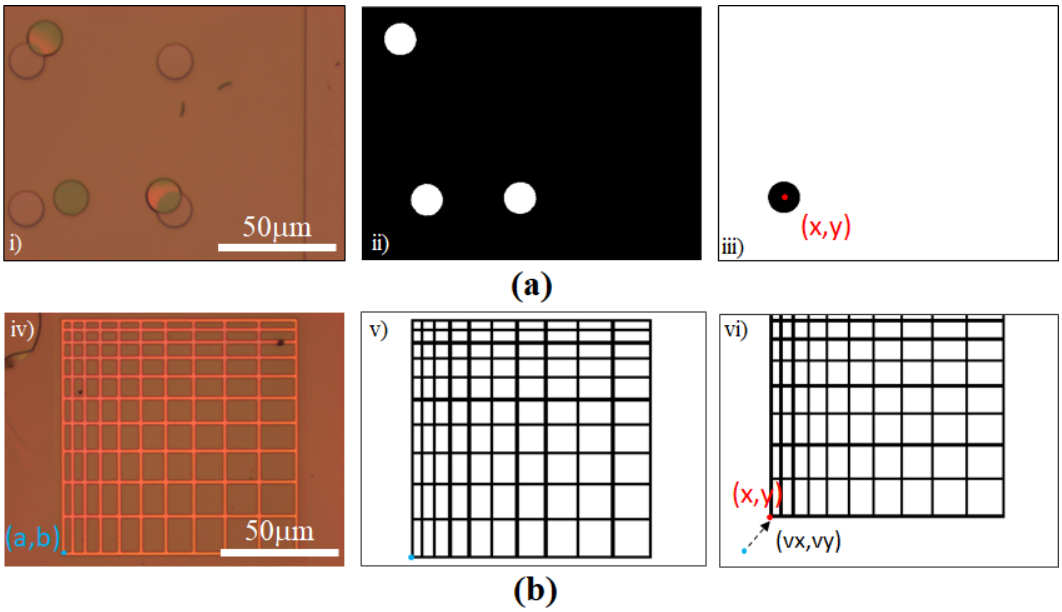

Figure 2.26: (a) Image processing technique for identifying micro-disk centre position within FOV in which (i) is a microscope image of disks and substrate, (ii) the binary mask of disks within FOV and (iii) binary mask of the individually selected disk with calculated centroid position. (b) Re-positioning of virtual alignment mark such that absolute position coincides with the selected micro-disk centre-point, with (iv) a microscope image of the alignment mark, (v) binary mask of the virtual alignment mark and (vi) the binary image of the virtual alignment mark after it has been translated within FOV with the left corner pixel position corresponds to the centroid of the disk.

i) and iv) Capture images of the micro-disks and alignment marker on their native substrates within the systems FOV. With regards to the randomly distributed nature of the micro-disks during the fabrication process, multiple micro-disks are captured with random placements within the imaging window.

ii) All stray objects and background colour are removed using a simple MatLab threshold function, based upon the grayscale intensity level of the image. By setting a level just below the intensity of the micro-disks all other objects can be set to black whilst anything above this level (micro-disks) are set to white. Stray objects, such as dirt or etch lines, are removed by setting a minimum object pixel size. The same process is utilised for the alignment marker, v).

iii) A Matlab function is utilised which finds circles using a circular Hough transform image processing technique. This function is used to detect circles in images and calculate their central position (a,b) and radius (r), using the equation $(x_n - a)^2 + (y_n - b)^2 = r^2$ where (x_n,y_n) are a number of points (n=1,2,..,i) positioned along the outer perimeter of the detected circle. Multiple circles of radius r and centre positions (x_n,y_n) are formed along the perimeter of an original circle formed within the main image. All the intersection points of each perimeter circle are determined, with the maximum number of intersection points corresponding to the centre position of the original circle (a,b) [86].

vi) The final stage is the movement of the alignment marker within the imaging FOV. This is achieved by calculating the coordinate difference (vx,vy) of the alignment marker corner and micro-disk centre, by vx = x-a and vy = y-b. A new image is formed with the alignment marker translated by this coordinate difference, such that the corner pixel position is now (x,y).

The alignment method explained has been used for the micro-assembly of AlGaAs micro-disks resonators to Si waveguides situated on a non-native SOI platform. As part of this work, an AlGaAs micro-disk is laterally aligned to a waveguide with a placement accuracy below 100 nm (137±4 nm with a target separation of 100 nm). The described alignment accuracy enables the production of an evanescent coupled hybrid AlGaAs-SOI micro-disk resonator [87]. A full analysis of this work is provided in chapter 4.

2.6.2 High precision alignment for selective nanowire integration

NW lasers are highly promising candidates for active components within nanophotonic systems for their sub-micron geometries. This has been realised by the ability to integrate across a wide range of material platforms, made possible by transfer printing [88]. In order to provide optimum lasing conditions, a high material quality and tight dimensional tolerances are required. However, the presence of slight fabrication inhomogeneities across a full wafer can cause large variations in the individual NW optical properties, this can be an issue for the integration of single NW lasers to integrated photonic systems where applications require the highest possible quality devices. An optical characterisation technique has been previously established which can statistically analyse each individual NWs quality and position across a full sample [89]. By implementing alongside high precision transfer printing individual NW integration can be achieved. The authors contribution to this section includes the on-chip alignment mark fabrication, and corresponding alignment procedure enabling high accuracy chip-to-chip TP of the NW lasers to pre-registered positions.

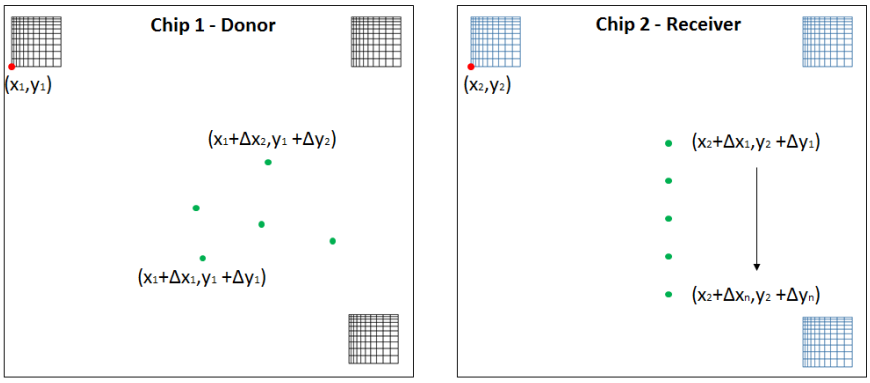

Figure 2.27: (a) Schematic illustration of donor with alignment marks absolute positions relative to NW lasers. (b) Schematic illustration of receiver containing the transfer printed NW lasers with relatively aligned positions corresponding to the alignment marks.

Using imaging and low power photoluminescence charcterisation of individual NWs across a full sample, their positional information can be catalogued in relation to fabricated alignment marks. Based on each NWs dimensions and lasing parameters, optimised NWs can be selected and transfer printed to a second substrate where they are released with high precision accuracy to corresponding alignment marks, this is detailed by a schematic representation in figure 2.27.

Figure 2.28a shows top-view optical images of the substrate containing a large number of randomly positioned NW lasers. The inset contains an alignment mark which is fabricated on the same substrate. The NWs are distributed randomly across the substrate prior to optical characterisation, demonstrating the importance of the alignment technique in order to select and find the specific NWs of interest. As well as recording their relative position, the optical characterisation provides further details such as their orientation, threshold and peak laser wavelength. A selected group of NWs, selected based upon their similar optical properties, are detailed in table 2.6.

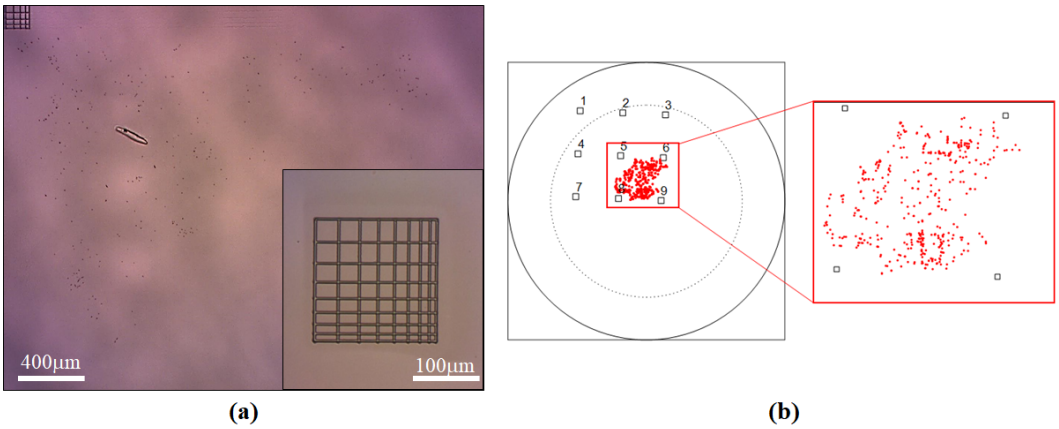

Figure 2.28: (a) Optical micrograph of NWs randomly spread across substrate (inset contains a fabricated alignment mark). (b) Schematic of full sample with measured NW positions relative to a formation of nine alignment marks. Red spots correspond to the measured positions of every recorded NW laser distributed across sample with numbered squares the alignment mark positions.

The selected group were moved along with four other groups to the receiving substrate chip, where they were printed in relation to a pre-fabricated alignment mark, shown in figure 2.29. As the orientation is known, the rotational control within the TP system can control the final orientation of the NWs.

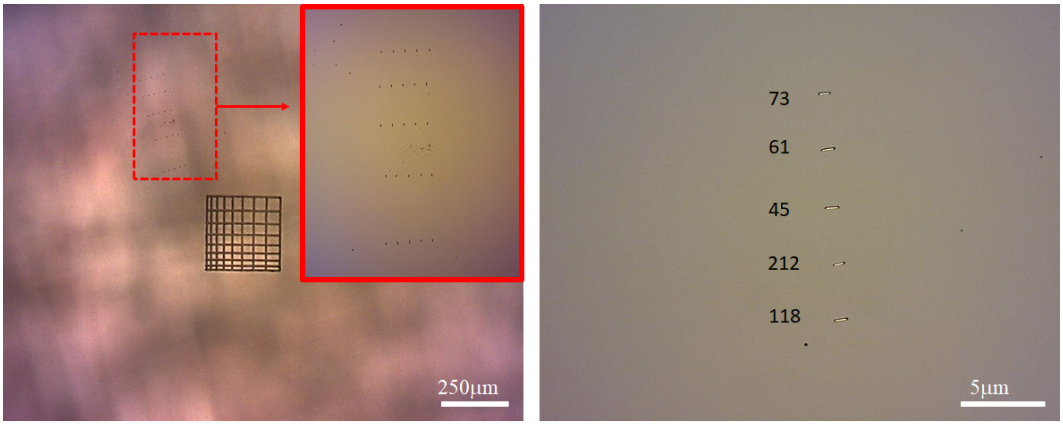

Figure 2.29: (a) Optical micrograph of pre-selected NW lasers selectively transfer printed. The sample contains five arrays of five NWs each; (b) Magnified image of a single NW laser array with the corresponding NW recorded numbers.

NW parameters				
NW #	Relative pos: x,y (μm)	Orientation (deg)	Lasing λ (nm)	Threshold ($\mu J/cm^2$)
45	-1.5, -2.9	320	771.1	428
61	-1.8, -2.8	77	759.8	428
73	-1.8, -2.8	310	771.1	428
212	-1.9, -2.6	41	780.2	395
118	-1.3, -3.1	82	792.3	362

Table 2.6: Selected NW lasers with recorded positions alongside their measured wavelength and lasing thresholds.

By combining this method with the cross-correlation alignment procedure, we have been able to selectively picked NWs with chosen properties and moved them to non-native substrates with extremely high positional placement. This section gives an overview on the alignment procedure used in order to transfer print pre-selected NWs across multiple chips, alongside the analysis and characterisation of the NWs pre- and post-printing. The section focuses mostly on the alignment procedure, however a continuation of the collaborative work is provided within appendix B.

2.7 Conclusions

This chapter discusses the implementation of a cross-correlation alignment procedure for the high accuracy chip-to-chip movement and integration of devices using the transfer printing method. It contains an explanation on the cross-correlation method used throughout the work. This includes discussing the procedures in place to fully implement within the TP system for the chip-to-chip transfer printing of pre-fabricated suspended membrane devices, as well as alternative device geometries from free-standing micro-disks to NW lasers. Further to this, the comparison of multiple alignment mark designs is carried out to find the most compatible design for the alignment method in question.

The TP system accuracy is measured using the cross-correlation alignment method with alignment accuracy of sub-100 nm achieved. Following this, the systematic device placement accuracy was measured, with a lateral placement accuracy of ±380 nm demonstrated, and rotational accuracy of ±4.8 mrad. The achieved placement accuracies are currently the highest achieved alignment accuracy by TP to date, and include the first recorded measurements and analysis on the device rotational alignment using transfer printing. The high placement accuracy helps introduce the technique of transfer printing to the efficient integration of passive photonic components, with the following chapter discussing research into the vertical micro-assembly of fully fabricated and single-mode silicon micro-ring resonators.

Chapter 3

Transfer printing of ultra-thin membrane silicon photonic devices

3.1 Introduction

SOI has been demonstrated as a key photonic platform over the past decades with the continuous development of efficient passive and active optoelectronic components such as waveguides [90], modulators and detectors [91, 92]. Following this, the monolithic integration of these devices has helped pave the way for highly functional Si PICs, with monolithic Si optical transmitters and receivers already demonstrating long-distance and high-speed optical communications [93]. However, as the performance requirements of PICs increase, limitations appear in the monolithic fabrication approach. The manufacturing of SOI LS-PICs requires a considerably high number of processing steps, this increases both production time as well as the relative cost. Further to this, silicon currently does not offer the full suite of photonic components, as an efficient silicon light source still remains a difficult challenge [24]. The introduction of nanoscale TP can overcome such issues, enabling the efficient integration of fully fabricated passive and active photonic components across many material platforms all onto a single chip. Further to this, it adds the potential of 3D Si systems

without requiring multi-layered wafer bonding methods.

The following chapter describes the vertical micro-assembly of ultra-thin Si membrane devices by high alignment accuracy TP. The initial sections detail the development and fabrication of ultra-thin transferable Si membranes containing ultra-compact waveguide rib resonators. This is then followed by the integration of the membrane resonators to non-native passive SOI receiver substrates forming all-pass ring resonators. The calculation of the absolute placement accuracy of the method is achieved by measuring the varying lateral coupling offset across multiple assembled devices. To conclude, the research into producing 3D SOI devices by TP is demonstrated, with the production of a multi-layered silicon and silica interface DBR stack with reflectance in the visible spectrum.

3.2 Device design and fabrication

The production of single-mode waveguides within the SOI platform requires device architectures with sub-micron dimensions. This is due to the high refractive index contrast between the silicon and silica, pushing the passive structure geometries to sub-micron levels. The advantage of such small components is that it allows the manufacturing of high packing density chip-scale architectures, however it also puts significant pressure on the fabrication, with transmission losses scaling with the square of the roughness amplitude [94]. For all Si components in this thesis, all patterning is achieved by electron-beam lithography (EBL), helping reduce sidewall roughness for low propagation and bend losses whilst keeping high alignment across the multi-layered lithography stages. When considering scalability for mass manufacturing, deep-UV lithography (DUV) can be an alternative option helping provide the necessary low side-wall roughness.

The SOI wafers used throughout this thesis are produced by Soitec who develop the wafers by a Unibond process, providing a very accurate thickness of each core layer with low interface roughness. The stack is comprised of a 220 nm thick silicon core layer which is bonded above a 2 μm thick buried oxide on top of a Si wafer. The device fabrication is carried out by a collaborating group within the James Watt Nanofabrication Centre at the University of Glasgow.

3.2.1 SOI waveguides

The SOI receiver chips are composed of a standard SOI layer stack and contain fully etched Si ridge waveguides acting as bus ports, with the fabrication procedure detailed in figure 3.1. A hydrogen silsequioxane (HSQ) resist layer is deposited on top of the SOI wafer by spincoating. This is followed by EBL exposure to define the patterns into the HSQ layer, with a hard bake and development stage leaving only the HSQ pattern mask. The pattern is fully transferred into the silicon core layer by an ICP reactive-ion etch process, using an SF_6/C_4F_8 chemistry with an etch rate of 150 nm/min, with an etch-rate selectivity greater than three between the silicon core and HSQ mask layer [95]. No further post-processing is performed with the waveguide structures open to the environment with only a thin top cladding of HSQ, otherwise a silica buffer layer is deposited over the surface to protect from both environmental factors and physical damage.

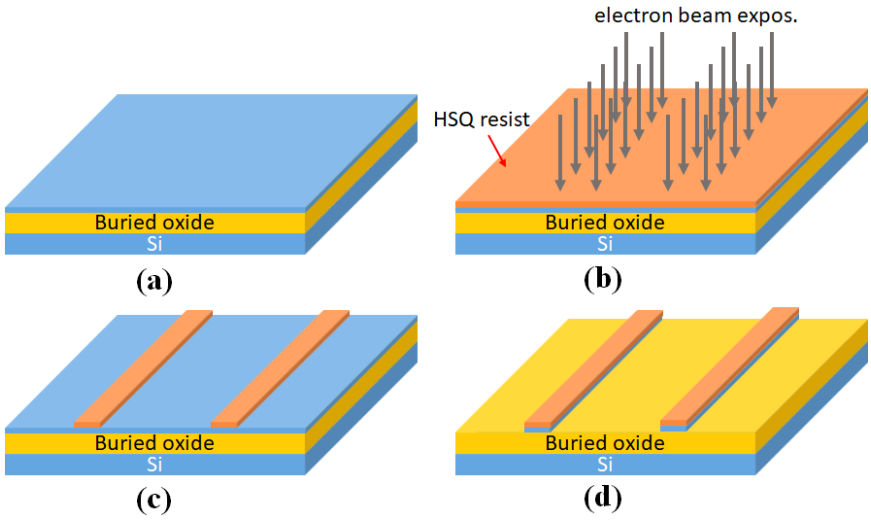

Figure 3.1: (a)-(d) Schematic of Si bus waveguide fabrication procedure; (e) SEM image of Si waveguide cross-section containing residual HSQ mask cladding.

Injection of light into the waveguides requires the use of tapered optical fibres, however typical fibre geometries reach several μm in diameter. When compared to the cross-sectional size of waveguides a large modal mismatch is formed which can translate to high coupling losses. To compensate for the size difference requires the use of mode couplers, gradually reducing the mode diameter before the light reaches the waveguide to minimise the modal size mismatch and reduce subsequent coupler loss. For this work, end-facet inverse tapered couplers are fabricated at both input/output regions using SU-8 photoresist prior to the full device cleave, illustrated in figure 3.2. Direct coupling between fibres and single mode silicon waveguides exhibit low geometric modal overlap, leading to coupling losses in the tens of dB range. The introduction of polymer inverse taper structures on the chip can improve TE mode coupling significantly, with losses as low as $\approx$1 dB per facet [96]. The polymer waveguide has dimensions in the micron range and a refractive index of $\approx$1.6, providing a much better modal overlap with the injection fibre mode. As shown in figure 3.2, a tapered silicon waveguide is embedded in the polymer structure. Due to the

high refractive index of the silicon, the optical mode will transfer between the polymer mode and the silicon waveguide as its dimensions exceed the cut-off point. The tapered geometry ensures adiabatic mode transformation, limiting coupling losses. .

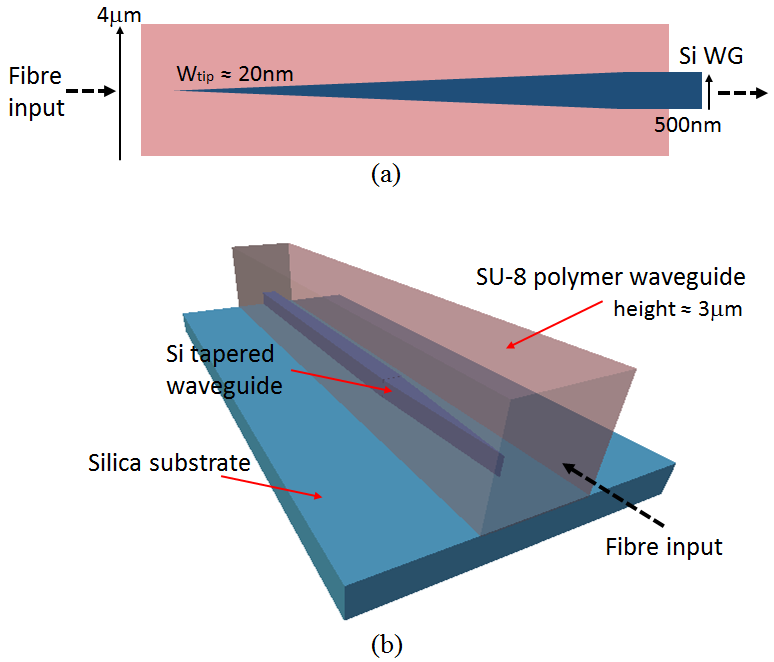

Figure 3.2: (a) Top-view schematic of an inverse taper, detailing the silicon waveguide width tapering from a tip width of ≈20 nm to its full width of 500 nm, and the constant polymer waveguide width of 4 μm. The fibre input couples to the facet positioned to the left of the taper structure. (b) 3D illustration of the inverse taper region fabricated at each facet of the chip. The silicon waveguide's full tapering length is 300 μm.

The above section describes the fabrication of silicon waveguide structures. These are implemented as the bus waveguides of the all-pass resonator devices produced throughout this work. The same fabrication techniques are utilised for the suspended silicon membrane devices.

3.2.2 Ultra-thin Si membranes

The TP method relies on the ability to detach small coupons of material from their native wafer and transfer them to a receiver substrate. TP in the SOI platform

requires the development of releasable Si material membranes, containing the fully-fabricated devices of interest which can be reliably detached and manipulated in a high yield manner. Fabrication of the releasable Si membranes implements past techniques for producing transfer printable LEDs [41], with a schematic illustration shown in figures 3.3 a-c.

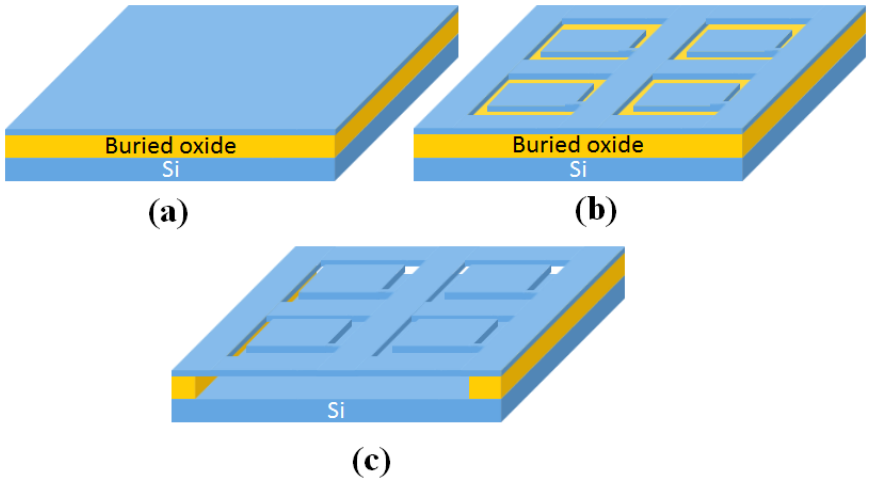

Figure 3.3: Schematic illustration of suspended membrane fabrication. (a) SOI wafer prior to any processing composed of silicon core layer of 220 nm thickness, a buried oxide layer of 2 μm thickness, and a silicon substrate. (b) Full ICP-RIE etch of trench surrounding membrane, leaving sole anchors to suspended the membrane structure. (c) HF vapour etch of buried oxide cladding suspending the membrane structure ready for release.

The initial stage is the production of a trench region surrounding the membrane attached by tapered anchored supports. A PMMA layer is deposited on top of the SOI wafer which is subsequently patterned by EBL. The trench and anchors are defined by a full ICP reactive-ion etch in order to open a via to the silica below, produced by the same recipe and process as described in section 3.2.1. Next is the suspension of the ultra-thin silicon membrane devices. Full suspension requires the removal of the buried oxide (BOX) layer which separates the silicon core layer and silicon substrate. A Hydroflouric (HF) acid etch, with its high silica-Si selectivity

provides the full removal of the silica cladding with minimal etch roughness introduced to the Si waveguiding layer.

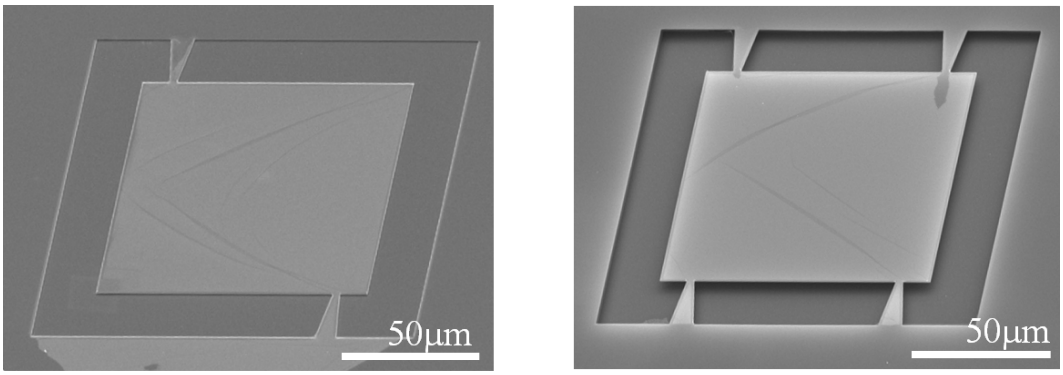

Figure 3.4: (a) SEM image of a suspended membrane fully collapsed and bonded to the Si substrate. (b) Successfully fabricated suspended silicon membrane attached by support anchors overhanging the substrate.

The thickness of the ultra-thin Si core layer results in highly flexible and delicate membrane structures when under-etched, therefore care has to be taking to avoid collapse when undergoing the fabrication. As a typical HF etch requires the immersion in liquid it can be an aggressive process, which would lower the overall device yield by membrane collapse onto the substrate surface, as shown in figure 3.4a. To improve the yield, a HF vapour release etch (VHF) is utilised. This is a technique commonly used for device suspension in micro electro mechanical systems (MEMs) [97]. As it is a dry etch, it takes advantage of being able to use a HF gas in it's pure chemical form (100 % concentration), such that a lateral etch rate of our 100x100 μm^2 membranes of ≈150 nm/min is achieved. The full under-etch is carried out in two runs with an overall etch time of ≈11 hours. An SEM of a finished suspended membrane is detailed in figure 3.4b. The VFH release is an isotropic etch process, therefore to fully under-etch whilst leaving suitable support regions for the membrane suspension requires a membrane coupon separation of more than double the

membrane length, with our wafer design utilising a membrane separation of 400 μm.

3.2.3 Si membrane device design

Prior to the fabrication steps, finite difference eigenmode (FDE) simulations are used as a means to optimise the Si membrane waveguide geometries for low-loss single-mode TE propagation. Variables included the waveguide width (w) and slab thickness (s) whilst keeping the overall waveguide height of 220 nm, detailed in figure 3.5.

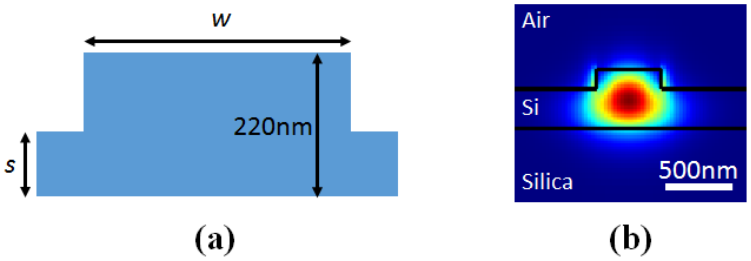

Figure 3.5: (a) Schematic cross-section of silicon waveguide detailing the width (w) and slab thickness (s). (b) Simulated TE_{00} mode profile for a silicon rib waveguide detailing the layer composition.

Simulations using Lumerical's FDE mode solver were implemented in order to measure the single-mode propagation within shallow-etched Si rib waveguide structures. The method calculates the spatial profile and frequency dependence of modes on a cross-sectional mesh of the waveguide, measuring the waveguide effective refractive index. Both the modal cut-off and multimode regimes are defined based upon the waveguide's material layers and dimensions. Further to this, by adding an additional bend loss to the waveguide, tolerances to the achievable waveguide ROC are calculated.

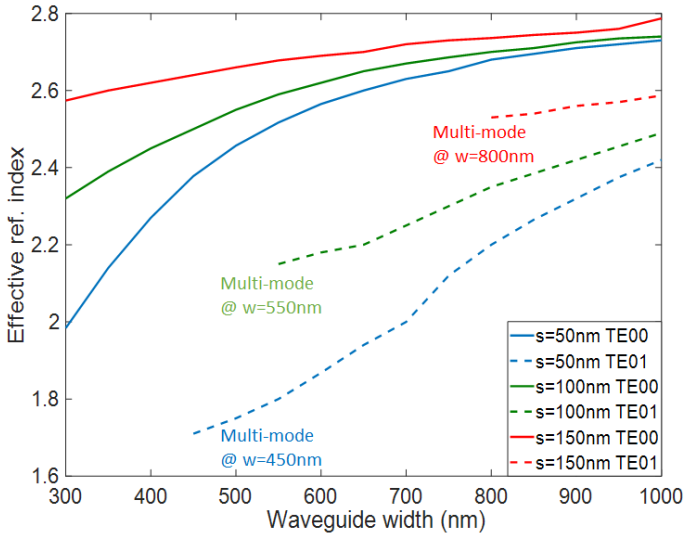

Figure 3.6: Plot of simulated mode effective refractive index for shallow-etched rib waveguides as a function of waveguide width (w) and slab height (s). The presence of a secondary mode solution (TE_{01}) defines the multi-mode condition of the waveguide, with the lack of a secondary mode indicating the conditions for single-mode propagation.

Figure 3.6 details the simulated effective index change when varying the waveguide geometry for the first and second order TE propagating modes. Multiple slab thickness of s=50, 100, and 150 nm are measured for an increasing waveguide width of 300 nm<w<1000 nm. Each of the three different slab heights enter multi-mode propagation at different waveguide widths, with the increased slab height producing single-mode propagation until w=800 nm. As the slab height decreases, the single-mode condition requires a decreased waveguide width.

Following this, simulations are carried out to determine the propagation loss of a waveguide with a slab height s=150 nm and full membrane height of 220 nm, shown in figure 3.6. The plot details that for decreasing waveguide width, the propagation loss will increase significantly which is directly related to mode cut-off to the surround slab region. A propagation loss of >1 dB/cm is desirable for producing resonator waveguides, with a limit to the waveguide width of w=450 nm. The final simulation

details the bend loss calculation for a ridge waveguide of parameters w=500 nm and s=150 nm and an overall membrane height of 220 nm. The tighter the curve, the more the mode profile shifts to the outer edge of the bend, interacting with the surrounding medium causing mode leakage and increased scattering loss [60]. The simulated results indicate that this issue arises for ring radii of <10 μm, with radii 15 μm and above demonstrating an average bend loss of ≈0.9 dB/cm. The ridge waveguide geometry chosen for the following work consists of a waveguide width of w=500 nm and slab height of s=150 nm, whilst ring radii of ROC = 15, 20, 25, and 30 μm are utilised in producing low loss and compact membrane ridge waveguide structures.

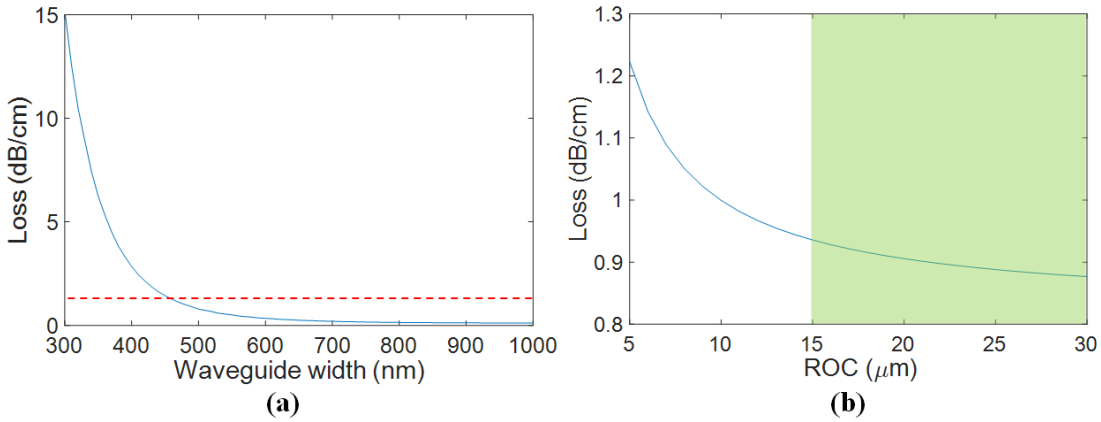

Figure 3.7: (a) Propagation loss measured as a function of width for a slab height of s=150 nm and full membrane height of 220 nm. The red dotted line highlights 1 dB/cm propagation loss limit. (b) Bend loss as a function of ROC for w=500 nm, s=150 nm and membrane height of 220 nm. The green shaded area highlights the ROC range used for the following experiments.

Si membrane device fabrication

This section details the fabrication procedure for the Si membrane devices. The production of the suspended Si membrane waveguides combines the techniques previously demonstrated for both fabrication techniques outlined in sections 3.2.1 and

3.2.2. Prior to fabrication of the surrounding trench, Si rib waveguides and a supporting frame are shallow-etched inside the membrane region using the standard lithography and RIE etching processes demonstrated before. The etch depth is calculated by removing the slab thickness from the membrane full height with a shallow-etch depth of 70 nm introduced. An illustration of the shallow-etched waveguide fabrication is shown in figure 3.8b.

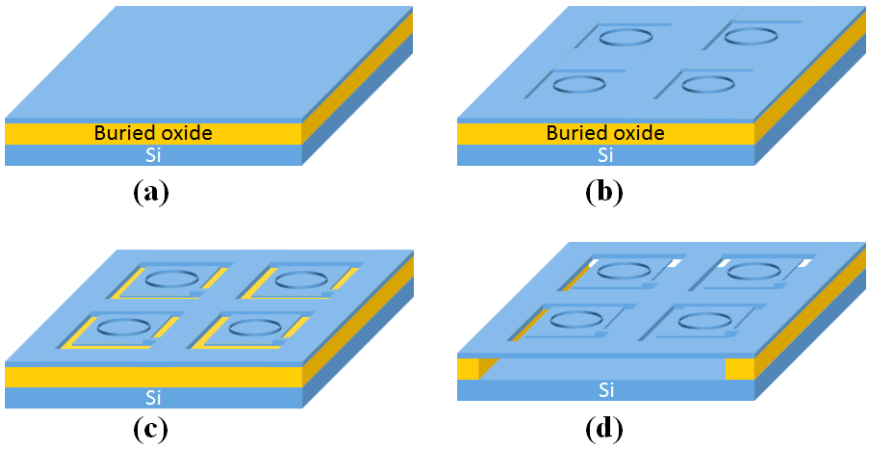

Figure 3.8: Schematic illustration of full membrane resonator fabrication protocol detailing the (a) SOI wafer prior to processing; (b) shallow-etch of membrane waveguide; (c) full Si etch of trench and support anchors; (d) membrane under-etch of buried oxide for device suspension.

After the shallow-etch, a trench is formed surrounding the complete structure by the full etch of the Si layer, leaving only the anchored supports holding the membrane to the remainder of the core layer. This is followed by the VHF under-etch to remove the buried oxide layer fully suspending and finishing the Si membrane device fabrication. The suspension steps are illustrated in figure 3.8c-d.

A top-view SEM image of a fully fabricated single membrane containing Si ring resonators is shown in figure 3.9 attached to the remaining Si core layer by two anchors situated at opposite ends of the structure. The support region at the full 220 nm Si core thickness surrounds the waveguide structure as a means to improve

on the membrane rigidity, detailed by the lighter regions of the membrane. Figure 3.9b is an SEM image of an array of Si membranes on a SOI wafer. Multiple arrays are fabricated on a single wafer with each containing different waveguide geometries enabling both highly compact and variable device integration.

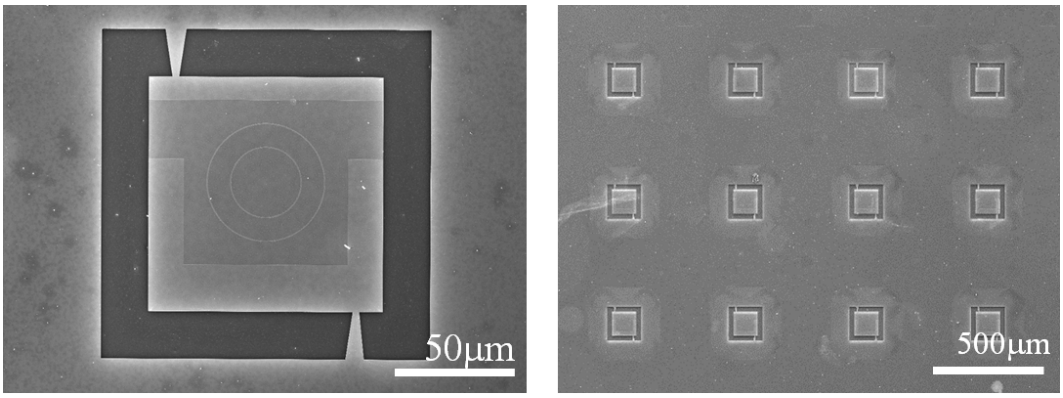

Figure 3.9: (a) SEM image of suspended membrane containing multiple shallow-etched ring resonator devices. (b) SEM image of a suspended membrane array.

3.3 Optical transmission measurement set-up

For the characterisation of the micro-assembled micro-ring resonators, the measurement set-up shown in figure 3.10 is utilised. Light from a tunable continuous wave (CW) laser, Agilent 81640A, with a wavelength range of 1510-1640 nm was coupled onto the Si chip via optical polarization control optics, isolator, and a tapered optical fibre. The light was captured from the output facet by an objective lens and focused onto the face of a photodetector and fed to an oscilloscope. An IR camera is used for fibre-to-facet active alignment for optimum light coupling on-chip.

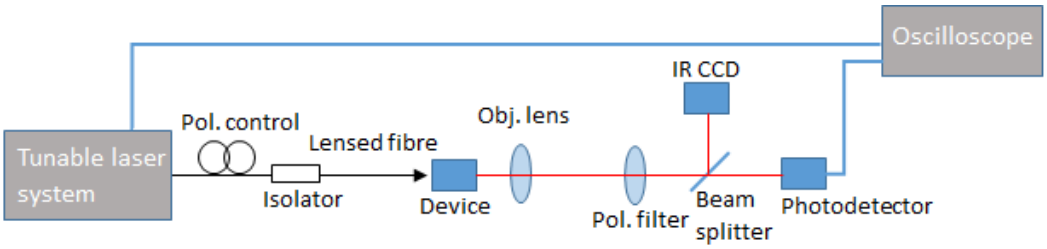

Figure 3.10: Schematic illustration of the experimental set-up for capturing the transmission spectra of the all-pass resonator devices.

The spectral transmission response of the device is measured by triggering sweeping the tunable laser across the desired wavelength range and recording the photodetector intensity signal as a function of time. The oscilloscope measurement is triggered by the laser source which is then swept at a constant rate, e.g. 20 nm s^{-1}. The captured temporal intensity trace can be converted to an intensity spectrum through the laser sweep speed and the oscilloscope sampling rate. For a sweep speed of 20 nm s^{-1} and an oscilloscope sampling rate of 20,000 Sa/s, the resultant measurement resolution is 1 pm. This provides an output measured intensity of the waveguide device as a function of the input laser wavelength.

3.4 Micro-assembly of SOI ring resonators

The absolute placement accuracy achievable by the high alignment TP method enables the micro-assembly of Si membrane micro-ring resonators with precise control over lateral coupling gap (x) between the bus waveguides and membrane micro-ring resonator cavities. A detailed description of the alignment procedure is given in chapter 2. Figure 3.11 shows a top-view SEM image of the finished vertically coupled all-pass micro-ring resonator device. It is composed of a straight Si bus waveguide fabricated on the SOI receiver substrate for the evanescent coupling/de-coupling of light into the resonator cavity. The Si ultra-thin membrane is bonded onto the re-

ceiver substrate by using the established TP method, and laterally aligned (x) for optimised coupling between each waveguiding layer. A higher magnification top-view image of the resonator, given in figure 3.11b, details the multi-waveguide coupling region with the controlled x lateral alignment. The displacement is measured between the centre of both waveguide structures with the device having a targeted lateral displacement of 400 nm. The vertical separation is determined by the residual HSQ layer which is y=100 nm. Figure 3.11c shows the gradual conformation of the silicon ultra-thin membrane around the bus waveguide. The flexibility of the membrane structure enables a strong bond between the SOI receiver substrate and the membrane, enabling the vertical assembly of structures without any mechanical supports or use of adhesion layers.

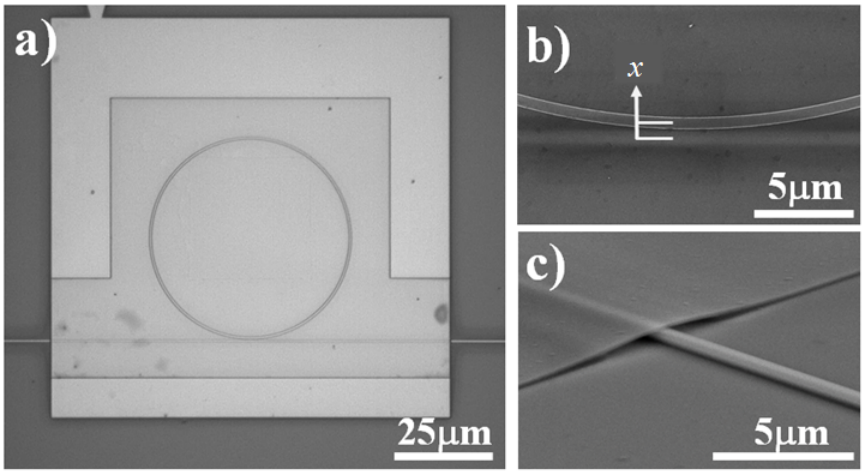

Figure 3.11: (a) SEM image of membrane resonator bonded to a SOI bus waveguide. (b) Magnified SEM image of the all-pass resonators vertical coupler region with a controlled lateral alignment offset x; (c) SEM image of the membrane conforming to underlying bus waveguide. The membrane thickness is 150 nm.

A measurement of the deformation of the membrane waveguide as it conforms over the receiver is calculated, including the calculated ROC. This allows the simulation of any additional vertical bend losses the device may inherit from the receiver

not being planar. For this calculation we assume a symmetrical s-bend cross-section of the curved membrane, as demonstrated in figure 3.12a, and using the equations:

$$R = \frac{D^2 + C^2}{2D}, \tag{3.1}$$

$$ROC = R - D, \tag{3.2}$$

where R is the radius of the full circle of the imaginary circle completing the curve with C and D being the length and height of the region of interest, respectively. The small aspect ratio of the bus waveguide height (320 nm) which includes the 220 nm Si waveguide and 100 nm HSQ capping layer compared to the lateral distance between both contact points of ≈5 μm gives a calculated ROC of ≈20 μm. This is achieved assuming a symmetrical s-bend deformation of the membrane with waveguide curvature in both upward and downward directions.

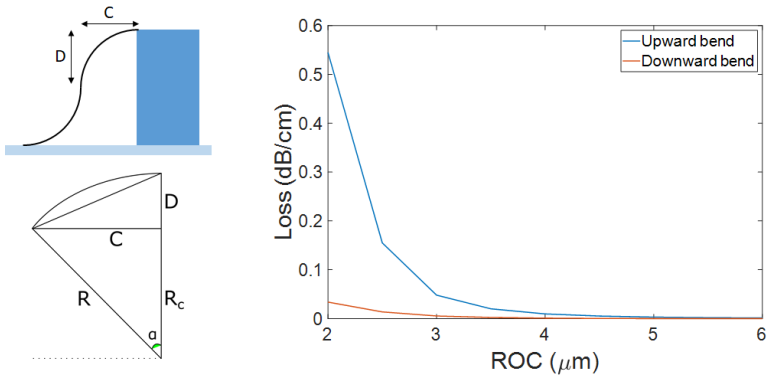

(a) **(b)**

Figure 3.12: (a) Schematic illustration of the membrane deformation as it conforms to the underlying waveguide structure. (b) Simulated plot of ROC in vertical direction as a function of loss for both upward and downward curvatures.

A bend loss for both upward and downward bend orientations was calculated in the range of 10^{-4} dB/cm for ROC greater than 5 μm, the low-loss comes from the

high refractive index contrast experienced between the Si and air/silica media. The relationship between ROC and loss is shown in figure 3.12b. As such, the added loss through waveguide deformation is negligible when compared to the transmission losses of the resonator structure and therefore will not detract from the overall performance of the membrane micro-ring resonator.

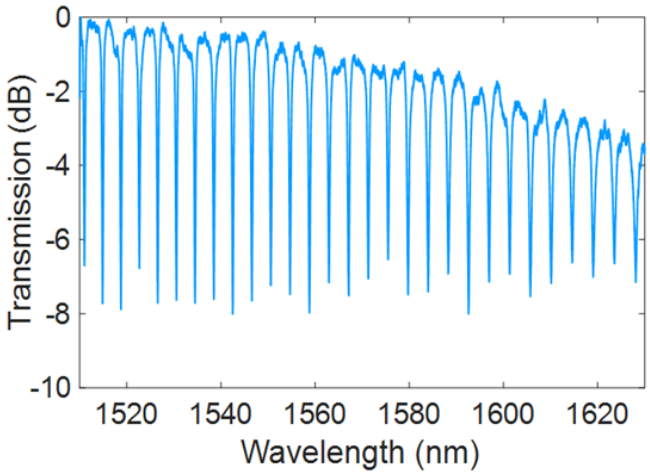

Figure 3.13: Measured transmission spectrum of the vertically coupled single-mode Si ring resonator produced by transfer printing.

The normalised transmission resonance spectrum of the assembled 25 μm-radius all-pass ring resonator is shown in figure 3.13, for a wavelength range of 1510-1630 nm. The resonator FSR is measured from the spectrum as ≈4 nm. By using equation 1.15, with a simulated group refractive index n_g= 3.66 a FSR of 4.2 nm at λ= 1550 nm is calculated, showing a clear match between the theoretical and experimental values. Following this, each individual resonance within the spectrum is theoretically fitted using a least-squares fit of the transmission intensity transmission function, equation 1.13. The cross-coupling coefficient (r) and single-pass amplitude transmission (a) during the fit are left as free parameters, with the best fit values used to calculate the device loaded Q-factor, using equation 1.20. The experimental average loaded Q-

factor value is measured as Q≈2,500, with similar values achieved when calculating directly from the resonance FWHM values, equation 1.18. An individually fitted resonance dip is shown in figure 3.14.

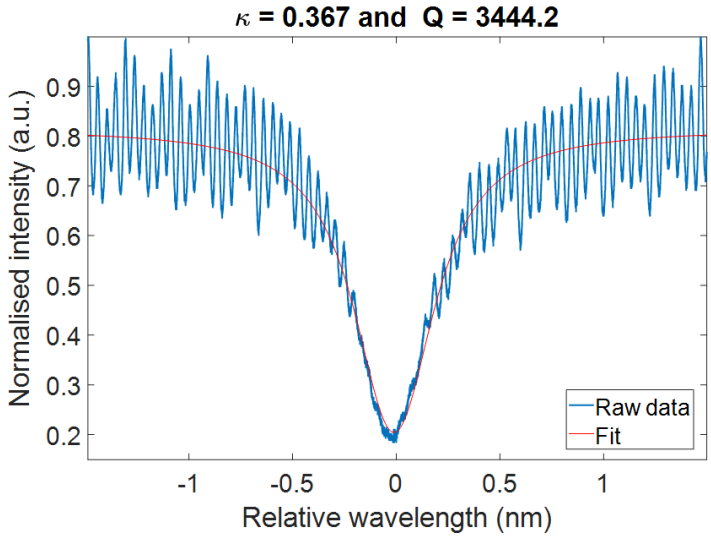

Figure 3.14: Theoretical fitting of a single resonance from the ring resonator normalised transmission spectra, with measured cross-coupling coefficient and Q-factor defined.

A state-of-the-art monolithically fabricated silicon ring resonator of similar geometry to the printed devices produces a loaded Q-factor for critical coupling at the value of 57,000 [98], an order of magnitude greater than our measured values. The reduction in quality when compared with similar monolithic Si devices can attribute to an increase in scattering losses. This effect was due to the silica undercladding of the membrane devices not being fully removed during the HF vapour etch, leading to a thin nonuniform silica surface on the membrane underside reducing the overall bond quality between the membrane and receiving substrate. By enhancing the contrast of the top-view image as well as by flipping a membrane to image the underside directly the roughness is demonstrated, figure 3.15. The roughness stops half way into the membrane under-etch with the same amount on the supporting silicon

region, shown in figure 3.15b. This is due to the first of two required VHF etch steps only partially removing the silica. By optimising the VHF etch process and moving to a single etch procedure, future fabrication processes have more efficiently removed the silica underneath.

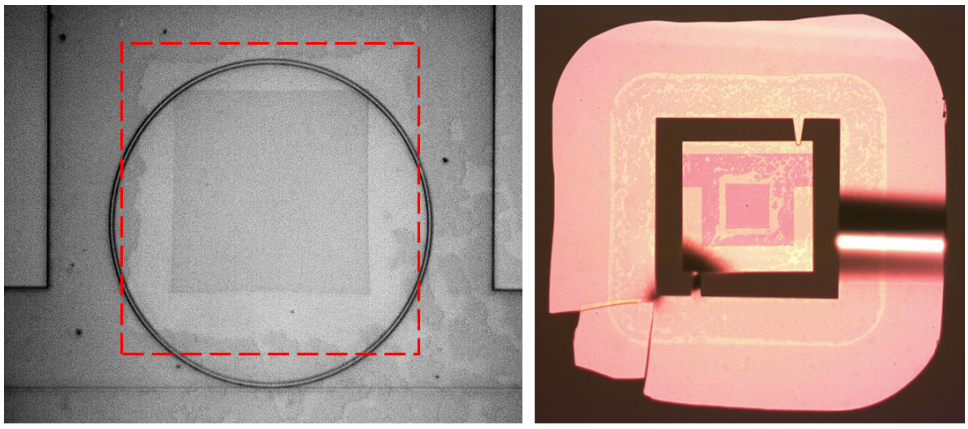

(a) **(b)**

Figure 3.15: (a) Top-view micrograph of the assembled all-pass resonator with underside roughness highlighted by a red dotted region. (b) Optical micrograph of the membrane underside showing the silica roughness.

3.5 Nanoscale placement accuracy

The positional accuracy of our TP procedure is measured by the micro-assembly of the membrane ring resonator structures with control over the lateral alignment between the printed membrane waveguide and underlying Si bus waveguide. Variation of the lateral displacement results in a change in the overall coupling coefficient and loaded Q-factor of the final assembled Si ring resonator. For the highest accuracy measurement of x we use high magnification top-view SEM images of the coupler region. The SEM pixel resolution is in the range of ± 10 nm therefore below the expected resolution of the alignment procedure.

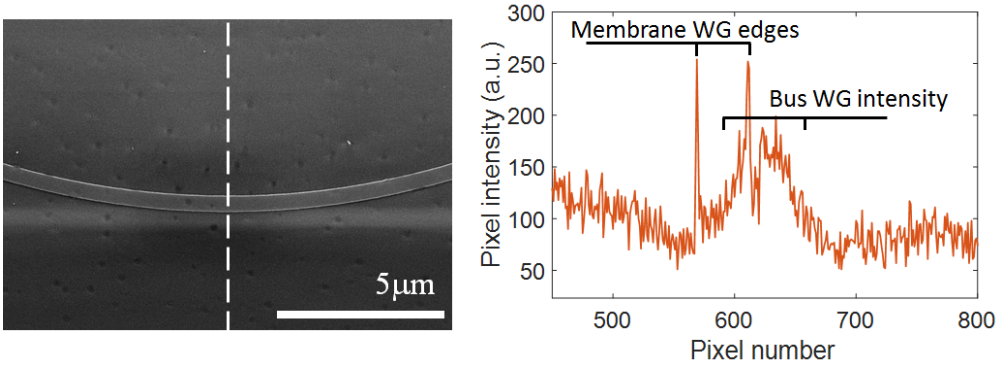

Figure 3.16: (a) SEM image and (b) associated line sections of the coupler region of a micro-assembled ring resonator. The edges of the membrane waveguide produce high intensity spikes, whilst the underlying waveguide produces a slowly varying increase in the overall intensity.

Due to the ultra-thin membrane, electrons can reach the underlying waveguide allowing the imaging of both the coupler sections of the membrane and receiver waveguides, as illustrated by the SEM image in figure 3.16a. Lateral positioning of the membrane waveguide with respect to the FOV is measured by taking a line profile across the image at the lowest point of the curved waveguide, figure 3.16a. The high scattering of electrons during the imaging enables the waveguide edge features to be easily resolved, with the waveguide centre taken as the average spatial position between the two edge points, as shown in figure 3.16b. However, the lack of resolution on the underlying bus waveguide edge profile inhibits the ability to accurately measure it's lateral positional information.

The difference in intensity profile of the bus waveguide is a factor of the electron scattering through the membrane material during the imaging process. To minimise the effects of noise in the image, the bus waveguide envelope was calculated as an average of a number of line sections at either side of the coupling point. In order to ensure that the scattering through the membrane has a negligible effect on the measured central position, an image was taken at the point where the bus waveguide

emerges from the membrane such that the waveguide edge positions can be measured with greater accuracy, figure 3.17a. The central positions are measured using the edge detection method in the exposed region and by calculating the central position of the envelope in the membrane covered region, with both methods producing a result with the centre point within the pixel resolution of the image. This comparison is shown in figure 3.17b.

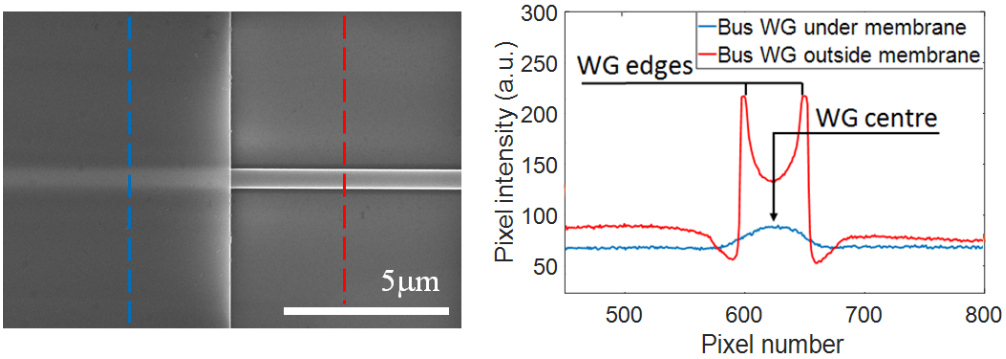

Figure 3.17: (a) SEM image and (b) associated line sections of the underlying bus waveguide at the membrane edge. The dotted lines represent the recorded sections used to produce the intensity line profiles.

Finally, by overlapping the two waveguide central points and taking the difference between the measured positions of the membrane and bus waveguides, x can be calculated. This plot is demonstrated in figure 3.18. The final measured lateral offsets are provided in table 3.1.

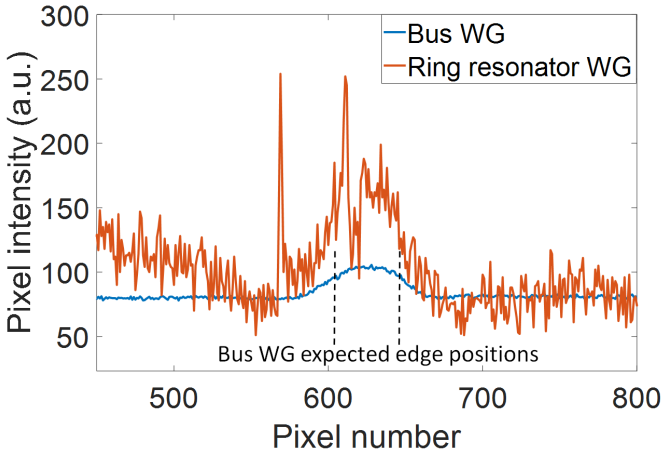

Figure 3.18: Plot of the overlapped associated line sections of the coupler region of the transfer printed membrane ring resonator device.

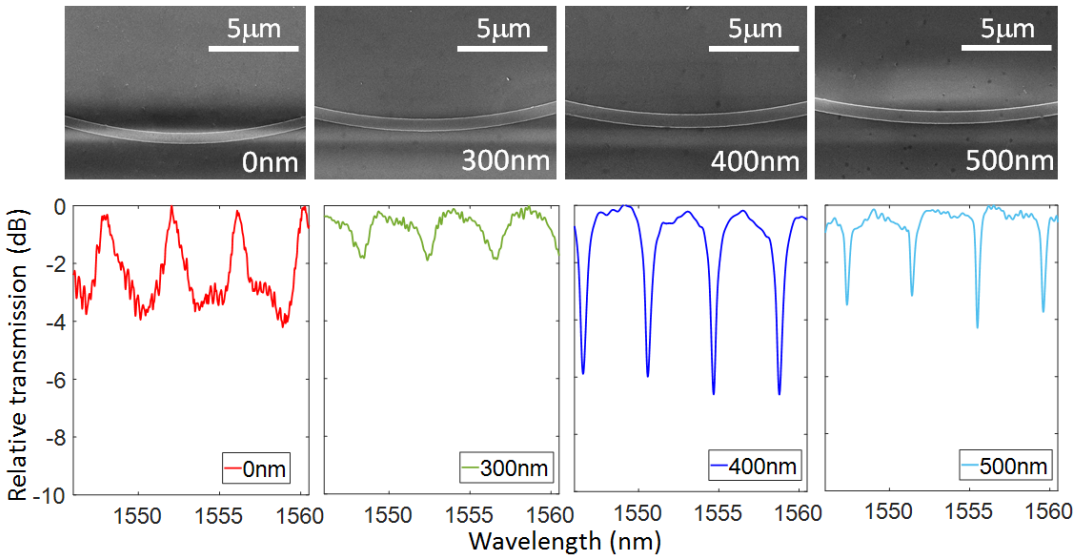

Figure 3.19: SEM images showing the waveguide lateral offset variation across multiple devices, including target x values. Included are the corresponding transmission spectra of each resonator device sweeping a wavelength range of λ= 1540 nm to 1560 nm.

Table 3.1: Comparison of micro-assembled SOI ring resonators

Expected x (nm)	Meas. x (nm)	Coupling coeff.	Q-factor
0	55	-	-
300	330	75 %	2000
400	530	50 %	2500
500	710	34 %	4100
Average error ± Std dev	100±70 nm		

Figure 3.19 shows top-view SEM images of the coupler region for the four micro-assembled devices as well as their respective optical transmission spectra over a 20 nm wavelength range centred at λ=1550 nm. The multiple top-view images of the coupler regions demonstrate the variation in the lateral offset of the membrane micro-resonators. The lateral offset x of each device are 0 nm, 300 nm, 400 nm, 500 nm with a fixed vertical coupling gap of ≈100 nm, applied by the use of an intermediate HSQ spacer layer as specified earlier in the chapter. By using the SEM image intensity profile method, an average positional alignment offset error over all devices is calculated at 100±70 nm, with each offset provided in table 3.1. The first three devices exhibit a placement accuracy better than 150 nm. Misalignments can be attributed to relative motion between the stamp and membrane devices during the printing process. The increased lateral waveguide offset is more evident in the device with a target separation of 500 nm with an absolute placement accuracy of 210 nm, however this exhibited accuracy is still better than the measured accuracies of current state-of-the-art TP methods. The measured transmission spectra for each device details the variation on the optical coupling as a function of the lateral offset between the membrane ring and bus waveguide. As x is increased resulting in a large coupling gap and therefore reduced coupling coefficient, the resonance linewidth exhibits under-coupling with a narrowed linewidth and decreased extinction. For the

case of the lateral offset x=0 nm, the resonance does not represent a well defined ring resonator. As the lateral alignment reaches x=0 nm with a HSQ spacer layer of ≈100 nm, the coupler region operates within a multimode regime producing complex coupling and loss behaviour as a function of the wavelength. The transition to a device layout exhibiting evanescent coupling between the waveguide structures is reached for lateral offsets greater than 200 nm, as shown by the corresponding single-mode resonances in the larger lateral alignment devices.

The theoretical fitting in order to obtain the loaded Q-factors is implemented for the devices exhibiting a lateral placement offset of $x \geq 300$ nm, with each devices corresponding Q-factor and coupling coefficient shown in table 3.1. In accordance with the reduction in linewidth for increasing lateral offset, an increase in the Q-factor alongside a reduction in the coupling coefficient is demonstrated.

3.6 3D assembly of Si membrane devices

Using the standard monolithic integration for Si photonic systems, the manufacturing of 3D architectures requires a large number of fabrication steps, which can be costly and time consuming with each added layer only increasing the fabrication complexity. As such, the introduction of TP, with it's ability to vertically assemble individual components in 3D architectures across many different material platforms can benefit the production of 3D PIC systems.

In this section we use TP to vertically assemble a selection of multi-layered ultra-thin membranes in a single stack without the use of intermediate bonding layers, with the success of the technique demonstrating the possible production of 3D device geometries.

3.6.1 Si multi-layered stack

There has been limited implementation of 3D stack assembly using TP. However, the capability which TP provides for the formation of 3D structures has been shown by past demonstrators of Si platelet stacking of multiple different platelet geometries, ranging from microns to sub-micron thickness [4].

The initial multi-layered structure we produce by TP is composed of five integrated Si membranes. The membranes have no patterned structures such that they are blank, and are made up of an ultra-thin 220 nm thickness Si layer. The aligned stack structure demonstrates the high rotational and translational control of the multi-layer TP method as well as great control of the bonding process. The micro-assembly is achieved on a Si receiver substrate with the direct bonding of each layer without the requirement of any additional adhesion promoting layers. An SEM of the fully assembled 3D stack is shown in figure 3.20. The TP protocol utilised is competitive adhesion using a flat PDMS stamp, relying fully on the direct adhesive-free layer bonding strengths.

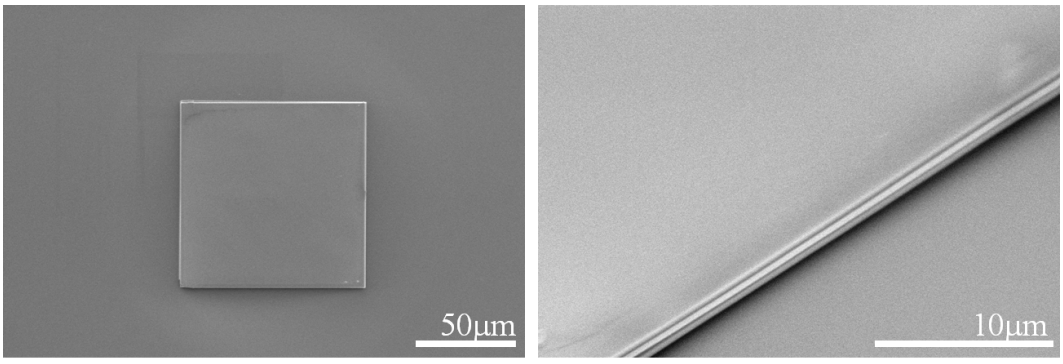

Figure 3.20: (a) Top-view SEM image of a multi-layered Si membrane stack utilising direct bonding of each layer; (b) Angled SEM image of the stack sidewall detailing the multiple layer structure.

3.6.2 Si and silica multi-layered DBR stack

Distributed Bragg reflectors (DBR) are multi-layered structures made up of an alternating arrangement of two or more materials producing a periodic variation in the structure's refractive index [99]. Each layer boundary - when satisfying the Bragg condition - will reflect light at wavelengths four times the optical path length with the combination of multiple layers producing a high quality reflector through constructive interference. The implementation of DBR structures can be used for photonic components such as DBR lasers [100] and resonant wavelength cavity micro-LEDs [101]. The DBR membrane structures consist of five-layer stacks of membranes. Each membrane contains two material interfaces, composed of a 220 nm thick silicon core layer followed by a deposited silica layer, with the geometry illustrated in figure 3.21.

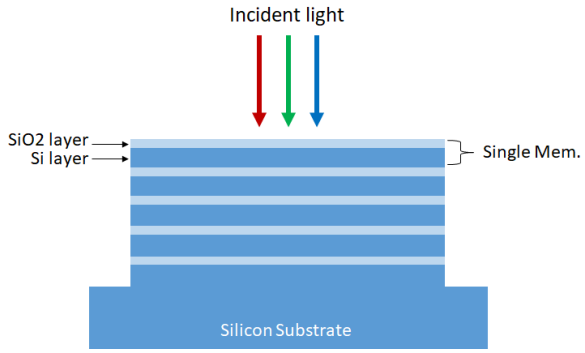

Figure 3.21: Schematic illustration of the Si/SiO_2 vertically assembled multi-layer stack structure.

The suspended Si membrane fabrication follows the procedure outlined section 3.2.2. The silica layer is added by plasma-enhanced chemical vapour deposition (PECVD) growth, with the deposition achieved after membrane suspension on the native substrate. Similar to the initial Si stack in section 3.6.1, the individual membrane assembly utilises no adhesion promoting layers. SEM images of a vertically

assembled membrane stack from both top and angled views are shown in figure 3.22. The device previewed has a silica interlayer thickness of 10 nm. The 10 nm thick silica layer was deposited as a test layer, making sure that the Si membranes would not collapse under the added weight and strain.

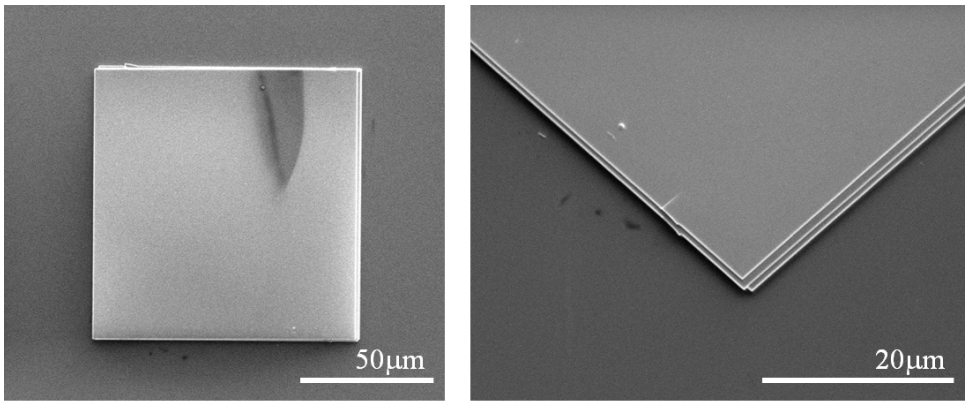

Figure 3.22: (a) Top-view SEM image of alternating Si/SiO_2 membrane stack assembled by TP. Dark region in top right portion of membrane is contaminant left from solvent cleaning. (b) Angled SEM image of the 3D membrane stacks sidewall.

Simulations were carried out using the Lumerical FDTD software package to find a combination of Si and silica which would produce a DBR with high reflectance within the visible wavelength range. An interlayer combination of Si (220 nm) and silica (100 nm) alternating layers was proposed, estimating a peak reflectance achieved for regions of the visible band for five bilayers, figure 3.23. It depicts a reflection band centred at ≈450 nm with a second wide-band over the wavelength range ≈550-680 nm.

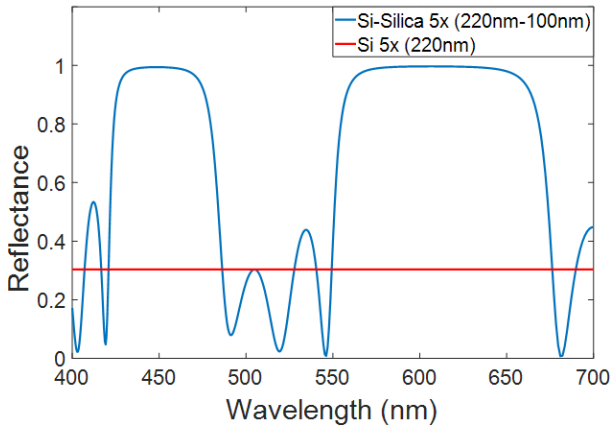

Figure 3.23: Simulated DBR reflection plot for 5x membrane layers of alternating silicon (220 nm) and silica (100 nm), compared against Si only stack structure.

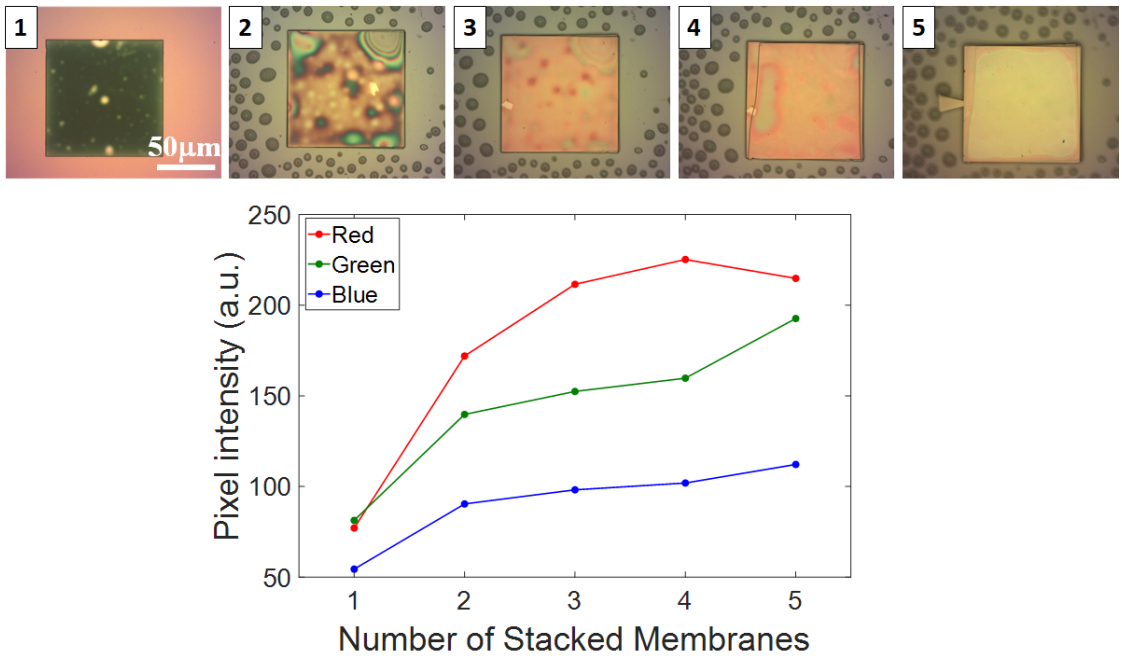

Figure 3.24: Top-view optical micrographs of Si/SiO_2 stack captured between each membrane print: *Left to right*: one to five membranes, tracking the change in membrane colour as each layer is added. Plot containing membrane intensity for each stage of the stack assembly, with the pixel intensity corresponding to the RGB pixel intensity of the images averaged over the full membrane areas.

Figure 3.24 details the evolution of the TP Si-silica membrane stack through top-view optical images. After each individual membrane is added, an image was captured to record the variation in the visible reflectance. The images depicts a

variation in the overall membrane reflected colour. This is further shown within the plot, which tracks the varying pixel red, green, and blue (RGB) intensity of the membranes across the number of stacked membranes. The measured RGB intensity is averaged over the full membrane area. The introduction of IPA during membrane printing was used to improve the bond quality through capillary actions, with the IPA droplets appearing on the substrate.

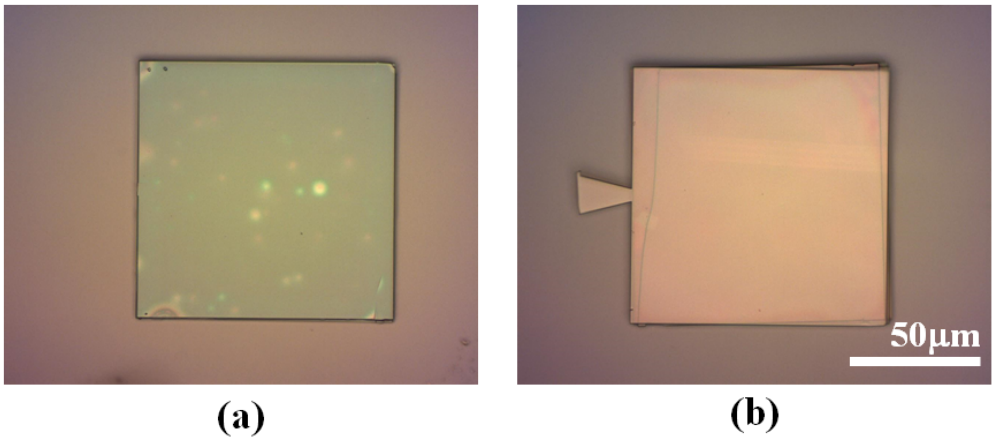

Figure 3.25: Top-view optical micrographs of (a) silicon 5x membrane stack (220 nm per membrane); (b) silicon-silica 5x membrane stack (220 nm silicon and 100 nm silica per membrane).

A direct comparison between the two obtained multi-layered membrane stacks, each containing five membranes, are detailed in figure 3.25. The block Si membrane stack with no additional interlayer silica is shown in figure 3.25a, and the Si membrane stack containing the 100 nm deposited layer is shown in figure 3.25b. The two stacked structures are capture within the same image as to produce identical imaging conditions. A distinction in the reflectance is exhibited between the two structures, with further image processing analysis characterising the reflectance comparisons for each stack structure. Each membrane image is separated into their RGB components, allowing characterisation of the reflectance change captured by

the microscope camera. A bar chart plots the RGB intensity distribution between each membrane stack, with the pixel intensity averaged over the full membrane area, is provided in figure 3.26.

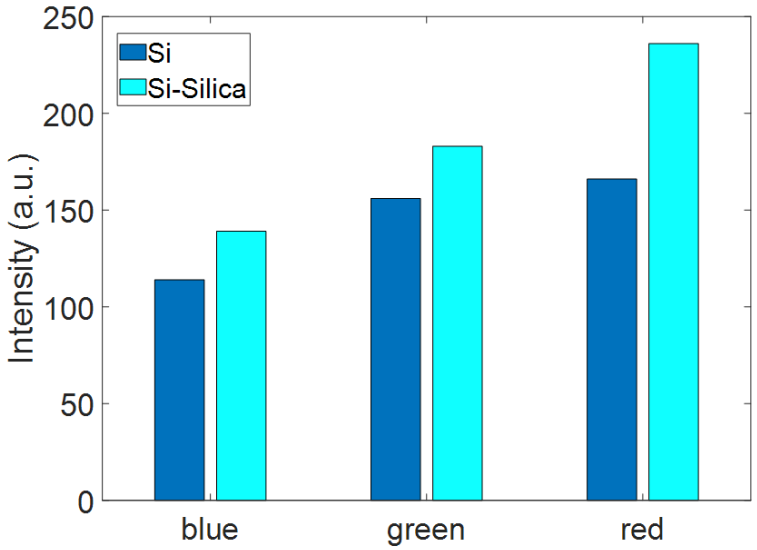

Figure 3.26: Barcjart detailing the variation in the RGB pixel intensity between the silicon only and silicon-silica stack structures, with the pixel intensity averaged over the full membrane area.

The output is compared against the simulated expected reflectance in figure 3.23, which predicts a large reflectance within the red wavelength region. The values from figure 3.26 shows similarities between the experimental and expected reflectance behaviour of the DBR stack, with the red wavelength component showing an increased pixel intensity for the silicon-silica stack corresponding to a higher reflectance in these wavelength regions. The reduced change in the green and blue wavelength components are also expected from the simulations, with a smaller reflectance band in the blue region whilst a slight reflectance overlap is predicted in the green wavelength region.

Overall, a 3D DBR stack structure is produced detailing a measurable change

in the device reflectance within the visible spectrum, with similarities in it's reflectance comparing to target reflectance simulations. The experiments demonstrate the transfer printing of multi-layered devices by the stacking of fully fabricated suspended membranes, with the technique possibly being a route towards producing future 3D photonic components.

3.7 Conclusions

In this chapter, the design and fabrication of ultra-thin silicon membranes was introduced. The design and modelling of single-mode silicon waveguide structures is contained. As well as the full process flow into the production of the receiver platforms SOI bus waveguides, and the techniques required for the production of ultra-thin suspended silicon membrane devices ready for transfer printing.

The chapter contains a description of the techniques used for the micro-assembly of vertically coupled all-pass SOI ring resonators by high accuracy transfer printing. With the method achieving single-mode vertically coupled all-pass ring resonators with Q-factors reaching ≈4,000. The nanoscale placement accuracy using our high precision TP method is measured by varying the lateral alignment offset between the membrane ring resonators and receiving bus waveguide, with an average placement accuracy as low as 100±70 nm calculated. The high placement accuracies achieved clearly show the ability of TP as a future technology for the future integration of passive photonic components across multiple non-native platforms.

As well as this, the three-dimensional micro-assembly of silicon membranes by TP is shown with controlled rotational and lateral alignment. The addition of a silica deposited interlayer produces multi-layered Si/SiO_2 DBR stacks with the demonstration of selective reflectivity. This demonstrates the possibility of using transfer

printing for the production of 3D photonic devices.

Chapter 4

Hybrid integration of WGM resonators by transfer printing

4.1 Introduction

WGM resonators are widely employed components in photonic systems. The resonant enhancement of light-matter interactions and environmental sensitivity enables applications ranging from nonlinear processes such as second-harmonic generation (SHG) and four-wave mixing [102, 65], to nano-scale high speed sensors [103], and the production of active photonic components such as micro-disk lasers [104]. Two material platforms utilised in producing chip-scale WGM resonators are of particular interest, these are silicon and aluminium gallium arsenide (AlGaAs). Silicon is compatible with CMOS manufacturing used by the electronics industry and has a high $\chi^{(3)}$ material nonlinearity. AlGaAs also has a large $\chi^{(3)}$ coefficient, and unlike Si, also exhibits a large $\chi^{(2)}$ nonlinearity. Further to this, both materials are transparent in the NIR telecommunication band, such that they can be used for significant technology developments within this wavelength range.

The production of efficient nonlinear components in monolithically fabricated SOI has several fundamental material issues, these are its lack of $\chi^{(2)}$ nonlinearity

combined with its two-photon absorption (TPA) and free-carrier absorption (FCA) at the 1550 nm wavelength. In order to produce high performance nonlinear components within the SOI platform we must heterogeneously integrate with more suitable material platforms, such as AlGaAs. This chapter focuses on the hybrid integration of AlGaAs-on-SOI micro-disk resonator devices using the high alignment accuracy transfer print method as a means to produce efficient nonlinear photonic components within the SOI platform. We first detail the integration of fully fabricated AlGaAs micro-disks of varying diameters with SOI waveguides producing high-quality factor hybrid resonator devices. Design and fabrication methods of the free-standing III-V micro-disk structures are explained, alongside in-depth characterisation of the TP micro-disk placement accuracy and finished hybrid resonator optical performance. Hybrid micro-disk resonators are micro-assembled onto SOI waveguides with both lateral and vertical coupling gap control. The vertical and lateral coupling mechanism are utilised for controllable selective excitation of different mode families within the disk resonators showing variation in coupling coefficient and Q-factor as a function of lateral offset between micro-disk and underlying bus waveguide. Further to this, we demonstrate the nonlinear capabilities of the hybrid resonators by achieving four-wave mixing (FWM) at low optical on-chip power, with efficiencies rivalling the state-of-the-art monolithically integrated resonator devices.

4.2 AlGaAs-on-SOI micro-disk resonators

4.2.1 Design

The AlGaAs micro-disk resonators are fabricated from an AlGaAs/GaAs material stack wafer composed of a GaAs substrate and two Al_xGa_{1-x}As thin layers, shown in figure 4.1a. The material composition of both AlGaAs layers have a vital role in the

disk fabrication, as furthered explained in section 4.2.2, with the AlGaAs micro-disk structures fabricated from the $Al_{0.3}Ga_{0.7}$As core layer. For the experiments, multiple diameter disks were fabricated from 5 to 20 μm with the disk height provided by the core thickness.

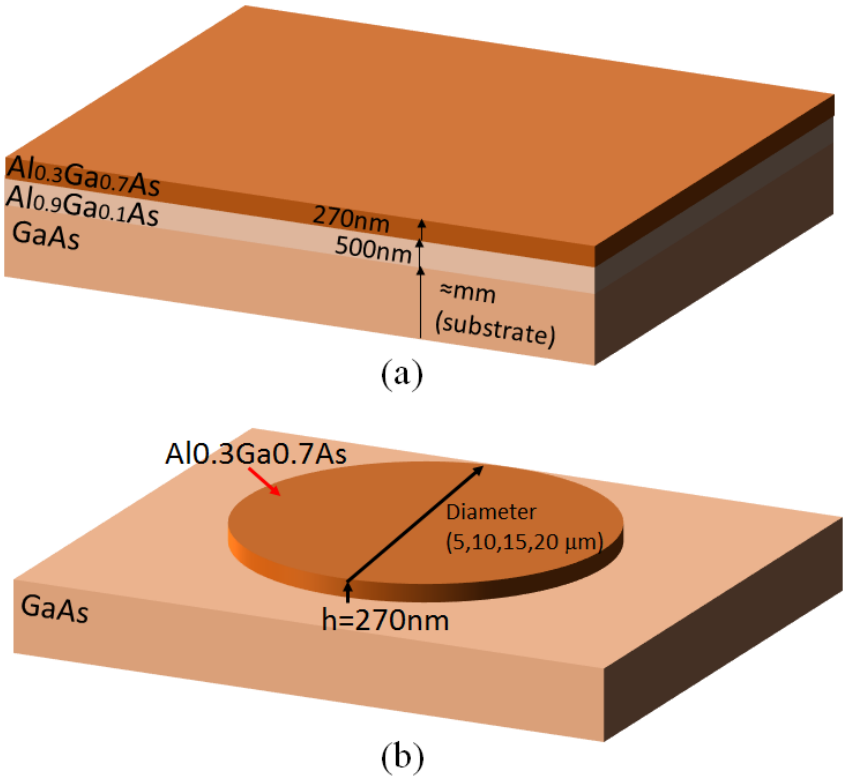

Figure 4.1: Schematic of (a) AlGaAs-on-GaAs wafer, detailing each layer thickness. (b) Post-fabrication micro-disk composed of the $Al_{0.3}Ga_{0.7}$As core layer on top of the GaAs substrate.

In micro-resonators, the tight control over mode coupling plays an important role in the production of high quality resonators, with nanoscale deviations in the coupling gap as well as mode cross-talk vital to overall device performance. With respect to this, vertical confinement of the micro-disk resonator modes is required to suppress complex resonant conditions within the micro-disk structure, limiting the resonant cavity to a single vertical mode and polarisation. This was accomplished

by restricting the disk cavity thickness.

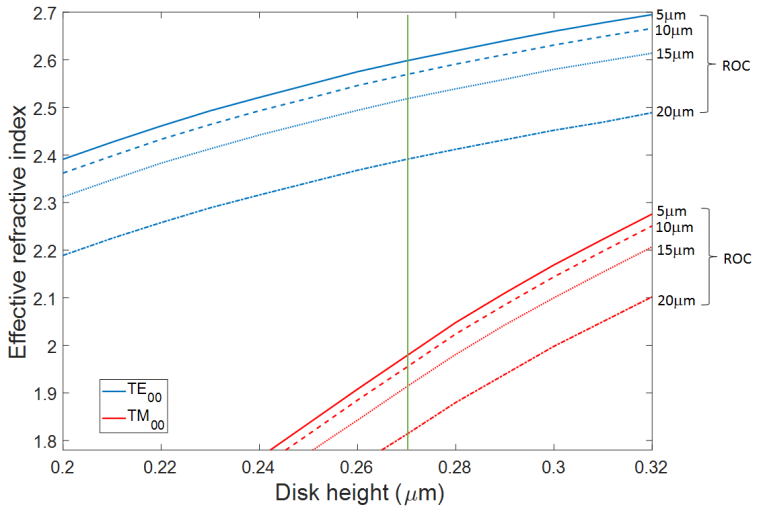

Figure 4.2: Simulated effective index as a function of the disk height for the fundamental TE and TM modes, with a height of 270 nm producing single-mode and low loss TE propagation (green line). Simulation is carried out with a variation of radii with ROC of 5,10,15,20 μm.

Figure 4.2 details a simulation of the effective refractive index change when the disk height is varied for both the TE and TM fundamental modes within the disk cavity. The simulation is carried out by a Lumerical FDE mode solver, as previously used within section 3.2.3, calculating the mode confinement within a cross-section of the AlGaAs micro-disk. This is simulated for a micro-disk structure with varying radii, with ROC=5,10,15,20 μm simulated. The increase in ROC due to the reduction in mode confinement reduces the overall effective refractive index. As the micro-disk height is reduced the TM propagation mode has an increased loss, as the modal cut-off is reached. The disk height of h=270 nm used throughout this work is highlighted by a green line within the plot. Further to this, the optimised disk has negligible loss across the full span of higher order WGMs.

4.2.2 Fabrication

The micro-disks are fabricated from an AlGaAs epitaxially grown material stack on top of a GaAs substrate. Control over the aluminium content of the $Al_xGa_{1-x}As$ (x is the composition percentage i.e. x=0.3=30 %) enables the production of highly selective sacrificial layers which can be used to isolate AlGaAs structures from the GaAs substrate. For this work an $Al_{0.3}Ga_{0.7}As$ layer of 270 nm thickness was grown on a high aluminium content $Al_{0.9}Ga_{0.1}As$ sacrificial layer of 0.5 μm, as shown by the schematic in figure 4.3. Micro-disk structures of 270 nm thickness, with diameters ranging from 3 μm to 20 μm, were patterned using EBL into a deposited HSQ resist. A full etch of the $Al_{0.3}Ga_{0.7}As$ is achieved using a $SiCl_4/Ar/N_2$ RIE process. Following this, a buffered 10:1 HF acid etch selectively removes the high aluminium content $Al_{0.9}Ga_{0.1}As$, which releases and distributes the free standing $Al_{0.3}Ga_{0.7}As$ structures randomly across the GaAs substrate. After an IPA cleaning stage, the AlGaAs micro-disks are ready to be transfer printed.

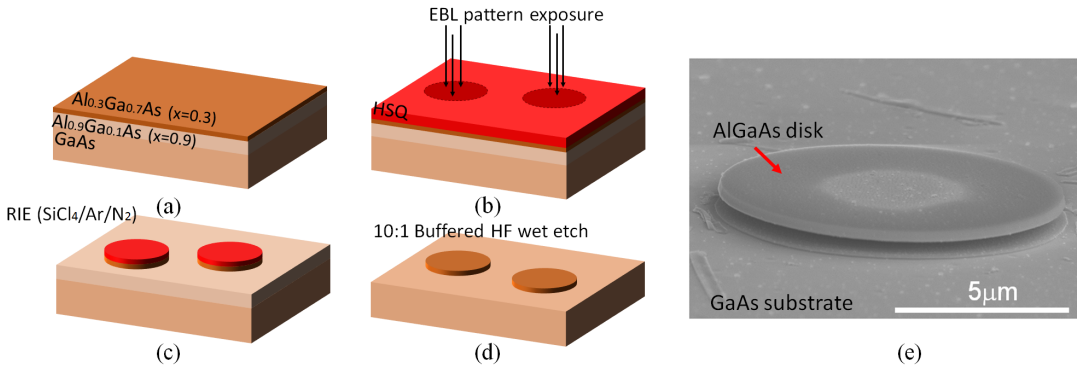

Figure 4.3: Schematic illustration of AlGaAs micro-disk fabrication procedure detailing (a) initial AlGaAs-GaAs wafer composition; (b) HSQ deposition and e-beam exposure of micro-disk patterns; (c) RIE etch of the AlGaAs core layer, with the micro-disk structures protected by the HSQ resist layer; (d) HF 10:1 wet etch of AlGaAs sacrificial layer, distributing fully released AlGaAs micro-disks across GaAs substrate; (e) SEM image of AlGaAs micro-disk on GaAs substrate.

The fabricated micro-disks lack the anchored supports provided in previous TP

device architectures. To support low-loss whispering gallery modes the disk sidewall roughness must be kept to a minimum, breakage of the anchors would leave surface defects increasing device scattering losses. As such, the structures were left free-standing on the GaAs substrate, however by using high adhesion PDMS stamps the micro-disks can be controllably released from the substrate in a similar fashion to the typical TP method. All of the AlGaAs disk fabrication is achieved within the James Watt Nanofabrication Centre at the University of Glasgow.

4.2.3 High accuracy transfer printing of laterally coupled disk resonators

This section details the first attempt at micro-assembling a hybrid AlGaAs-on-SOI micro-disk resonator by TP. This was achieved by bonding an AlGaAs micro-disk onto the SOI receiver with a controlled lateral coupling gap to a Si bus waveguide, as shown by schematic in figure 4.4. The high alignment accuracy TP method for micro-disk structures is detailed in chapter 2.

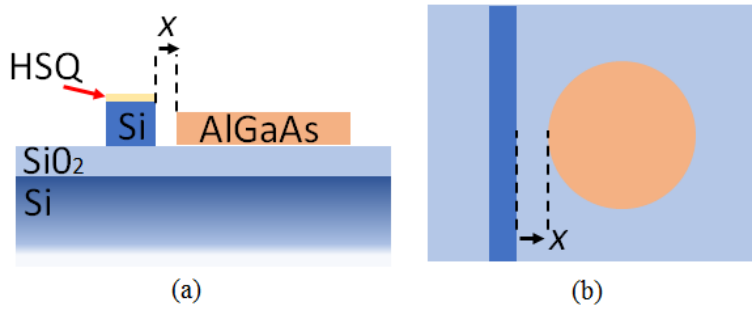

Figure 4.4: (a) Cross-section schematic of the laterally coupled AlGaAs micro-disk with a Si waveguide on the SOI platform. The lateral gap (x) is an edge-to-edge measurement calculated from the closest edges of both waveguide and micro-disk. (b) Top-view schematic of same structure detailing the lateral offset between the waveguide and micro-disk.

The target lateral coupling gap between bus waveguide and disk is x=100 nm,

with the close proximity enabling evanescent coupling into the fundamental whispering gallery mode of the disk resonator cavity. A HSQ layer of 100 nm is present solely on top of the waveguide with the substrate exposed surrounding the waveguide. This allows adjacent printing to the bus waveguide onto the silica cladding surface with full control over resonator coupling determined by lateral offset (x).

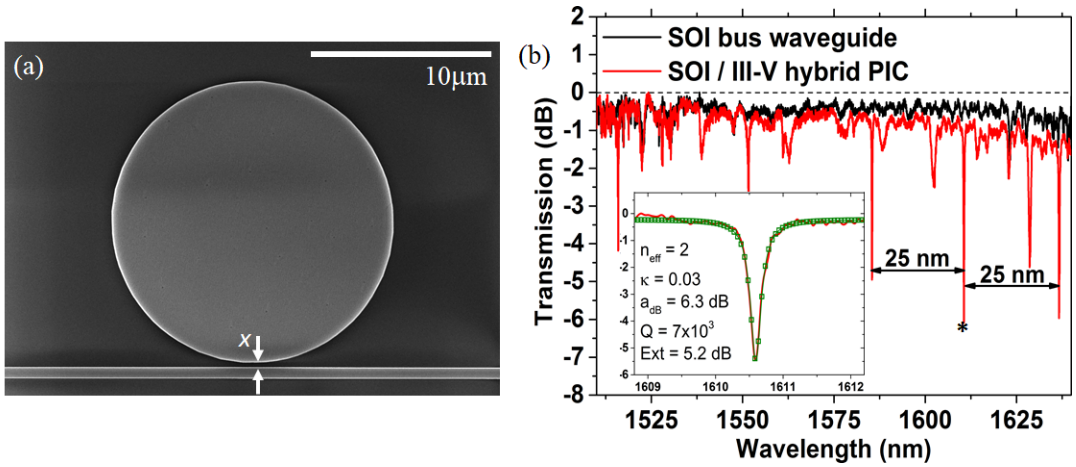

Figure 4.5: (a) Top-view SEM image of laterally coupled AlGaAs-on-SOI micro-disk resonator with a controlled lateral coupling gap x=100 nm. (b) Normalised transmission spectra of the Si bus waveguide prior to and post-assembly of the hybrid AlGaAs-SOI disk resonator. (Inset: Single resonance with extracted Q-factor, coupling coefficient, and distributed waveguide loss.)

Figure 4.5a shows an SEM image of the hybrid disk resonator of 10 μm diameter integrated by high alignment accuracy TP. Figure 4.5b details the subsequent optical transmission spectrum of the Si waveguide prior to and after the integration of the coupled AlGaAs micro-disk cavity, normalised to the Si waveguide maximum transmission. A free spectral range of ≈25 nm corresponds to the fundamental whispering gallery mode of the micro-disk resonator. By fitting the 1610 nm wavelength resonance to an all-pass resonator model, the Q-factor and coupling coefficient are extracted from the data, as shown in the inset of figure 4.5b. The device has a measured Q-factor of 7 x 10^3, coupling coefficient of 3 % and exhibits an ap-

proximate ∼6 dB resonance extinction level. Further to this, a finesse of 111 was calculated at λ_{res}=1610 nm. The low extinction and high losses can be attributed to localised notch defects on the outer disk region, lowering the achievable Q-factor. This notches are produced by discretisation during the EBL patterning. As light propagates through the disk cavity, it will scatter off the sidewall defects increasing the losses within the resonator and therefore is detrimental to the overall performance of the device.

Positional alignment accuracy measurement

The target lateral coupling distance (x) of the assembled micro-disk resonator was measured detailing the placement accuracy of the TP method. In the same fashion as the measurement technique demonstrated in chapter 3, an intensity line profile of the hybrid devices coupling region is extracted from a top-view SEM image, detailed in figure 4.6a. Calculation of x is achieved by the intensity contrast, imaging the contrasting edge profiles of the micro-disk relative to the bus waveguide. With respect to the sloped sidewall of the disk, a differentiation of the data signal over the scan range helps emphasise the change in pixel intensity for a more accurate measured representation of the lateral coupling gap. The data points included in the x calculation are detected as the minimum and maximum of the absolute value of the differentiated signal which corresponds to the FWHM of the separation distance, as shown in figure 4.6b. The SEM measurement error is as low as ±2.8 nm which is dominated by the pixel resolution of the imaging system.

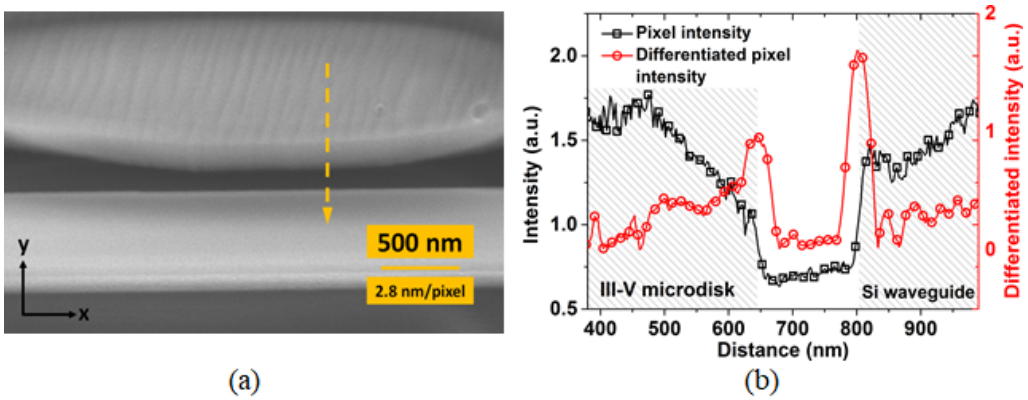

Figure 4.6: (a) Magnified SEM image with line profile showing the extracted profile intensity region. (b) Pixel intensity as a function of the lateral distance of the line profile. Intensity variations within the pixel intensity captures the Si waveguide, micro-disk and lateral gap positions. The absolute differentiated pixel intensity emphasises the edge regions.

A large variation in x across the coupler region was present due to the small ROC of the micro-disk cavity. As such, the coupling gap was measured over a region-of-interest (ROI) covering the coupling region, with the results plotted in figure 4.7 showing a variation in the coupling gap over the full region.

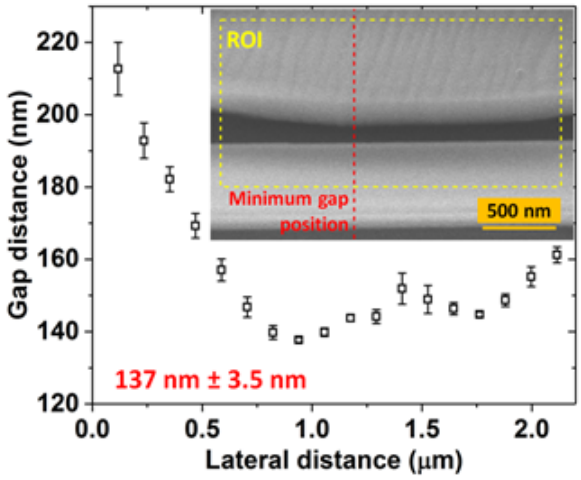

Figure 4.7: Coupling gap distance within a ROI surrounding the coupling region. (Inset: ROI region and position of the minimum gap location.)

The minimum measured coupling gap between the two structures was x= 137 nm ± 4 nm closely matching with the targeted gap distance of 100 nm, with the

error corresponding to the SEM measurement technique. The SEM image alongside the lateral coupling distance measurements in figure 4.6 show a variation in the micro-disk outer rim where the separation varies with a non-uniform curve. This is attributed to localised notch defects as previously mentioned. The continued work uses newly fabricated micro-disk structures where the notching defect has been removed, this will effectively reduce any losses from surface scattering and increase the hybrid resonator device overall performance.

4.2.4 High-Q factor vertically coupled disk resonators

As well as reducing the notch defects in the disk sidewalls, several variations to the hybrid disk layout were used to optimise its performance. An HSQ cladding layer is deposited over the silicon waveguides on the SOI receiver by spin-coating. This produces a planar surface for TP, increasing the adhesion properties whilst simultaneously defining a controlled vertical coupling separation.

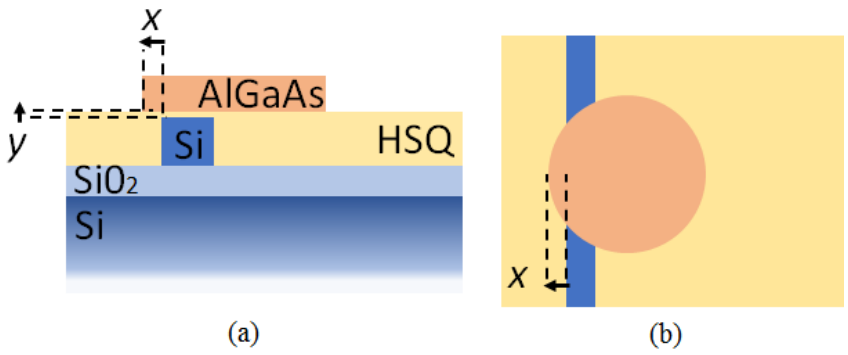

Figure 4.8: (a) Cross-sectional schematic of the vertically coupled AlGaAs micro-disk an Si waveguide enabling the controlled lateral and vertical coupling by transfer printing. The lateral gap (x) is an edge-to-edge measurement whilst the vertical gap (y) is calculated from the top of the waveguide to the bottom of the micro-disk. (b) Top-view schematic detailing the micro-disk overlapping the waveguide detailing the corresponding lateral offset.

The vertical coupling scheme between the WGM resonator has several advan-

tages over the lateral counterpart, such as denser device integration, higher device flexibility with control over both vertical and lateral coupling, as well as allowing selective excitation of different mode families within the micro-disk cavity which can't be achieved through typical lateral coupling mechanisms. A schematic of the assembly layout is shown in figure 4.8. The vertically coupled hybid AlGaAs-SOI disk resonator is shown by a top-view optical micrograph and corresponding transmission spectrum in figure 4.9. The disk resonator is 15 μm in diameter and has a lateral coupling distance between the disk and bus waveguide of 1 μm.

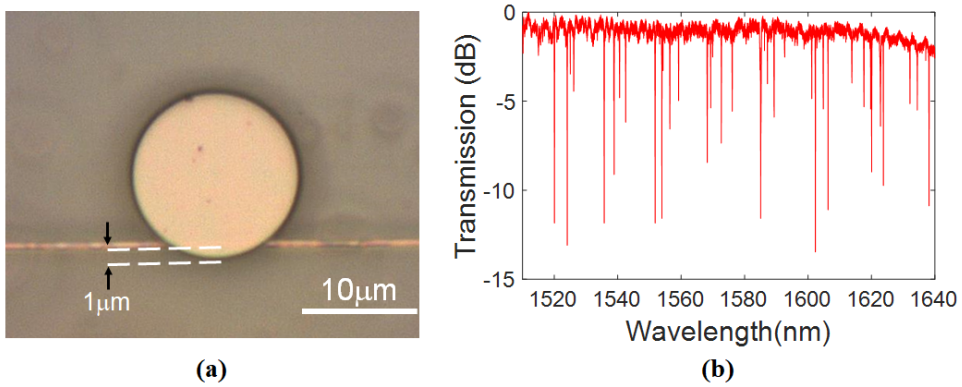

Figure 4.9: (a) Optical micrograph of a transfer printed hybrid AlGaAs micro-disk resonator on a Si waveguide with a lateral coupling offset of 1μm; (b) Normalised transmission spectra exhibiting multiple mode resonances across the full wavelength sweep range.

The lateral overlap of the disk resonator to the bus waveguide demonstrates the evanescent coupling to multiple mode families as indicated by the high number of resonances within each periodically spaced group throughout the transmission spectrum. The device exhibits an average loaded Q-factor of $\approx 25 \times 10^3$ across all mode families with a fundamental mode FSR$\approx$18 nm and exhibited resonant extinctions reaching $\approx$-12/13 dB.

Selective mode excitation

Micro-disk resonators are highly multimode, with different mode families excited as light travels into the inner regions of the cavity. Yet, to precisely control mode excitations requires high precision control of both the lateral and vertical separation. Previous techniques have been demonstrated [105], however complex fabrication protocols are required. The implementation of high alignment accuracy TP bypasses the multi-level fabrication processes by micro-assembling fully fabricated micro-disk resonators with high positional placement accuracy in both vertical and lateral directions.

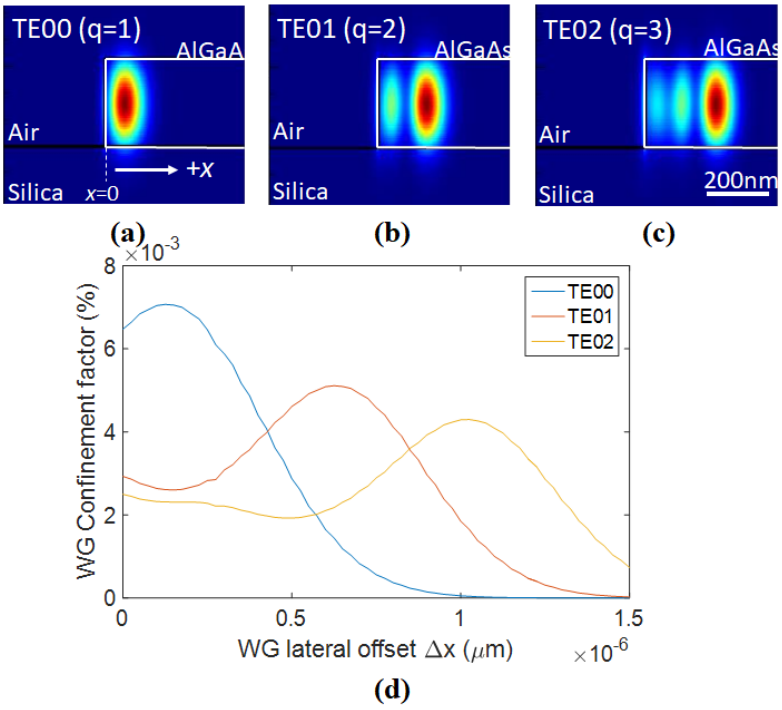

Figure 4.10: AlGaAs disk cross-section with simulated mode profiles. The variation in lateral offset enables the controlled coupling of the waveguide to different modes within the disk cavity, with higher order modes extending further into the disk cavity showing the (a) fundamental TE_{00} mode, (b) TE_{01} mode and (c) TE_{02} mode. (d) Plot of mode confinement as a function of waveguide lateral x for different modes. The vertical offset y is kept at a constant 100 nm. *Scale bar is identical for all simulation cross-sections.*

In order to map the variation of the mode excitation as a function of lateral displacement, multiple AlGaAs micro-disk resonators are transfer printed on top of single-mode Si straight waveguides to produce vertically coupled hybrid resonators. By varying the waveguide lateral position with respect to the disk cavity, the amount of modal overlap between the bus waveguide and disk varies causing a change in the mode coupling percentage. Simulated mode profiles of the multiple TE modes present in the disk cavity are shown in figure 4.10 a-c. As well as this, a measurement of the change in mode confinement within the waveguide as it is laterally shifted further into the disk cavity is plotted in figure 4.10d.

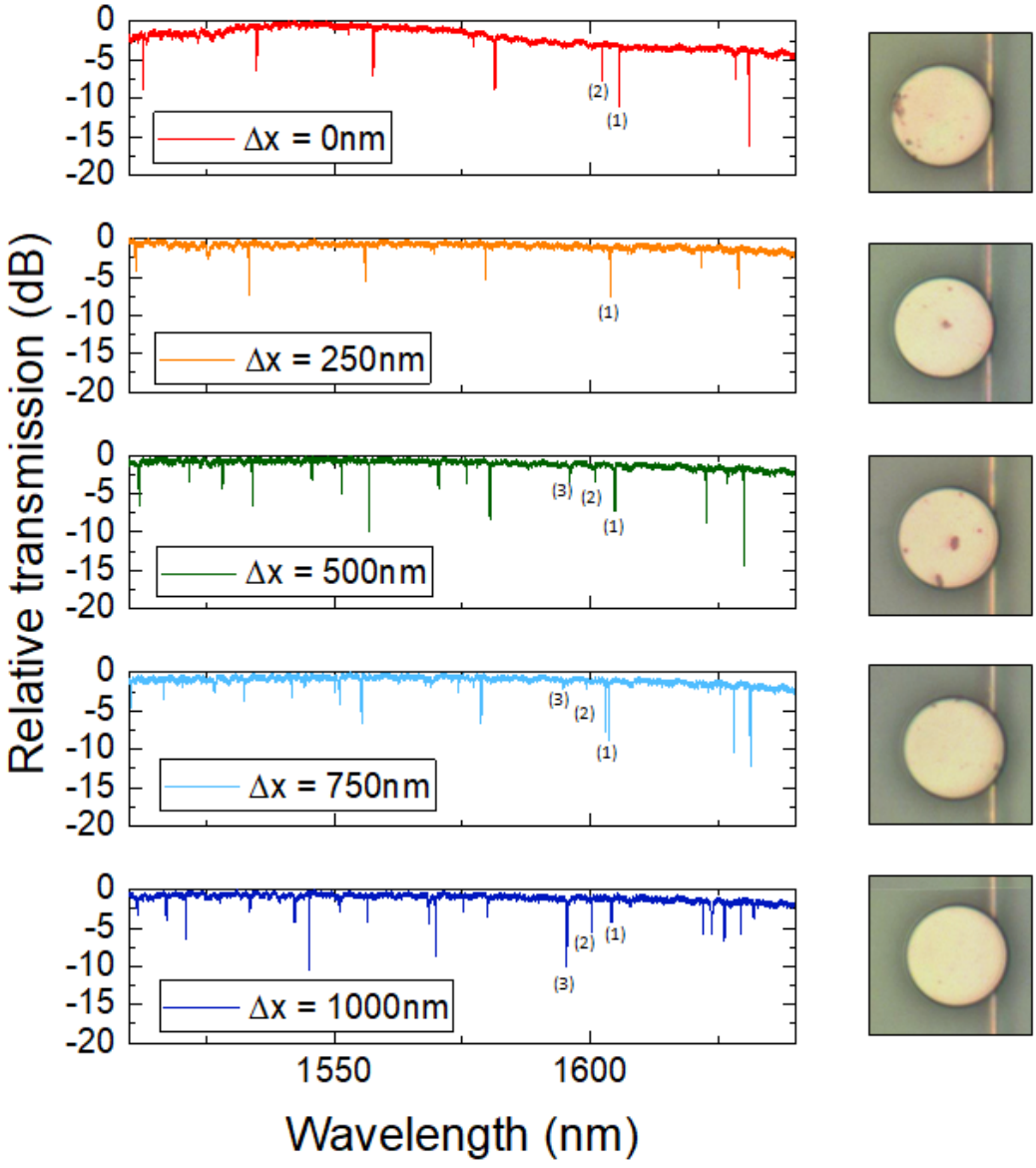

Figure 4.11: Optical microscope images of the hybrid resonator devices with varying x from 0 μm to 1 μm in steps of 250 nm (top to bottom, respectively) and accompanying normalised transmission spectra. Resonances dips within a single wavelength bunch are labelled with their corresponding radial mode numbers.

Figure 4.11 shows the multiple vertically coupled III-V/SOI hybrid resonators with controlled vertical and lateral coupling. They are detailed by top-view optical micrographs along with their accompanying optical transmission spectra. The lateral coupling distance of the waveguide edge to the micro-disk edge was increased from

0 to 1 μm with steps of 250 nm over five different devices. The movement of the waveguide further under the micro-disk couples light with different mode families within the cavity structures, as demonstrated by the variation in the resonant mode excitation as a function of the lateral displacement offset.

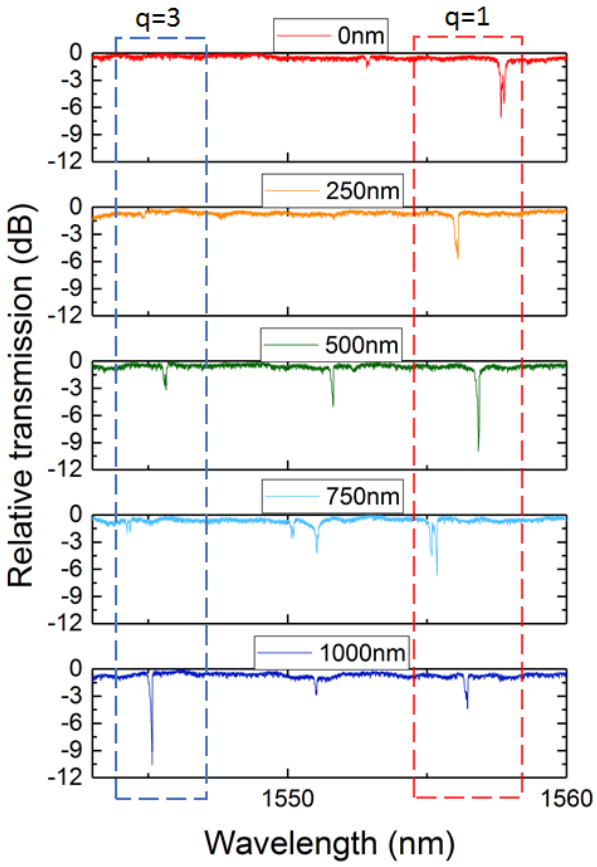

Figure 4.12: Cropped transmission spectra (1540 to 1560 nm) showing the resonant mode excitation shift from the fundamental (q=1) mode (red dashed box) to a higher order (q=3) mode (blue dashed box) by increasing the micro-disk to waveguide lateral offset x.

This shift in mode coupling is shown more clearly in figure 4.12, which contains a magnified section of the transmission spectra, situated around a centre wavelength of $\lambda \approx 1550$ nm. An increase in the lateral offset (x), when positioned further into the disk, caused a reduction in the coupling for the fundamental mode as detailed within the red dashed area. At the same time, once the lateral gap is large enough

the light is shown coupling into a secondary mode (blue dashed area).

The introduction of periodic scattering centres along the circumference of the devices during the EBL writing can lead to split resonances. This is attributed to the intra-cavity backscattering causing initially degenerate clockwise and anticlockwise propagating modes to couple and produce two standing wave solutions, [106]. The devices exhibit split resonances throughout their transmission spectra. In order to analytically measure the Q-factors, the theoretical fit of a single lobe is characterised, as shown in figure 4.13.

The measured loaded Q-factor and coupling coefficient values averaged from resonances throughout each of the the full spectra are shown in table 4.1. Several of the exhibited split resonances have been unable to provide clear and accurate measurement criteria and are left blank in the table. The results show a clear variation in the coupling of the fundamental mode with respect to the controlled coupling distance having a direct relation to the Q-factor, with a sudden jump in the coupled light to the higher order mode detailed once x reaches 1 μm.

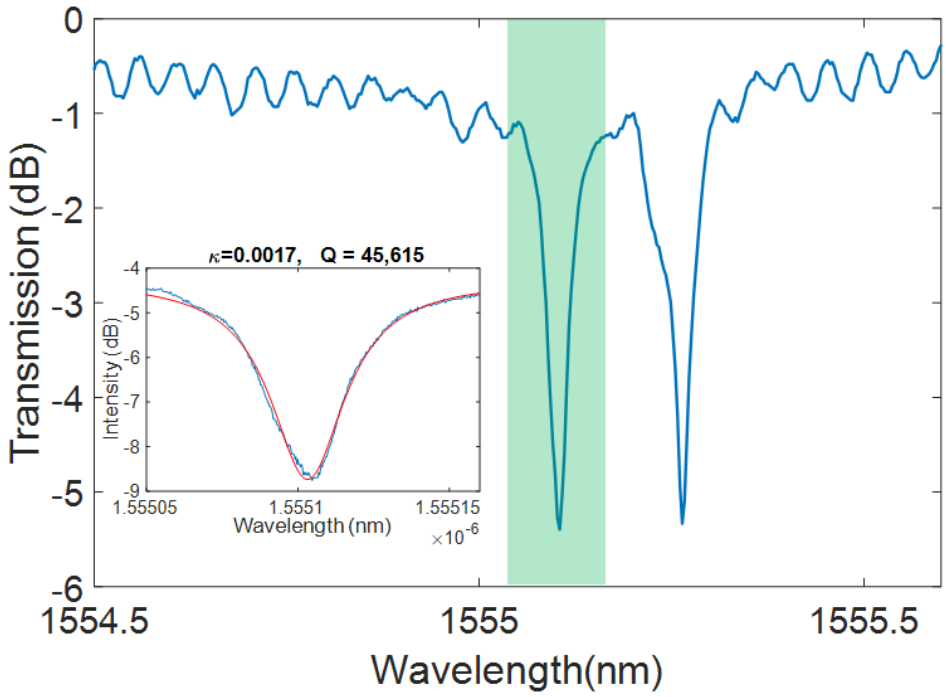

Figure 4.13: Spectra of split resonance with multiple lobes (inset contains a theoretical fitting curve to the left section of resonance).

The introduction of vertically coupled resonators have demonstrated the ability to reach loaded Q-factor values averaging at Q∼25,000 and reaching numbers of Q∼38,300 with extinctions of ∼15 dB. Comparisons with the side-coupled AlGaAs-SOI resonator devices in the previous section, an improved device performance is achieved. The improvement can be related to the better sidewall fabrication reducing scattered losses, with the vertical coupling enabling the coupling into higher order modes within the disk cavity. When compared to the state-of-the-art monolithic AlGaAs resonators, values range from Q≈7,500 for AlGaAs-on-GaAs [107] to Q≈100,000 for AlGaAs-on-Insulator [108]. Lower loaded Q-factor results compared with the AlGaAs-on-Insulator can be attributed to fabrication induced surface roughness, further evidenced by the split resonances.

Table 4.1: Selective mode coupling: Q-factor and coupling coefficients

x (nm)	Fundamental		Higher order	
	Q	κ	Q	κ
0	21,300	0.0108		
250	27,900	0.0089		
500	29,300	0.0084		
750	38,300	0.0081		
1000			30,000	0.0075

4.3 Micro-assembled AlGaAs-SOI resonators for nonlinear four-wave mixing

Nonlinear optics has greatly benefited from the progress in chip-scale integrated photonic systems. The introduction of highly compact devices, when compared against the typical fibre-scale architectures, enables dramatically increased non-linear responses through high optical modal confinement. This in turn produces much greater light-matter interactions over reduced distances. When it comes to deciding on a material platform there are many available, with each material's specific properties beneficial for a range of applications. Table 4.2 details the comparison of a list of popular nonlinear materials.

Table 4.2: Material nonlinear properties

Comparison of materials for nonlinear PIC technology				
Material platform	Ref. index	n_2 (m^2 W^{-1})	Re(γ) (m^{-1} W^{-1})	CMOS
AlGaAs [59]	3.3	2.6×10^{-17}	630	No
Silicon [109]	3.45	6.5×10^{-18}	320	Yes
Hydex [110, 111]	1.7	1.2×10^{-19}	0.22	Yes
SiN [112]	2.1	1.6×10^{-18}	16	Yes
InGaP [113]	3.1	6.0×10^{-18}	475	No

Four-wave mixing (FWM) is a nonlinear optical parametric process utilised for a

range of applications such as all-optical switching [114], signal generation [115] and wavelength conversion [116]. By taking advantage of resonant enhancement through the implementation of micro-resonators, increasingly high FWM nonlinear efficiency can be produced at low input powers.

Silicon's CMOS-compatibility and ability to produce highly compact resonator components makes it a desirable platform for nonlinear applications. However, it suffers from a high two-photon absorption (TPA) at 1550 nm which leads to free-carrier absorption (FCA) losses, in which the incoming photon energy is absorbed by free carriers produced by TPA, limiting the possible conversion efficiency of the nonlinear interaction process [117]. Unlike silicon, AlGaAs with its high nonlinear coefficient and lack of FCA losses can exhibit a much greater nonlinear conversion FWM efficiency. By transfer printing fully fabricated AlGaAs resonator structures into a pre-processed SOI passive system, we can produce a CMOS-compatible integrated photonic platform exhibiting the high nonlinearities of AlGaAs without the material nonlinear issues of silicon. This section demonstrates the application of our micro-assembled AlGaAs-on-SOI micro-disk resonators for nonlinear FWM. We report on the nonlinear optical characterisation of the hybrid resonator devices through efficient FWM at low optical on-chip power over multiple micro-disk device geometries.

4.3.1 Four-wave mixing overview

FWM is a $\chi^{(3)}$ nonlinear optical parametric process. It occurs when three photons from two input sources, signal and pump, propagate within a nonlinear material. The interaction and subsequent scattering leads to the generation of a fourth idler photon with a frequency difference related to the input frequencies [118], depicted

in figure 4.14.

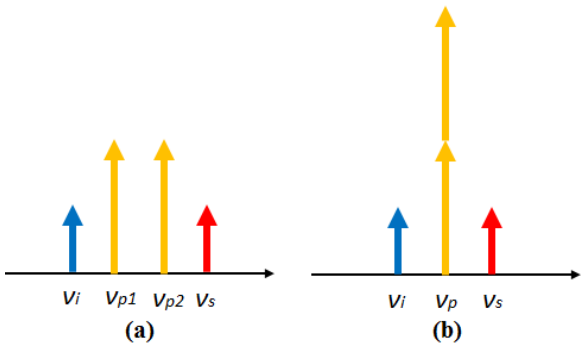

Figure 4.14: (a) Non-degenerate FWM and (b) degenerate FWM frequency diagrams.

Both degenerate and non-degenerate FWM can occur, as shown in figure 4.14a and b. In non-degenerate FWM, three frequency components were two are high intensity pump (ν_{p1} and ν_{p2}) and a third signal (ν_s) all combine to provide a fourth component known as the idler (ν_p) with a frequency difference defined in equation 4.1. In degenerate FWM, two pump photons have coinciding frequencies, as in equation 4.2, with both combining alongside the signal to provide the output idler peak

$$\nu_i = \nu_{p1} + \nu_{p2} - \nu_s, \tag{4.1}$$

$$\nu_i = 2\nu_p - \nu_s. \tag{4.2}$$

The continued work focuses on degenerate FWM processes, with a single high intensity input pump and signal beam generating an output idler beam.

The nonlinear FWM effect is highly dependent on the phase matching of the system. If a generated wave maintains a fixed phase relation with the material systems nonlinear polarisation, it is able to extract energy most efficiently from the interacting waves. Phase matching in FWM applies when the wave vector relationship of

the interacting waves equals zero, detailed by [118]:

$$\Delta k = 2k_p - k_s - k_i = 0, \tag{4.3}$$

where $k_{p,s}$ are the interacting pump and signal wavevector components. When they are in phase, as shown in equation 4.3, the field emitted by each corresponding dipole adds coherently in the same direction, increasing the total radiated power. If phase matching is not satisfied, known as a phase mismatch ($\Delta k \neq 0$), the emitted fields partially cancel each other depending on the phase difference, which can lead to a considerable decrease in the efficiency of the nonlinear processes.

The effects of dispersion in a waveguide system can impact on the achievable efficiency. Dispersion causes a variation in the refractive index as a function of the input frequency, and as a result perfect phase matching of collinear interacting beams must satisfy the condition:

$$\frac{n_p(2v_p)}{c} - \frac{n_s v_s}{c} = 0, \tag{4.4}$$

where $n_{p,s}$ are the refractive indices for the relevant pump and signal frequencies. With the refractive index varying monotonically with frequency, the ability to perform perfect phase matching becomes increasingly difficult. However, by reducing the amount of dispersion, or minimising the frequency difference between interacting waves, phase matching can be increased to maximise the overall achievable nonlinear efficiency.

Optical parametric gain is the phenomenon when the output is amplified by the input pump beam during the nonlinear FWM process. The condition for parametric gain is detailed below:

$$G_{max} = exp(\gamma P f_{i,j,k} l), \tag{4.5}$$

$$\gamma = \frac{2\pi n_2}{\lambda A_{eff}}, \tag{4.6}$$

where γ denotes the nonlinear parameter, P is the on-chip pump power, n_2 the nonlinear refractive index, A_{eff} defines the area a waveguide mode covers in the transverse dimension [119], $f_{i,j,k}$ is the overlap integral of the pump, signal, and idler wavelength modes and l is the interaction length [120]. Regarding the FWM efficiency measurement, this is the case when the output idler beam power is greater than the input signal power subject to a positive nonlinear efficiency.

4.3.2 AlGaAs and silicon FWM comparison

SOI integrated photonic systems have been used for a variety of nonlinear applications. However, the obtainable SOI FWM conversion efficiency is limited by high two-photon absorption (TPA) and free-carrier lifetime. An alternative candidate has been realised in AlGaAs. The III-V alloy material has a high refractive index (n=3.24) enabling the fabrication of highly compact devices geometries comparitive to silicon, whilst it also has the ability to tailor the bandgap helping mitigate the TPA and free carrier lifetime for the realisation of high FWM efficiencies [121, 59].

To compare both silicon and AlGaAs solely on their nonlinear properties, we calculate their FWM efficiency based on the theoretical simulation and analysis of two identical ring resonators. Each resonator model has identical geometry with a radius 15 μm, cross-sectional area (220 nm x 500 nm), as well as a cross-coupling coefficient value of κ=0.018, and distributed propagation losses of 3.5 dBcm^{-1}. This enables the comparison of the material nonlinear coefficient (γ) and nonlinear refractive in-

dex (n_2). Lumerical FDE mode simulations calculate the waveguide dispersion (d) and effective mode area of the devices, with the mode area used for the calculation of the γ value of both materials utilising equation 4.3.1. The n_2 values are provided in table 4.2. The simulated values of effective mode area are 0.133 μm^2 for silicon and 0.172 μm^2 for AlGaAs calculating a γ value of 198 W^{-1} m^{-1} and 610 W^{-1} m^{-1}, respectively. Dispersion values were calculated as $d_{Si} = 1500$ ps/nm $\cdot$ km and $d_{AlGaAs} = 2300$ ps/nm $\cdot$ km.

The FWM efficiency (η) is defined by the ratio between the generated idler and input signal powers:

$$\eta = \frac{P_{idler}}{P_{signal}} = |\gamma P_{pump} L_{eff}|^2 F_p^2 F_s F_i, \tag{4.7}$$

$$L_{eff}^2 = L^2 exp(-\alpha L) \left| \frac{1 - exp(-\alpha L + j\Delta k L)}{\alpha L - j\Delta k L} \right|^2, \tag{4.8}$$

where P_{idler} and P_{signal} are the idler and signal powers respectively, L and L_{eff} are the cavity geometric and effective lengths, α is the average field propagation loss coefficient incorporating both the two-photon and free carrier non-linear losses, and the phase mismatch is given by Δk. $F_{p,s,i}$ is the square of the field enhancement factors for the pump, signal and idler, measured by:

$$F_{p,s,i} = |\frac{r}{1 - texp(-\frac{\alpha L}{2}) + jk_{p,s,i}L}|^2, \tag{4.9}$$

where r and t are the cross-coupling and transmission coefficients of the resonator-bus waveguide coupler. The final parameters of interest are each material's nonlinear loss, being the TPA and FCA material values. The nonlinear TPA for silicon and

AlGaAs are 0.7 cm/GW and 0.1 cm/GW, whilst the free carrier absorption values are 500 ps and 40 ps, respectively [122, 109, 123]. Figure 4.15 plots the FWM efficiency - as calculated from equation 4.7 - for both Si and AlGaAs resonators, with the Si efficiency level calculated both with and without TPA revealing the effects of nonlinear loss within the system.

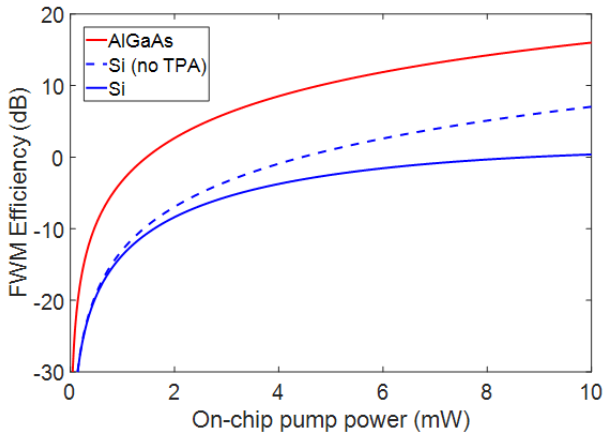

Figure 4.15: Theoretical plot of silicon versus ALGaAs FWM efficiency as a function of on-chip power. Silicon's efficiency level is calculated with and without TPA losses to show the effect of nonlinear absorption losses on the nonlinear response of such devices. A centre wavelength of 1550 nm was used for the measurements with FSR≈6.1 nm.

The AlGaAs is shown to have a much higher FWM efficiency level compared to both silicon resonator systems, primarily due to the high nonlinear refractive index (n_2) and therefore high nonlinear coefficient of the AlGaAs material platform. Whilst the efficiency of the silicon suffering from TPA saturates at the higher pump powers. The comparison details the advantages of providing a hybrid resonator system for nonlinear applications.

4.3.3 Experimental set-up and measurement

The experimental setup shown in figure 4.16 is used in order to carry out the FWM experiments. A continuous-wave (CW) laser source outputs both the pump and signal beam. The pump beam is fed into an erbium doped fibre amplifier (EDFA) passing through an attenuator and polarisation controls into the input fibres. Both pump and signal are tuned to TE-polarisation before being combined by a 90:10 fibre coupler. A small fraction of the pump beam is fed to a power meter for real-time power measurements with the majority coupled on-chip, interacting with the resonator device. The output light is collected by a tapered fibre which is connected to an optical spectrum analyser (OSA) for power measurements of the pump, signal and idler beams.

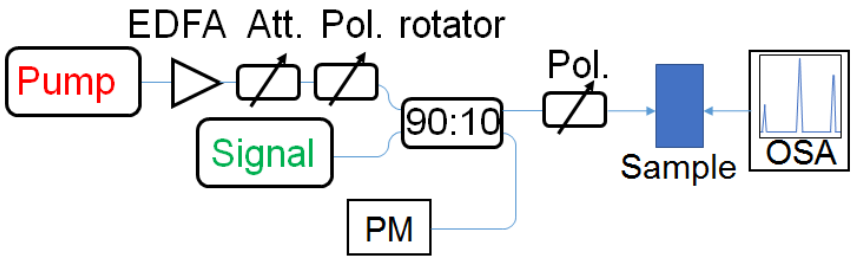

Figure 4.16: Schematic of the measurement set-up for FWM. EDFA: Erbium doped fibre amplifier, PM: Power meter, OSA: Optical spectrum analyser.

The measurement of the FWM is given by the signal-to-idler conversion efficiency ($\frac{P_{idler}}{P_{signal}}$), and is split into several steps. The pump beam (P_{pump}) and signal beam (P_{signal}) output powers are measured individually from each other, with the wavelength tuned away from any disk resonance to provide the full optical power propagating through the waveguide. Both pump and signal outputs are shown in figure 4.17a off-resonance to the disk. The residual noise floor in the spectra is a factor of the amplified spontaneous emission (ASE) from the EDFA. Following this, both

pump and signal wavelengths are red-shifted to wavelengths on-resonance, figure 4.17b. The spectra demonstrates a drop in power with respect to the off-resonance as light is coupled into the resonator. Interaction of the pump and signal within the resonator causes the production of a third peak known as the idler with an output power (P_{idler}). The wavelength of the idler is given by $\lambda_i = 2\lambda_p$ - λ_s where λ_i is the idler wavelength, λ_p is the pump wavelength, and λ_s is the signal wavelength.

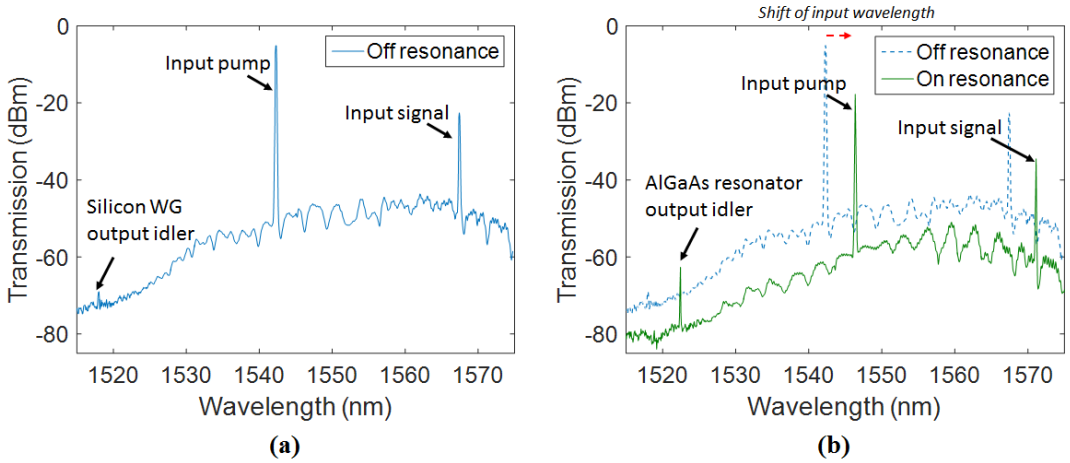

Figure 4.17: FWM spectra showing (a) off-resonance pump and signal beam output peaks and off-resonance silicon waveguide generated idler peak; (b) on-resonance pump and signal beam peaks accompanied by output AlGaAs resonator generated idler peak.

4.3.4 Silicon waveguide non-resonant four-wave mixing

Figure 4.17a details the output transmission of the hybrid resonator when both pump and signal transmission are off-resonance to the micro-disk resonator. This is the case when no light is coupled into the resonator, instead propagating directly through the silicon waveguide. However, it is shown that off-resonance there is still the generation of an idler peak at ≈1516 nm with a FWM efficiency of -48.3 dB at P_p=0.3 mW, produced from the nonlinear FWM of the silicon waveguide. The predicted FWM efficiency level for a silicon strip waveguide with a cavity length of 1 mm is measured

as -45 dB at P_p=0.3 mW, calculated using the non-resonant conditions of equation 4.7. The experimental data depicts an overlap to the expected efficiency level. By red-shifting both pump and signal beams to an on-resonance wavelength the light now couples directly into the AlGaAs resonator cavity, this on-resonance condition is shown in figure 4.17b. With the pump and signal beams interacting within the resonator cavity, the FWM generated idler peak increases by an efficiency level of 6.3 dB as shown in figure 4.17b. The increased output idler peak power introduces the benefits of implementing a hybrid resonator system. By further increasing the input pump power, the efficiency of the hybrid AlGaAs-SOI resonator can be further increased without the additional material issues regarding silicon's TPA and FCA losses, which is demonstrated in the continued sections.

4.3.5 FWM using micro-assembled AlGaAs-on-SOI micro-disk resonators

The FMW experiment was carried out on two different device geometries, a hybrid micro-disk resonator of 15 μm diameter and another of 10 μm diameter. To directly measure the variation in efficiency as a function of effective mode area (A_{eff}), one device is coupled to the fundamental mode whilst the other is coupled to a higher order mode with a much larger A_{eff}. The comparitive FWM efficiencies area measured as a function of on-chip optical pump power for both devices.

15μm micro-disk

A 15 μm diameter micro-disk resonator was micro-assembled to a silicon bus waveguide on a SOI platform with a lateral offset of $x\approx$2 μm, with the bus waveguide coupling to the micro-disks higher order TE modes.

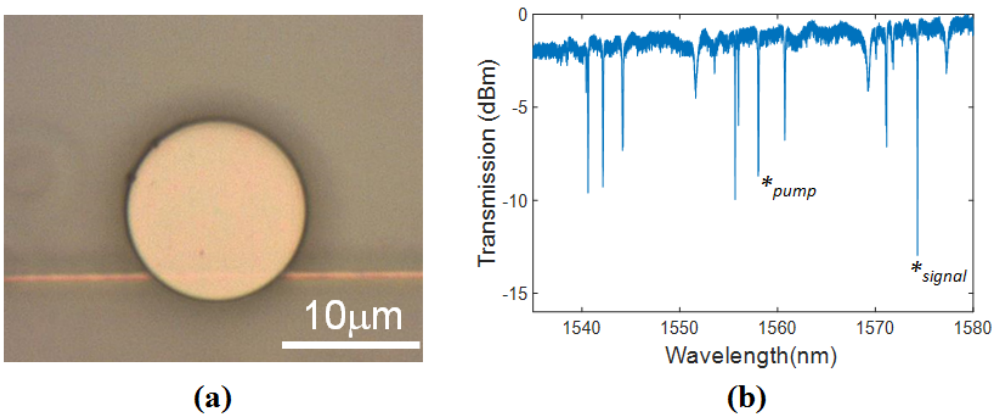

Figure 4.18: (a) Optical micrograph of hybrid resonator with lateral offset of $x = 2$ μm. (b) Resonant spectra of multiple mode-families, labelled are the resonant peaks used for pump and signal beam tuning.

An image of the micro-assembled resonator structure is shown in figure 4.18 alongside a resonant transmission spectra. The two successive mode resonances used during the FWM experiment for both the pump and signal beam tuning are highlighted, with resonant wavelengths of λ_{rp} ≈1558 nm and λ_{rs} ≈1574 nm. The measured Q-factor of λ_{rp} is ∼22,000 and λ_{rs} is ∼23,000 with a FSR≈16 nm. A measure of the nonlinearity of the device is given by the nonlinear coefficient (γ). To determine γ requires the effective mode area (A_{eff}) as expressed by the equation $\gamma = 2\pi n_2/\lambda\ A_{eff}$ [124]. The effective mode area of the mode within the disk is calculated by taking an intensity integral from a simulated TE mode profile using lumerical,shown in figure 4.19. The higher order TE mode primarily overlapping the waveguide coupler region had a measured A_{eff} of ∼0.61 μm^2

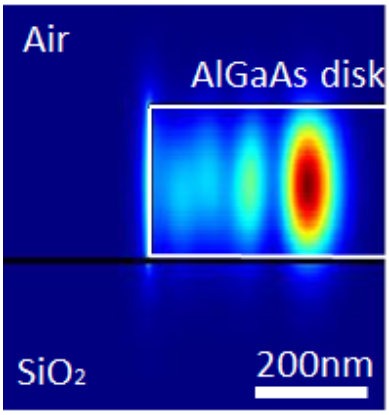

Figure 4.19: Mode simulation showing a partial cross-section of an airclad AlGaAs micro-disk on top of a silica substrate, with a radius of curvature of 7.5 μm. The outer left hand edge of the micro-disk is shown in the image containing the simulated higher order mode profile.

The experimental results of the FWM achieved a maximum efficiency level of η=-25.54 dB at an on-chip optical pump power of 4mW, with the variation in FWM efficiency as a function of on-chip optical pump power shown in figure 4.20a.

The experimental data is compared to a theoretical prediction of FWM efficiency. The theoretical FWM efficiency is calculated using equation 4.7, under the following conditions. The gamma parameter is calculated using the literature value for n_2 and a value for the modal effective area extracted from the mode simulation. Values for the field enhancement factors and effective length are calculated from the measured resonator losses, coupling coefficient and dispersion. The theoretical curve matches the experimental FWM data. Figure 4.20b demonstrates a quadratically increasing efficiency level, indicating a reduced saturation with respect to the AlGaAs material platform utilised. For the hybrid resonator we obtained a nonlinear coefficient of γ=133 $(\mathrm{Wm})^{-1}$.

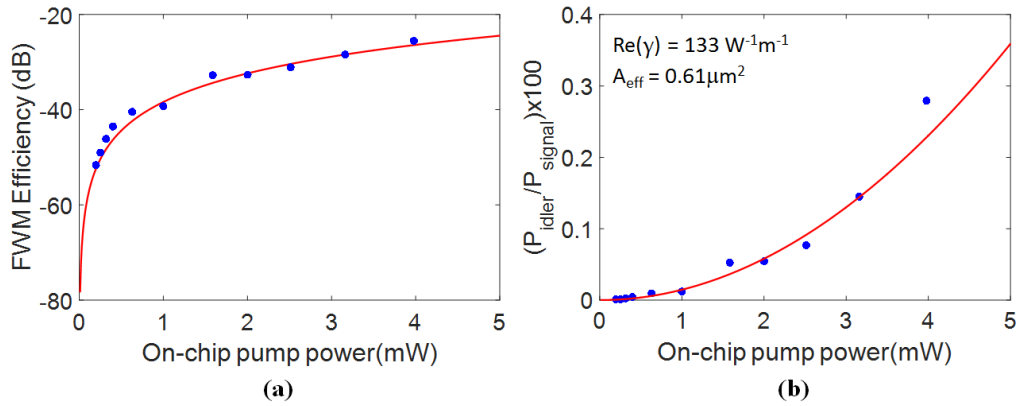

Figure 4.20: (a) FWM efficiency as a function of on-chip pump power, blue dots are the experimental data and theoretical curve is given by the red line; (b) FWM efficiency idler to signal ratio as a function of on-chip optical power with non-linear coefficient and effective mode area calculated and provided within the inset.

The reduced efficiency is due to the large excited mode area, owing to the excited mode situated further into the disk regarding the lateral waveguide placement. The larger area reduces the average electric field intensity within the resonator, limiting the non-linear interaction strength within the device. To fully take advantage of the micro-disk structure the light has to be coupled to the fundamental mode situated at the outer region of the cavity. This reduces the effective mode area increasing the field intensity within the resonator structure.

10μm micro-disk

The next device used to carry out FWM experiments is a 10 μm diameter hybrid AlGaAs-SOI micro-disk resonator. The bus waveguide is coupled to the fundamental mode for reduced modal area for increased power density within the device. As well as this, a smaller disk diameter further reduces the mode area by reducing the ROC.

Figure 4.21a details a top-view optical micrograph of a 10 μm diameter AlGaAs micro-disk resonator integrated with a SOI bus waveguide. The micro-disk and waveguide have a controlled lateral offset of x≈750 nm, with the waveguide coupling

to the fundamental mode of the resonator. A truncated resonant spectra of the hybrid resonator is shown in figure 4.21b detailing the mode resonances used for the FWM experiment, the full spectra is shown in figure 4.11. The two successive mode resonances used during the FWM experiment for both the pump and signal beam tuning are highlighted, with resonant wavelengths of λ_{rp} ≈1556 nm and λ_{rs} ≈1579 nm. The measured Q-factor of λ_{rp} is ∼22,500 and λ_{rs} is ∼26,500 with the device having a FSR≈23 nm.

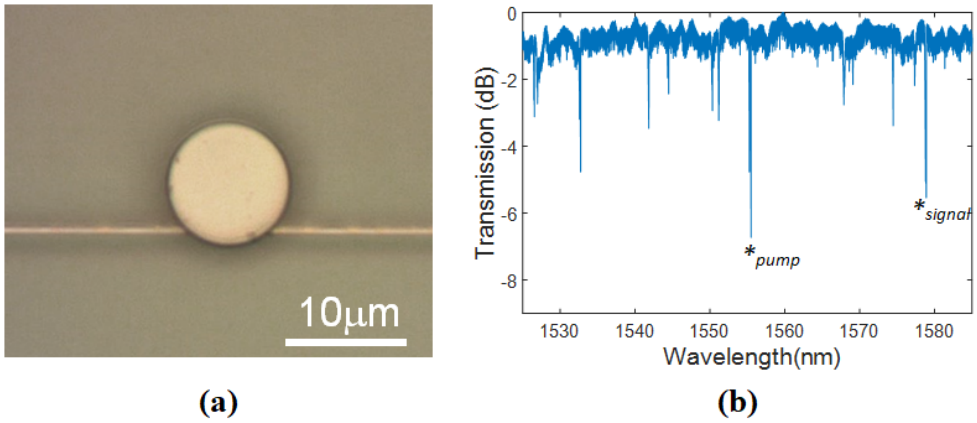

Figure 4.21: a) Optical micrograph of hybrid resonator device with a lateral offset of $x = 750$ nm, coupled primarily to the fundamental TE_{00} mode within the cavity; (b) Resonant spectra labelling the resonant peaks for which the pump and signal beam are tuned for the FWM experiment.

A simulated mode profile is utilised to determine the A_{eff} of the resonant excited mode within the micro-cavity, this is shown in figure 4.22. With regards to the higher order mode in the previous section, the fundamental mode closer to the edge of the micro-disk exhibits a much reduced modal area of A_{eff}=0.25 μm^2. The reduced mode area increases the nonlinear interaction strength within the structure causing an increase in the nonlinear coefficient (γ).

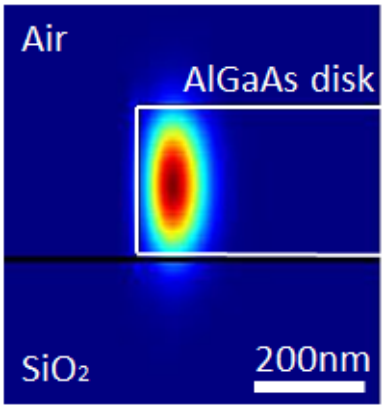

Figure 4.22: Mode simulation showing a partial cross-section of an airclad AlGaAs micro-disk on top of a silica substrate, with a radius of curvature of 5 μm. The outward left hand edge of the micro-disk is shown in the image containing the simulated fundamental mode profile.

Figure 4.23 details the FWM efficiency as a function of the optical on-chip pump power. A maximum experimentally measured nonlinear efficiency of η=-25 dB was achieved at a pump power of 2.5 mW, with the device's nonlinear coefficient value calculated as γ=325 $(\mathrm{Wm})^{-1}$ using the simulated A_{eff} value. The theoretical curve details an accurate comparison to the experimental FWM efficiency measurements. The experimental results demonstrate an increasing trend in efficiency with regards to the low TPA of AlGaAs, with higher efficiencies capable at increased pump powers. The maximum measurable optical pump power didn't reach the same level as for the previous 15 μm higher order resonator, section 4.3.5. As the high intensity pump beam pushes the resonance to longer wavelengths the cavity state becomes much more sensitive to fluctuations in the coupled power. This instability can cause the resonance to spontaneously jump back to its initial cold-cavity state, with the resonant wavelength de-tuning from the pump beam stopping all nonlinear FWM processes. The effect is more prominent in higher-Q resonators due to the larger resonant wavelength shift exhibited. When this is combined with environmental fluctuations in the fibre-to-facet alignment giving rise to sudden changes in the cou-

pled power, the cavity instability can become too large for reliable measurements at the higher power regime. One possible solution would be the tuning of the resonance to help limit this effect, this has been shown in previous work by thermal tuning of the resonance wavelength [125].

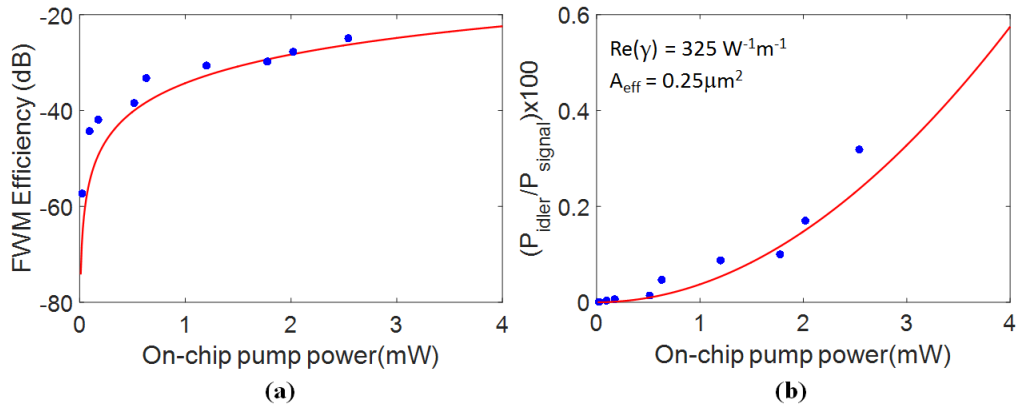

Figure 4.23: (a) FWM efficiency as a function of on-chip pump power for the 5 μm radius hybrid resonator, blue dots are the experimental data and theoretical curve is given by the red line; (b) FWM efficiency idler to signal ratio as a function of on-chip optical power, with the calculated non-linear coefficient and effective mode area provided within the inset.

The FWM efficiency is reduced from the predicted level in figure 4.15 for AlGaAs resonators of similar geometries. The main reason for this is due to high dispersion effects experienced by the resonator device. When considering the exhibited FSR, the idler generation falls largely outside the respected resonance limiting the intensity enhancement factor experienced and therefore the conversion efficiency. The state-of-the-art for AlGaAs-on-insulator micro-resonator contains a measured FWM efficiency at -12 dB for 7 mW on-chip optical powers [59]. From the fitted curve, the efficiency level at a comparable optical pump power is calculated as -17.7 dB. As such, the produced integrated AlGaAs-SOI TP micro-resonators can be seen as a potential for nonlinear photonic applications, strongly influenced by the flexibil-

ity and simplicity of the CMOS-compatible integration method. To achieve greater efficiencies would require the switching to single-mode low dispersion AlGaAs resonators. The reduced effective mode area would allow much greater efficiencies to be achieved. The obtainable FWM efficiency levels have been previously shown in the comparison plot in figure 4.15, with FWM efficiency reaching the gain regime.

4.4 Conclusions

This chapter describes the work into the design and fabrication of free standing AlGaAs micro-disk cavities. This includes the modelling of vertically confined micro-disk cavities as a means to suppress the complex resonant conditions which can inhibit disk resonator devices. A discussion into the fabrication techniques is detailed into the production of free-standing AlGaAs micro-disk cavities ready for transfer printing.

Both lateral and vertical integration of the fully fabricated disk structures to Si bus waveguides on the SOI platform is explained, with the production of hybrid WGM resonators demonstrated in a fully back-end process, including analysis on the lateral placement accuracy of micro-disk resonators by transfer printing. Vertically coupled hybrid AlGaAs-on-SOI WGM resonators with Q-factors as high as ≈25,000 are demonstrated, with the selective coupling of light into multiple mode families within the disk cavities enabled by the precise control over the lateral and vertical separations during the integration of the AlGaAs micro-disk cavities to the underlying silicon bus waveguides.

Following this, the characterisation of the hybrid resonator device nonlinearity is achieved by four-wave mixing experiments, with a measured nonlinear coefficient of γ=325 $(\mathrm{Wm})^{-1}$. Nonlinear FWM efficiency levels reaching -25 dB at a low on-

chip optical power of 2.5 mW are produced on SOI, without exhibiting the typical saturation loss experienced by silicon at $\lambda \approx$1550 nm due silicon's high TPA and FCA. The results demonstrates the capability of transfer printing as a promising method for the production of a full suite of nonlinear processes within the SOI platform by the integration of hybrid passive resonator devices.

Chapter 5

Conclusions and future research

This section summarises each chapter's relevant research achievements. Further to this, a brief description of the future research goals of each individual chapter's specific focus are detailed. The motivation behind the research was the development of TP as a method for producing complex and highly functional large-scale PIC technologies, with the focus on establishing a nanoscale alignment method with the ability to integrate compact, guided wave components from multiple material platforms in a parallel and scalable fashion. The motivation of the thesis, respective outcomes from the research, and future research goals described in this section are crucial in working towards this aim.

5.1 Nanoscale absolute alignment for transfer printing

Chapter 2 details the development and implementation of a cross-correlation alignment procedure with the goal of nanoscale precision absolute alignment of devices by TP. An alignment method was developed for chip-to-chip integration of suspended membrane devices, free-standing micro-disk resonators, and NW lasers with the specific goal of the last being the large-scale selective alignment of NWs based

upon their specific optical and geometric properties. The chapter details first the cross-correlation alignment method, followed by the systematic absolute alignment accuracy once implemented within the TP system. This is then followed by the statistical alignment measurement for chip-to-chip TP of Si membranes across multiple substrates. For the systematic alignment, an average absolute accuracy of 50±40 nm was demonstrated. Following this, the statistical alignment accuracy of TP devices across multiple samples was measured with a lateral absolute accuracy of ±380 nm (3σ) and rotational accuracy of ±4.8 mrad (3σ). This is to our knowledge the highest demonstrated alignment accuracy for TP to date and the first measured rotational accuracy.

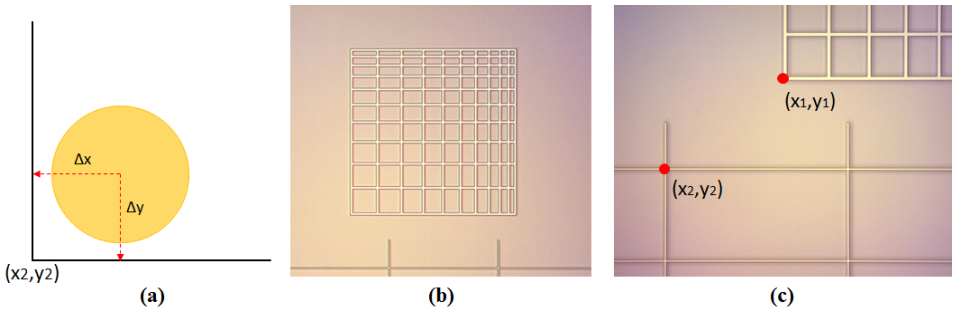

Figure 5.1: (a) Schematic illustration of a micro-disk containing the required measurements for a statistical analysis. (b) Optical microscope image of fabricated alignment mark and etched lateral lines used for the micro-disk statistical alignment project; (c) Magnified image of lateral lines detailing the relative alignment coordinates corresponding to the schematic in (a).

With regards to the cross-correlation alignment analysis, the same level of rigour has not been fully developed for the explained device alignment methods presented, particularly the cross-correlation absolute alignment of free-standing micro-disk structures. A receiver substrate containing alignment grid markers and lateral etched lines in both vertical and horizontal directions has already been produced, as detailed in figure 5.1. The goal is to use the alignment method to integrate micro-disks to an

absolute position on this receiver substrate with positions relative to the lateral lines. The expected and experimental lateral offsets (Δx, Δy) will be measured by similar techniques used for the statistical chip-to-chip alignment in chapter 2. This can also be achieved for the absolute alignment accuracy of NW lasers using TP, with similar techniques used to provide the lateral and rotational accuracy.

The final project would be the measurement of parallel TP of membrane devices. This would follow the exact measurement protocol of the membrane chip-to-chip alignment, however the TP of an array of membranes all in a single operation would be achieved. The absolute alignment of parallel TP across mm-scale, even to cm and wafer scale would be highly beneficial to the overall goal of providing a scalable and highly parallel integration technique suitable for large-scale PIC technologies.

5.2 Transfer printing of ultra-thin membrane silicon photonic devices

Chapter 3 details the development and micro-assembly of ultra-thin suspended Si membrane resonators with a receiver SOI substrate, with a goal of producing vertically assembled all-pass micro-resonator devices.

Ultra-thin (150 nm) Si membranes containing shallow-etched ridge resonators were fabricated using e-beam lithography. These are subsequently suspended above their native SOI substrates enabling the release and transfer to different substrates by TP. By utilising the nanoscale alignment TP method, the micro-assembly of all-pass micro-resonators onto a receiver SOI platform with loaded Q-factors reaching 4,000 was achieved. This was limited by notch defects in the e-beam patterning stage of the micro-disk fabrication process and causing increased scattering losses. Future work removed this defect, with the introduction of a planar HSQ cladding

layer increasing the bond strength whilst simultaneously providing more flexibility with regards to the device coupling gap. By varying the lateral coupling offset between the membrane micro-resonator and bus waveguide, the resonator coupling and subsequent Q-factor was controlled. Following this, measurement of average absolute placement accuracy was calculated as low as 100±70 nm across multiple assembled devices. The final section describes work into the micro-assembly of multiple stacked membrane layers by TP. The production of a silicon-silica DBR five layer stack composed of individually printed membranes with thickness's of 220 nm - 100 nm was demonstrated, with the device visible wavelength reflectance comparable to simulated reflectance measurements.

There are several future research paths possible pertaining to this chapters main focus, with emphasis placed on the production of 3D architectures currently requiring complex monolithic fabrication techniques. Firsly, the technique could be advantageous in the field of orbital angular momentum (OAM) photonic devices, where Si micro-resonators have in the past been used for the production of compact and efficient OAM emitters [126].

Figure 5.2: Illustrations of integrated (de)multiplexer OAM devices composed of (a) Ω-shaped waveguides containing sidewall gratings; (b) Concentric micro-resonators vertically coupled to straight waveguides sections. From [5]

The idea of concentric OAM emitters as a means to produce a (de)multiplexer

array has been put forward before, with some ideas detailed in figure 5.2. By combining this technology with Si membrane TP, concentric OAM resonators can be fully fabricated on a single membrane where they can then be integrated with bus waveguides. However, the two approaches have their own limitations, such that the Ω-shaped waveguide architecture performance level would be reduced regarding the incomplete ring hindering the achievable mode purity. The concentric micro-ring is more attractive, however requires a multi-level fabrication process involving wafer bonding steps. By implementing the concentric OAM micro-ring resonator configuration alongside the membrane vertical assembly approach from this chapter bypasses the need for complex multi-layered fabrication steps, making the production of these devices more adept for medium to larger scaled manufacturing.

Another possible research direction would be the integration of highly compact concentric micro-resonator cross-grid arrays, for applications in high-data rate matrix switches used within interconnection networks [57]. The micro-assembly established within the chapter would enable high density arrays of micro-resonators vertically integrated over multiple layers. This approach would increase achievable data-rates per integrated chip-space.

5.3 Hybrid integration of WGM resonators by transfer printing

The final chapter describes research into the development of free-standing AlGaAs micro-disk resonators and subsequent TP to non-native SOI substrates by high accuracy cross-correlation alignment.

Vertically coupled hybrid AlGaAs-on-SOI WGM resonators with average loaded Q-factors measured at ∼25,000 were demonstrated. The values presented com-

pare against current state-of-the-art monolithic Si micro-resonators. Further to this, the selective excitation of multiple mode families within the WGM resonators was demonstrated, depicted by variations in coupling percentage and Q-factor of resonant modes across five micro-assembled devices with coupling gaps varying from 0 nm to 1 μm in steps of 250 nm. The nonlinear capability of the hybrid resonators was analysed by FWM experiments with the objective of demonstrating FWM without the nonlinear saturation losses of TPA and FCA currently limiting fully monolithic SOI equivalent devices. Nonlinear efficiency levels reaching -25 dB at low on-chip optical powers of 2.5 mW were achieved using the hybrid AlGaAs-SOI micro-disk resonators, with plots of efficiency as a function of pump power demonstrating the reduction in TPA/FCA loss as expected from the AlGaAs resonators.

The achieved FWM efficiency was limited by both a large effective mode area and high dispersion from multi-mode propagation within the micro-disk resonators. Future research into producing higher FWM efficiencies would require switching to single-mode low dispersion AlGaAs resonators, as detailed in chapter 4, where efficiency levels are predicted to reach the gain regime under which optical parametric amplification can occur. The development of single-mode AlGaAs micro-ring resonators can be achieved by similar fabrication protocols as the Si membrane resonators, in which shallow-etched ridge resonators are fabricated into the core AlGaAs layer of the growth wafer. This would produce a transferable membrane containing AlGaAs micro-resonators which can be integrated within a fully processed SOI chip.

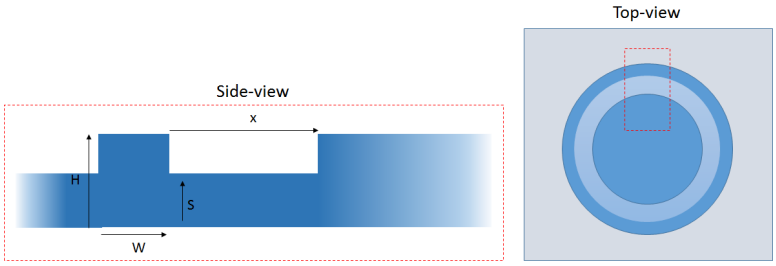

Figure 5.3: Side-view and top-view schematic illustrations of a proposed shallow-etch AlGaAs micro-ring resonator device.

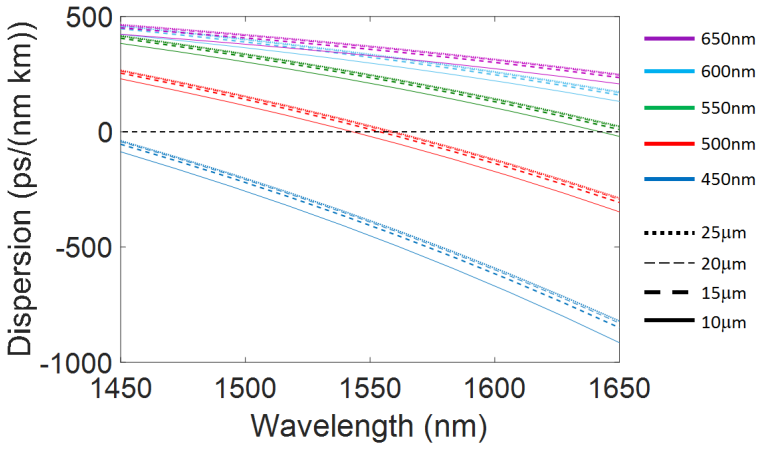

Figure 5.4: Dispersion analysis plot showing dispersion as a function of wavelength for varying waveguide widths (450 nm to 650 nm) and varying micro-resonator ROC (10 μm to 25 μm).

Figure 5.3 shows a schematic of the single-mode AlGaAs suspended membrane resonator device, detailing the cross-section of the shallow-etch region as well as a top-view of the membrane structure. The dispersion analysis for this resonator geometry is plotted in figure 5.4, for an AlGaAs shallow-etched resonator with a width w of 500 nm. The modal dispersion curves intersect the zero dispersion line around 1550 nm over a range of ROC between 10 μm and 25 μm. By setting a gap x between the waveguide and support region of $\sim$1 μm and a slab height S of $\sim$100 nm for an overall height of 230 nm, mode leakage into the support region can be reduced for minimal losses. The simulation also shows ROCs possible at 10 μm to

25 μm for extremely compact devices.

The final possible future project is the TP of ultra-high Q-factor silica micro-disks and toroid resonators into PIC systems. Among WGM resonator designs, silica microtoroids have exhibited some of the highest Q-factors to date as a result of their extremely low optical losses from visible all the way to near-IR making them very suitable for nonlinear applications [127], together with silica's biocompatible nature, they have high demand within biodetection experiments [103]. However, an issue is the standard optical injection method which uses tapered fibres to couple these devices to the outside world, which results in unstable experimental conditions. The use of TP can integrate free-standing silica micro-resonators within a pre-processed SOI substrate, substantially increasing the application range. SEM images of a silica micro-disk suspended on top of a silicon plinth are shown in figure 5.5, in order to integrate with non-native platforms requires the successful release of the micro-disk from the plinth.

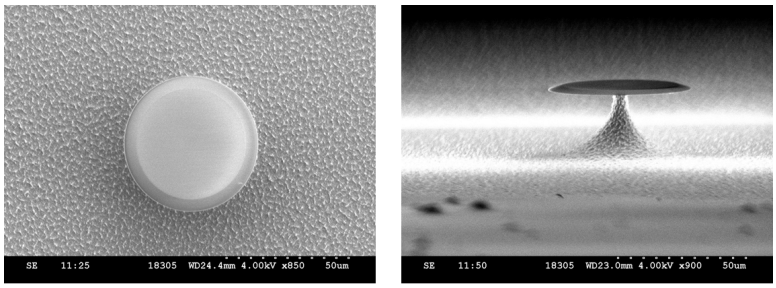

(a) (b)

Figure 5.5: (a) Top-view SEM image of silica micro-disk within native substrate. (b) Side-view image of micro-disk detailing the attached silicon plinth region produced during an under-etch of the structure.

We have shown the ability to TP these devices from their native substrate to a receiver chip, demonstrated by a silica microtoroid resonator bonded to a raised resist plinth on the receiver substrate, figure 5.6b. In order to release from the native

substrate, the silicon suspension pillar is broken by a quick retraction of the stamp. However, this process leaves remnants of the silicon plinth attached to the underside of the micro-disk. This issue can be overcome by a technique known as flip chip transfer printing. This process utilised the transfer of a device, mid-printing, to a second stamp which enables the bonding of the device to the receiver top-side down. A schematic of the flip chip TP method alongside a micro-disk bonded to a receiver chip using the explained procedure are both shown in figure 5.6.

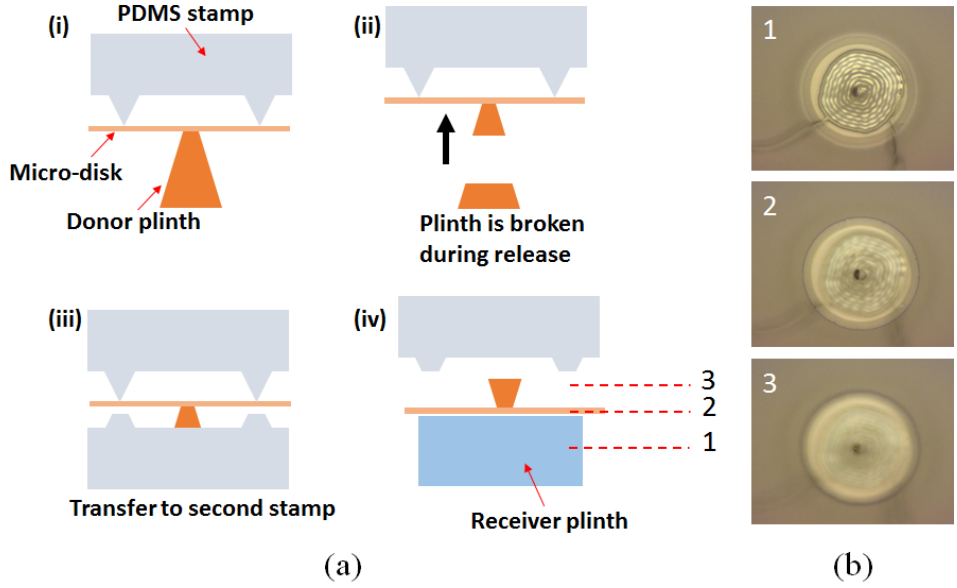

Figure 5.6: (a) Schematic of flip chip TP procedure of a micro-disk from a donor to receiver chip. (i) PDMS stamp is brought into contact with micro-disk (ii) Quick retraction causes underlying plinth to break, releasing micro-disk (iii) The micro-disk is transferred to a second PDMS stamp (flipping of device) (iv) Micro-disk is bonded to receiver chip with silicon plinth defect situated at top-side of micro-disk. (b) Optical images of silica micro-disk bonded to receiver, with images spanning multiple z-foci (1) Interface between resonator and second plinth situated on donor (2) Edge region of micro-disk device (3) Silicon plinth attached to micro-disk during release from donor chip.

5.4 Future direction of thesis research

The previous sections detail possible future work specific to each chapter's main motivation and research outcomes. However, the combination of the developed techniques and research can provide a collective future goal with regards to the overall vision of the thesis.

The main motivation is the integration of a complex PIC requiring many different material platforms in order to provide a host of unique optical properties. One example would be a tunable low-loss optical quantum circuit, demonstrating the on-chip generation and efficient routing of quantum-correlated photon pairs for quantum information processing [128] and sensing applications [129]. The introduction of single-photon quantum emitters as elements within PICs can enable significant scaling of quantum information processing (QIP) systems. This is only further complemented through the increased optical interactions experienced by the compact guiding components, as well as the investigation of many different physical processes available to chip-based nanophotonic structures such as Kerr and single-photon nonlinearities [130]. Until recently this would have required table-top systems, however it has since been demonstrated at the chip-scale, marking the potential of future quantum technology systems [131]. By utilising the advantages of the newly developed nanoscale accuracy TP method, the integration of multiple material devices in an extremely compact and parallel fashion can be used to produce an array of multi-λ tunable laser sources at increasingly high bandwidths, which when integrated with high $\chi^{(2)}$ sections can herald a spontaneous parametric down conversion (SPDC) single-photon source through the production of photon pairs. Following this, the addition of optical filtering systems and actively tunable and WDM components improves on function-

ality through the realisation of tunable routing of the quantum sources. This highly parallel and compact integration of the multiple material platform and devices would benefit from the flexibility of the TP method.

Overall, the thesis has helped provide possible solutions and technology required in order to produce large-scale PIC technologies. The additional flexibility of the high accuracy TP method exhibited opens up a wide range of possible research directions with an increased scope of future applications.

Appendix A

Transfer Printing of NW lasers

The work in this appendix involves the research into the high accuracy manipulation of NWs by the transfer printing method. First, the integration of NW lasers to a mechanically flexible waveguide system is detailed, with information into the device development and including analysis into the effects of the device lasing as a function of mechanical deformations of the waveguides. Following this, the analysis into the large-scale selection and manipulation of NWs based upon unique optical properties is provided. This section is a continuation of the work in chapter 2, providing further information on the characterisation and statistical analysis of the NWs prior to and after transfer printing.

A.1 Integration of NW lasers with flexible polymeric waveguide devices

Nanowire lasers have been integrated with mechanically flexible waveguide devices by high positional accuracy TP. The direct NW-waveguide coupling is achieved, both by end-fire coupling into the waveguide facet and with the NW laser printed directly on top of the waveguide. This section details the integration of NWs to waveguides fabricated onto mechanical substrates demonstrating robust coupling between the on-

chip laser source and deformed waveguiding structures. The author's contribution to this section is the fabrication of the flexible polymer SU-8 waveguide substrate and the deformation analysis.

A.1.1 Device fabrication and measurement

The polymer waveguides are fabricated using a standard direct-write laser lithography method. SU-8 photoresist is spincoated onto a flexible glass substrate (∼30 μm thick) with a film thickness of ≈4 μm. Following this, the custom-built maskless photolithography system, with λ=370 nm was used to expose the waveguide patterns which were then developed with an EC-solvent solution. The waveguides are multimode with diameters of 7 μm. The waveguide end facets were cleaved using a diamond scribe on one edge of the sample, with the other end used for NW integration. Propagation losses of the single-mode TE_{00} waveguides were measured at 3 dB/cm at the telecom band (∼1550 nm).

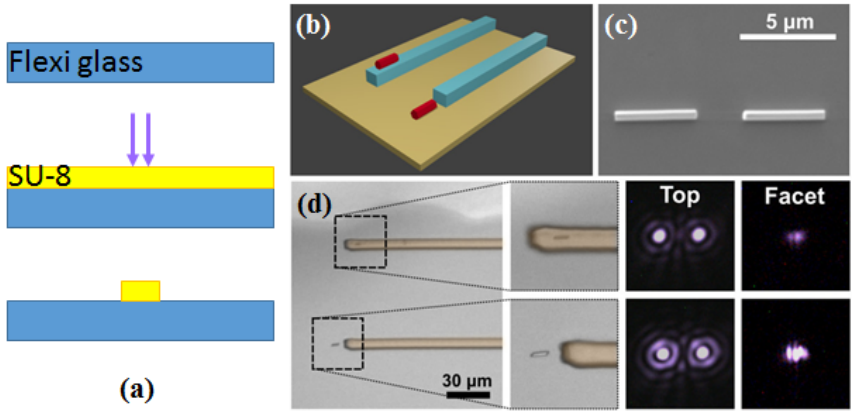

Figure A.1: (a) Schematic illustration of the SU-8 waveguide fabrication process. (b) Schematic of NW lasers integrated to waveguides; (c) SEM of NW lasers transfer printed with highly controlled positional alignment, measured at 50±35 nm; (d) Images of integrated devices and accompanying laser emission from NWs directly (left) and from waveguide end-facets.

NWs are transfer printed using techniques established in [88] with NWs directly

printed onto the top surface of the waveguide/substrate and aligned to the normal of the waveguide. The NW rotation is mechanically controlled by lateral stamp movements in order to rotationally align with the waveguides for maximum optical coupling. The images of lasing are obtained through μ-photoluminescence (μ-PL) with the optical excitation achieved by using a frequency-doubled Nd:YAG laser operating at 532 nm, measured at an optical pump power of 6.95 μW. Two CMOS cameras were used to capture the output lasing micrographs, one above the NW labelled as the vertical setup (VS), and one at the end-facet of the flexible substrate labelled as the edge detection module (EDM) with subsequent spectral data measured by a high resolution spectrometer. The integrated devices and examples of the lasing outputs are shown in figure A.1 with the experimental setup detailed in figure A.2.

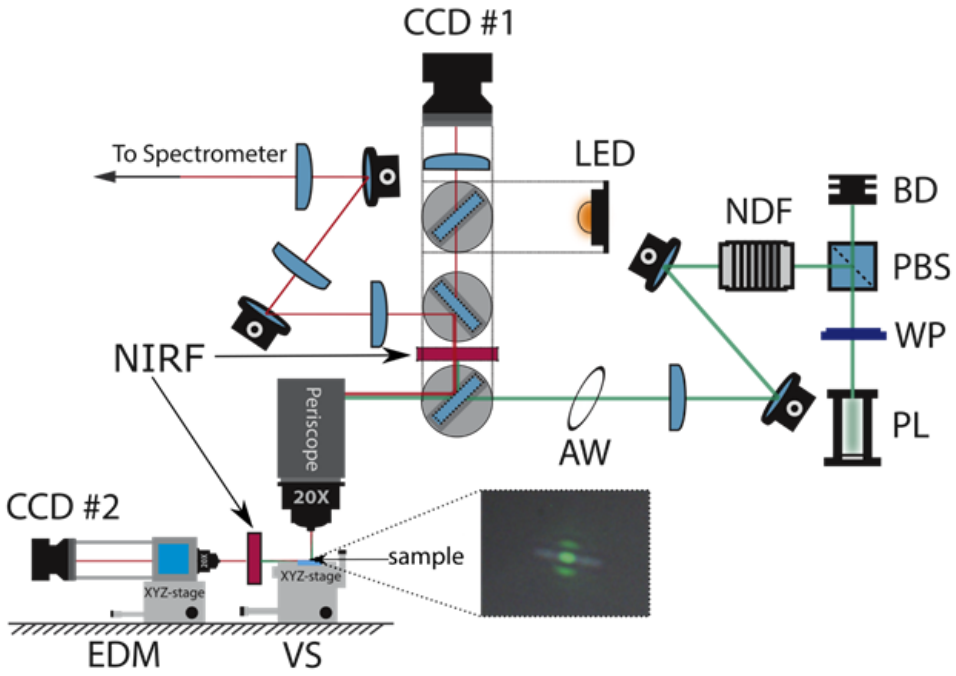

Figure A.2: Schematic diagram of the μ-PL setup for the characterisation of NW lasers, with and without the mechanical deformation applied. Setup includes the vertical Setup (VS) and Edge Detection Modules (EDM). PL pump laser; WP waveplate; PBS polarised beam splitter; BD beam dump; NDF neutral density filter; AW attenuator wheel; and NIRF near infrared filter.

A.1.2 Mechanical waveguide deformation and analysis

The characterisation of lasing properties of the integrated devices are measured as a function of mechanical deformation through the implementation of a bending module. A controlled curve was applied to the flexible substrate with both the top-view and end-facet lasing measured across a span of different substrate ROCs, as depicted in figure A.3.

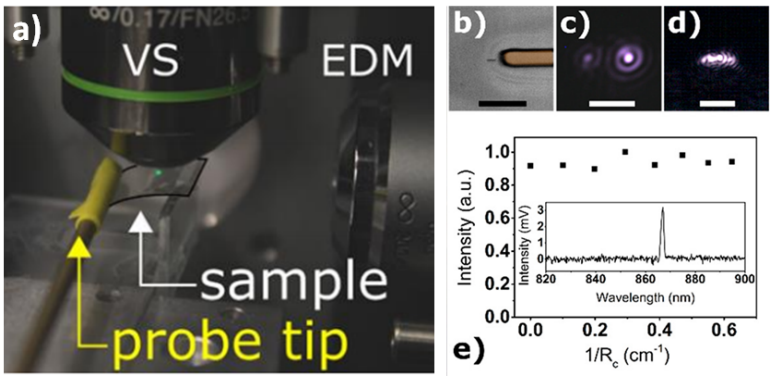

Figure A.3: (a) Image of mechanically deformed substrate detailing vertical and lateral imaging setup and probe tip used for sample deformation. (b) Top-view image of NW coarsely aligned to waveguide facet. (c) Top-view lasing emission of NW. (d) Emission from end-facet of waveguide showin multi-mode light propagation. (e) Normalized light intensity at the waveguide facet as a function of 1/ROC. Inset shows captured spectral emission of the NW at 1.6 cm ROC. Scalebars are 15 μm.

Figure A.3a demonstrates the sample deforming achieved using a mechanical probe tip assembly, as well as the NW investigation method by top-view imaging. The flexible waveguide sample was mounted with the waveguide end-facet overhanging the edge of a pillar region and fixed in position. The free end of the flexible glass was deflected in the vertical direction, this is subsequently converted to an equivalent radius of curvature assuming a constant bend radius of the flexible substrate. The measurement procedure of the waveguide's conformal ROC is previously detailed in chapter 3 by equation 3.2. Figure A.3e shows the relationship between the substrate bending and the normalised output power of the waveguide coupled to the NW laser. The pump laser was optimised for each measurement point by alignment of the objective to the NW, compensating for the vertical misalignment of the pump focus directly related to the vertical displacement with regards to substrate deflection. The plot depicts a minimum variation in the pump power of $\sim$5 % down to a ROC of 1.6 cm, limited by the mechanical fracture of the substrate after reading its maximum flex capability. The results shows the integration of NWs to passive

waveguide components, with the ability to produce flexible passive structures robust to mechanical deformations with the outlined work describe in full detail in [73].

A.2 Large-scale selective manipulation and high accuracy alignment of NW lasers

This section follows the work described in chapter 2 looking at the characterisation and statistical analysis of a large number of NW lasers across a sample substrate, followed by their selection based on unique properties and high accuracy alignment and integration to a second receiver substrate. The technique and alignment protocol are detailed in the chapter, with this section containing the binned NW arrays and their specific properties. Further to this, the output analysis of their photoluminescence and lasing characteristics before and after the TP procedure.

A.2.1 NW arrays

Figure A.4 contains top-view μ-PL images of the NW array detailed in chapter 2, with images captured before and after TP to the receiver substrate. The NWs in question are multi-mode such that the NW excitation changes based upon which area is exposed to the beam. The PL spectra shows a clear overlap in the PL output. This overlap is shown again for the lasing spectroscopy, however the multi-mode condition has caused slight variations in the mode wavelengths. Overall, the overlap between the newly characterised and original NW data show clearly that the selected devices are the initially chosen NW lasers demonstrating the success of the procedure.

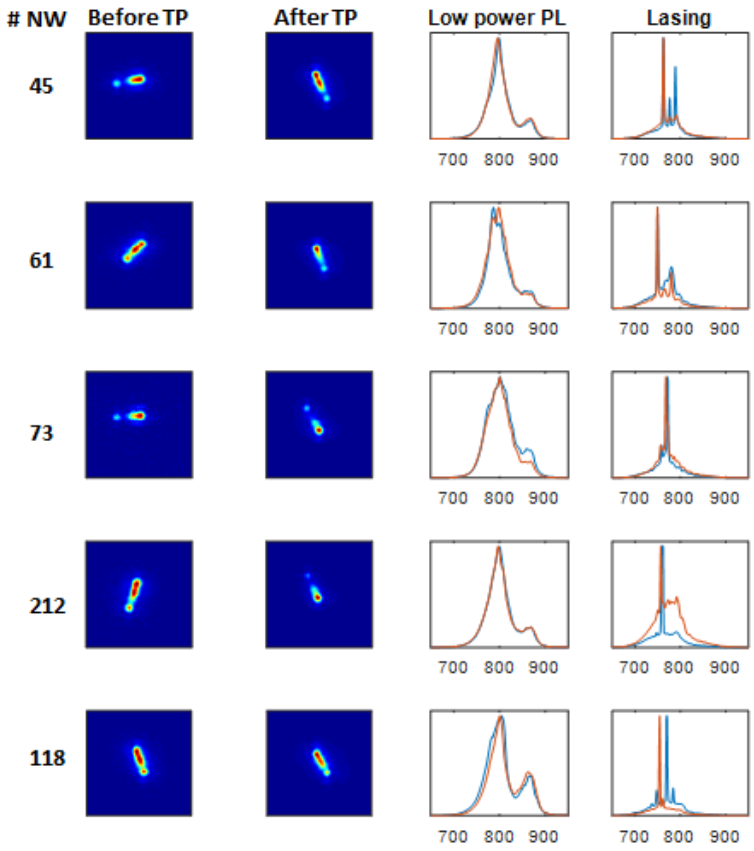

Figure A.4: Characterisation of NW laser array showing before and after data of selected NWs with (left) top-view PL images of NWs; (middle) PL spectra; (right) lasing spectra.

The same procedure was achieved for five NW arrays, each array containing NWs with specific μ-PL and lasing properties. 24 of the 25 TP NWs lased post-TP, the failure of the final NW could be due to anything from the TP process, to degradation of the NW over time. The before and after lasing wavelength plot in figure A.5b shows a clear correlation with regards to the lasing conditions of the NWs. This is continued in the lasing threshold correlation plot, with the clear bundling of each arrays NWs based upon their array specific lasing threshold conditions demonstrated. Several outliers are detailed in the final plot which could be due to fluctuations in the thresholding value caused by the NW multi-mode nature, with the variation not demonstrated in the PL wavelength spectra.

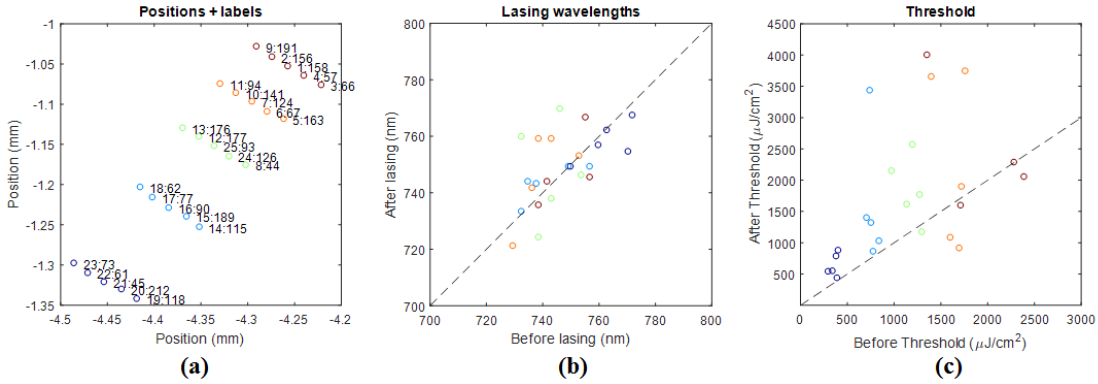

Figure A.5: (a) Plot detailing the relative positions for each array of five NW lasers on the receiver substrate. (b) Correlated plot of lasing wavelengths before and after TP. (c) Correlated plot of lasing threshold before and after TP.

Appendix B

Transfer Printing of polymer waveguides on flexible substrates

The thesis work demonstrated the vertical assembly of waveguiding layers by nanoscale accuracy TP. The flexibility of the technique is further shown by the following work, detailing the vertical coupling of polyermic waveguide layers through the TP of mm-scale flexible glass substrates. This section details the technique enabling fabrication of polymer waveguides on flexible glass substrates by direct-write laser lithography, followed by the TP method enabling the vertical coupling of polymer components.

B.1 Polymer waveguide design and fabrication

A mode solver was used in order to simulate the geometric cross-section requires for the production of TE single-mode SU-8 polymer waveguide structures. This was achieved using a MatLab function with the results shown in figure B.1 at a wavelength of 1550nm, calculating the modes using a semivectorial finite difference method with a full description of the technique provided by [132]. The structures are made up of an SU-8 polymer waveguide of refractive index 1.55, and a cladding of SiO_2 with index 1.52. The simulations determine a single-mode propagation occuring for SU-8 waveguides with a height of 4 μm and a diameter of 2.5 μm.

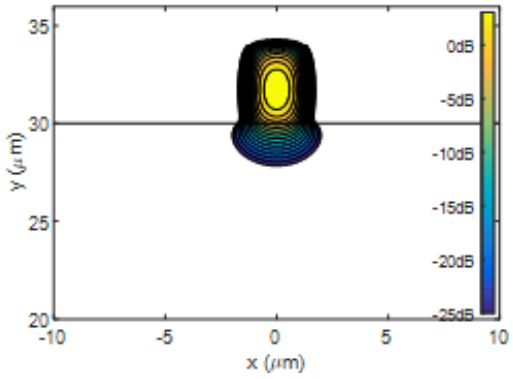

Figure B.1: Mode simulation of the fundamental TE_{00} mode for a 2.6×4 μm polymer (SU-8) waveguide.

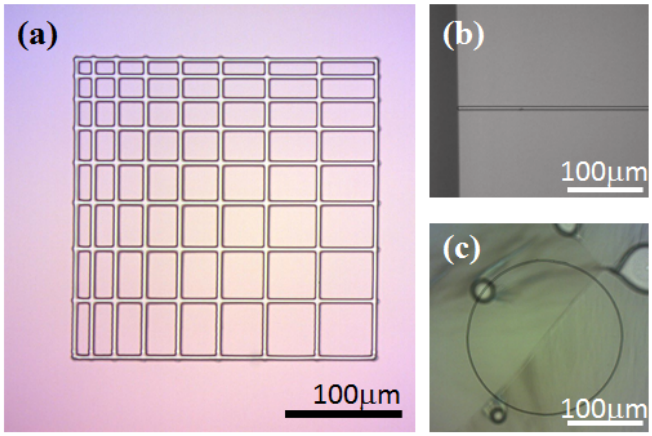

Figure B.2: (a) Optical micrograph of tapered grid alignment mark fabricated using direct-write laser lithography. (b) Straight waveguide on receiver glass substrate showing cleaved edge of sample. (c) Ring resonator fabricated on flexible substrate.

All components follow the same fabrication procedure as the polymer waveguides within appendix A. The donor substrate containing the polymer bus waveguides is composed of an ultra-thin flexible SiO_2 substrate of ~30 μm thickness for conformal bonding, whilst the receiver SiO_2 substrate is 280 μm in order to produce a more rigid final device platform. The individual waveguide devices situated on each substrate as well as a fabricated alignment marker are shown in figure B.2, with identical alignment markers situated on each substrate.

B.2 Transfer printing procedure

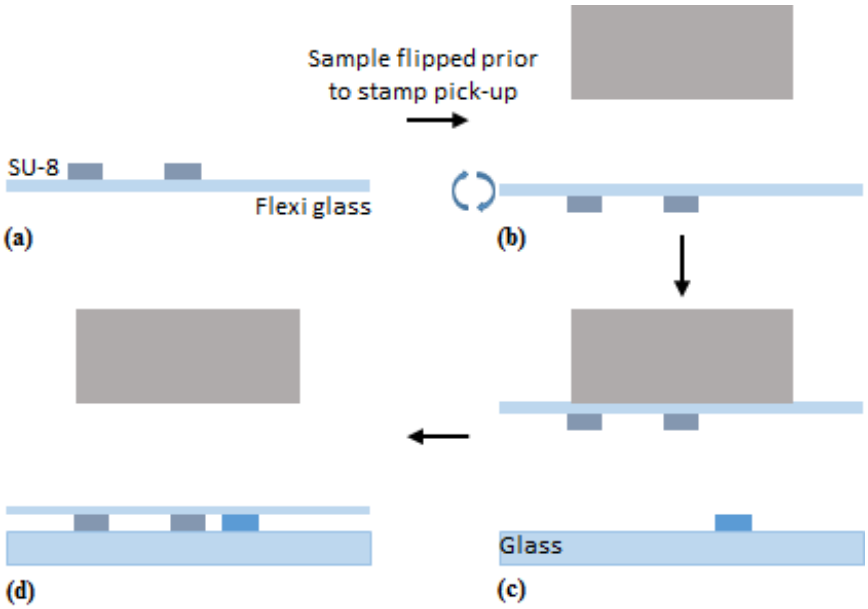

Figure B.3: Schematic of TP process showing transfer printing of flexible glass containing polymer structures; (a) flexible glass with SU-8 polymer structures; (b)-(c) sample if flipped prior to printing with PDMS stamp used to pick-up sample from TP system sample holder; (d) Flipped sample is bonded to glass substrate as to integrated the patterned structures.

The first stage in the TP method requires the flipping of the donor flexible substrate, ensuring direct contact between the non-native waveguide devices producing an MMI coupler system, as illustrated in figure B.3b. The sample is flipped before being placed free-standing onto the sample holder in the TP system, the size and weight of the sample limits slippage during the translation stage displacement for high accuracy positional alignment. The ultra-thin glass allows viewing of the structures through the substrate by the optical imaging system, necessary as a means to capture images of the alignment markers during the alignment procedure. The cross-correlation alignment protocol, as discussed in chapter 2, is utilised. Once the chip-to-chip alignment is achieved, the flexible substrate is picked-up using the PDMS stamp. A

large stamp contact area is required to improve adhesion for controlled manipulation of the mm-scale flexible device. An IPA solvent layer is deposited onto the receiver prior to contact. The two substrates are placed into contact, with the capillary force of the solvent pulling the IPA away from the substrate interface leaving a strong bond between the two surfaces.

B.3 Vertically assembled devices and characterisation

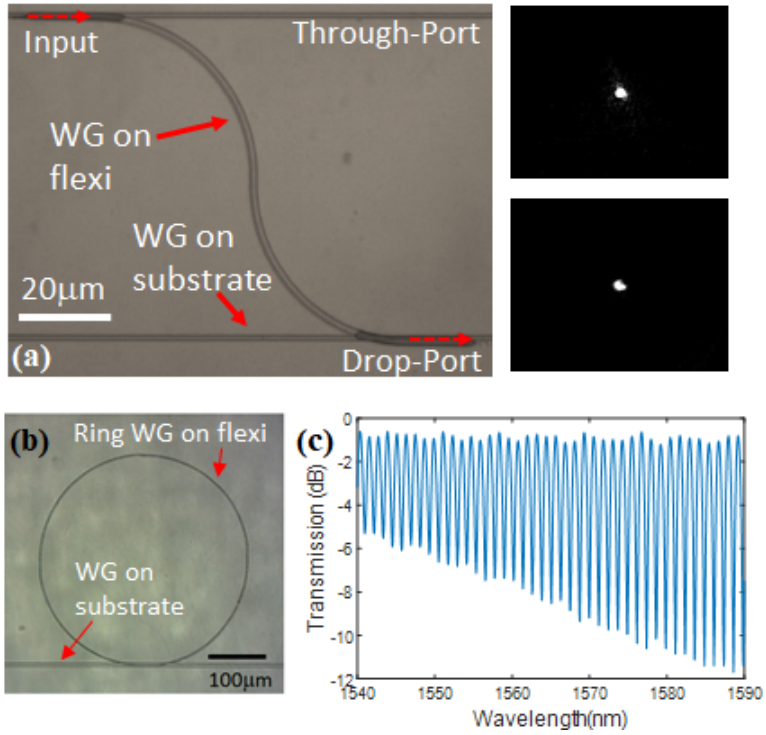

Figure B.4: Optical micrographs of vertically assembled polymer waveguide structures showing (a) coupler region and accompanying facet outputs for drop-port and drop-port waveguides; (b) transfer printed all-pass ring resonator and associated singe-mode transmission spectra.

Figure B.4a shows the finished vertically assembled waveguide coupler. Both straight input and drop-port waveguide structures are situated on the receiver substrate, whilst the s-bend coupler is on the transferred flexible SiO_2 substrate. The coupler

regions are aligned using the cross-correlation alignment TP method, and bonded directly by capillary forces. Light is injected into the input waveguide on the receiver substrate using an end-fire transmission rig. A proportion of this light is then coupled to the drop-port through the coupler region, with both output modes shown in the relevant images captured by an IR camera situated in focus at the output of the receiver substrate. The average coupling percentage of light at the drop-port waveguide output is measured as 7.9±1.3 % across a wavelength range of 1520-1600 nm, detailing a high level of coupling achieved.

Figure B.4b contains an optical micrograph of a micro-assembled all-pass ring resonator device produced by high alignment TP. The micro-ring cavity is situated on a transferred flexible substrate and is aligned to a straight bus waveguide situated on the receiver SiO_2 substrate, promoting coupling into the resonator. A normalised transmission spectra in figure B.4c shows a high extinction single-mode resonance produced from the all-pass polymer resonator. All results are produced by resonators with a ROC of 100 μm to minimise bend losses, causing a very narrow FSR. For these type of micro-assembled polymer micro-ring resonators, using transmission fitting of the resonances we have calculated Q-factors up tp ∼7000, with losses per round-trip of ∼1 dB. However, high system losses can be attributed to large optical scattering situated at the coupling regions and the interface between each substrate, with distributed losses ranging from ∼6 dB/cm to ∼25 dB/cm.

Bibliography

[1] R. Dangel, J. Hofrichter, F. Horst, D. Jubin, A. L. Porta, N. Meier, I. M. Soganci, J. Weiss, and B. J. Offrein, "Polymer waveguides for electro-optical integration in data centers and high-performance computers," *Optics Express*, vol. 23, no. 4, p. 4736, Feb. 2015. [Online]. Available: https://doi.org/10.1364/oe.23.004736

[2] Z. Wang, B. Tian, M. Pantouvaki, W. Guo, P. Absil, J. V. Campenhout, C. Merckling, and D. V. Thourhout, "Room-temperature InP distributed feedback laser array directly grown on silicon," *Nature Photonics*, vol. 9, no. 12, pp. 837–842, oct 2015. [Online]. Available: https://doi.org/10.1038/nphoton.2015.199

[3] A. Trindade, *Transfer printing of nitride based light emitting diodes*. University of Strathclyde, Glasgow, 2015. [Online]. Available: http://oleg.lib.strath.ac.uk/R/?func=dbin-jump-full&object_id=25449

[4] S. Kim, J. Wu, A. Carlson, S. H. Jin, A. Kovalsky, P. Glass, Z. Liu, N. Ahmed, S. L. Elgan, W. Chen, P. M. Ferreira, M. Sitti, Y. Huang, and J. A. Rogers, "Microstructured elastomeric surfaces with reversible adhesion and examples of their use in deterministic assembly by transfer printing," *Proceedings of the*

National Academy of Sciences, vol. 107, no. 40, pp. 17 095–17 100, sep 2010. [Online]. Available: https://doi.org/10.1073/pnas.1005828107

[5] X. Cai, M. Strain, S. Yu, and M. Sorel, "Photonic integrated devices for exploiting the orbital angular momentum of light in optical communications," *Frontiers of Optoelectronics*, vol. 9, no. 3, pp. 518–525, Sep. 2016. [Online]. Available: https://doi.org/10.1007/s12200-016-0572-9

[6] S. Koehl, A. Liu, and M. Paniccia, "Integrated silicon photonics: Harnessing the data explosion," *Optics and Photonics News*, vol. 22, no. 3, p. 24, mar 2011. [Online]. Available: https://doi.org/10.1364/opn.22.3.000024

[7] D. Miller, "Rationale and challenges for optical interconnects to electronic chips," *Proceedings of the IEEE*, vol. 88, no. 6, pp. 728–749, jun 2000. [Online]. Available: https://doi.org/10.1109/5.867687

[8] A. F. Benner, M. Ignatowski, J. A. Kash, D. M. Kuchta, and M. B. Ritter, "Exploitation of optical interconnects in future server architectures," *IBM Journal of Research and Development*, vol. 49, no. 4.5, pp. 755–775, Jul. 2005. [Online]. Available: https://doi.org/10.1147/rd.494.0755

[9] A. Shacham, K. Bergman, and L. P. Carloni, "Photonic networks-on-chip for future generations of chip multiprocessors," *IEEE Transactions on Computers*, vol. 57, no. 9, pp. 1246–1260, Sep. 2008. [Online]. Available: https://doi.org/10.1109/tc.2008.78

[10] D. Miller, "Device requirements for optical interconnects to silicon chips," *Proceedings of the IEEE*, vol. 97, no. 7, pp. 1166–1185, Jul. 2009. [Online]. Available: https://doi.org/10.1109/jproc.2009.2014298

[11] D. Welch, F. Kish, S. Melle, R. Nagarajan, M. Kato, C. Joyner, J. Pleumeekers, R. Schneider, J. Back, A. Dentai, V. Dominic, P. Evans, M. Kauffman, D. Lambert, S. Hurtt, A. Mathur, M. Mitchell, M. Missey, S. Murthy, A. Nilsson, R. Salvatore, M. V. Leeuwen, J. Webjorn, M. Ziari, S. Grubb, D. Perkins, M. Reffle, and D. Mehuys, "Large-scale InP photonic integrated circuits: Enabling efficient scaling of optical transport networks," *IEEE Journal of Selected Topics in Quantum Electronics*, vol. 13, no. 1, pp. 22–31, 2007. [Online]. Available: https://doi.org/10.1109/jstqe.2006.890068

[12] P. Dong, "Silicon photonic integrated circuits for wavelength-division multiplexing applications," *IEEE Journal of Selected Topics in Quantum Electronics*, vol. 22, no. 6, pp. 370–378, nov 2016. [Online]. Available: https://doi.org/10.1109/jstqe.2016.2575358

[13] C. Doerr, L. Chen, D. Vermeulen, T. Nielsen, S. Azemati, S. Stulz, G. McBrien, X.-M. Xu, B. Mikkelsen, M. Givehchi, C. Rasmussen, and S.-Y. Park, "Single-chip silicon photonics 100-gb/s coherent transceiver," in *Optical Fiber Communication Conference: Postdeadline Papers*. OSA, 2014. [Online]. Available: https://doi.org/10.1364/ofc.2014.th5c.1

[14] L. Virot, P. Crozat, J.-M. Fédéli, J.-M. Hartmann, D. Marris-Morini, E. Cassan, F. Boeuf, and L. Vivien, "Germanium avalanche receiver for low power interconnects," *Nature Communications*, vol. 5, no. 1, sep 2014. [Online]. Available: https://doi.org/10.1038/ncomms5957

[15] C. Sun, M. T. Wade, Y. Lee, J. S. Orcutt, L. Alloatti, M. S. Georgas, A. S. Waterman, J. M. Shainline, R. R. Avizienis, S. Lin, B. R. Moss, R. Kumar, F. Pavanello, A. H. Atabaki, H. M. Cook, A. J. Ou, J. C.

Leu, Y.-H. Chen, K. Asanović, R. J. Ram, M. A. Popović, and V. M. Stojanović, "Single-chip microprocessor that communicates directly using light," *Nature*, vol. 528, no. 7583, pp. 534–538, dec 2015. [Online]. Available: https://doi.org/10.1038/nature16454

[16] C. Delezoide, M. Salsac, J. Lautru, H. Leh, C. Nogues, J. Zyss, M. Buckle, I. Ledoux-Rak, and C. T. Nguyen, "Vertically coupled polymer microracetrack resonators for label-free biochemical sensors," *IEEE Photonics Technology Letters*, vol. 24, no. 4, pp. 270–272, feb 2012. [Online]. Available: https://doi.org/10.1109/lpt.2011.2177518

[17] K. D. Vos, J. Girones, T. Claes, Y. D. Koninck, S. Popelka, E. Schacht, R. Baets, and P. Bienstman, "Multiplexed antibody detection with an array of silicon-on-insulator microring resonators," *IEEE Photonics Journal*, vol. 1, no. 4, pp. 225–235, oct 2009. [Online]. Available: https://doi.org/10.1109/jphot.2009.2035433

[18] Y. Arakawa, T. Nakamura, Y. Urino, and T. Fujita, "Silicon photonics for next generation system integration platform," *IEEE Communications Magazine*, vol. 51, no. 3, pp. 72–77, mar 2013. [Online]. Available: https://doi.org/10.1109/mcom.2013.6476868

[19] V. Lal, J. Summers, N. Kim, S. W. Corzine, P. Evans, M. Lauermann, A. Nguyen, A. Hosseini, M. Lu, J. T. Rahn, M. R. Chitgarha, J. Zhang, J. Osenbach, T. Vallaitis, P. Samra, C. Park, M. Kuntz, J. Tang, C. Tsai, H. Sun, R. Schmogrow, D. Pavinski, B. Behnia, P. Mertz, T. Butrie, K.-T. Wu, M. Mitchell, M. Ziari, M. Reffle, D. Welch, and F. Kish, "Extended c-band tunable multi-channel inp-based coherent transmitter pics," *J. Lightwave*

Technol., vol. 35, no. 7, pp. 1320–1327, Apr 2017. [Online]. Available: http://jlt.osa.org/abstract.cfm?URI=jlt-35-7-1320

[20] M. Lipson, "Nonlinear silicon photonics," in *2011 Conference on Lasers and Electro-Optics Europe and 12th European Quantum Electronics Conference (CLEO EUROPE/EQEC)*. IEEE, may 2011. [Online]. Available: https://doi.org/10.1109/cleoe.2011.5943578

[21] J. Sun, E. Timurdogan, A. Yaacobi, Z. Su, E. S. Hosseini, D. B. Cole, and M. R. Watts, "Large-scale silicon photonic circuits for optical phased arrays," *IEEE Journal of Selected Topics in Quantum Electronics*, vol. 20, no. 4, pp. 264–278, jul 2014. [Online]. Available: https://doi.org/10.1109/jstqe.2013.2293316

[22] R. Nagarajan, P. Evans, M. Kato, M. Fisher, S. Corzine, A. Dentai, M. Missey, A. Spannagel, S. Nguyen, M. Raburn, M. Ziari, C. Joyner, F. Kish, and D. Welch, "Large-scale monolithically integrated photonic circuits for terabit/s data rate applications," in *2008 7th International Conference on Optical Internet*, Oct 2008, pp. 1–2.

[23] J. Doylend and A. Knights, "The evolution of silicon photonics as an enabling technology for optical interconnection," *Laser & Photonics Reviews*, vol. 6, no. 4, pp. 504–525, jan 2012. [Online]. Available: https://doi.org/10.1002/lpor.201100023

[24] D. Liang and J. E. Bowers, "Recent progress in lasers on silicon," *Nature Photonics*, vol. 4, no. 8, pp. 511–517, jul 2010. [Online]. Available: https://doi.org/10.1038/nphoton.2010.167

[25] A. W. Fang, B. Koch, E. Norberg, G. Fish, and E. Hall, "Heterogeneous integration as a manufacturing platform for photonic integrated circuits," in *2013 IEEE Photonics Conference*. IEEE, sep 2013. [Online]. Available: https://doi.org/10.1109/ipcon.2013.6656382

[26] Xingsheng Liu, S. Haque, Jinggang Wang, and Guo-Quan Lu, "Packaging of integrated power electronics modules using flip-chip technology," in *APEC 2000. Fifteenth Annual IEEE Applied Power Electronics Conference and Exposition (Cat. No.00CH37058)*, vol. 1, Feb 2000, pp. 290–296 vol.1.

[27] T. Shimizu, N. Hatori, M. Okano, M. Ishizaka, Y. Urino, T. Yamamoto, M. Mori, T. Nakamura, and Y. Arakawa, "Multichannel and high-density hybrid integrated light source with a laser diode array on a silicon optical waveguide platform for interchip optical interconnection," *Photonics Research*, vol. 2, no. 3, p. A19, apr 2014. [Online]. Available: https://doi.org/10.1364/prj.2.000a19

[28] H. Lu, J. S. Lee, Y. Zhao, C. Scarcella, P. Cardile, A. Daly, M. Ortsiefer, L. Carroll, and P. O'Brien, "Flip-chip integration of tilted VCSELs onto a silicon photonic integrated circuit," *Optics Express*, vol. 24, no. 15, p. 16258, jul 2016. [Online]. Available: https://doi.org/10.1364/oe.24.016258

[29] Z. Wang, B. Tian, M. Paladugu, M. Pantouvaki, N. L. Thomas, C. Merckling, W. Guo, J. Dekoster, J. V. Campenhout, P. Absil, and D. V. Thourhout, "Polytypic InP nanolaser monolithically integrated on (001) silicon," *Nano Letters*, vol. 13, no. 11, pp. 5063–5069, oct 2013. [Online]. Available: https://doi.org/10.1021/nl402145r

[30] B. Mayer, L. Janker, B. Loitsch, J. Treu, T. Kostenbader, S. Lichtmannecker, T. Reichert, S. Morkötter, M. Kaniber, G. Abstreiter, C. Gies, G. Koblmüller, and J. J. Finley, "Monolithically integrated high-β nanowire lasers on silicon," *Nano Letters*, vol. 16, no. 1, pp. 152–156, dec 2015. [Online]. Available: https://doi.org/10.1021/acs.nanolett.5b03404

[31] D. Liang, A. W. Fang, H. Park, T. E. Reynolds, K. Warner, D. C. Oakley, and J. E. Bowers, "Low-temperature, strong sio2-sio2 covalent wafer bonding for iii–v compound semiconductors-to-silicon photonic integrated circuits," *Journal of Electronic Materials*, vol. 37, no. 10, pp. 1552–1559, Oct 2008. [Online]. Available: https://doi.org/10.1007/s11664-008-0489-1

[32] S. Keyvaninia, M. Muneeb, S. Stanković, P. J. V. Veldhoven, D. V. Thourhout, and G. Roelkens, "Ultra-thin DVS-BCB adhesive bonding of III-v wafers, dies and multiple dies to a patterned silicon-on-insulator substrate," *Optical Materials Express*, vol. 3, no. 1, p. 35, dec 2012. [Online]. Available: https://doi.org/10.1364/ome.3.000035

[33] J. Wei, H. Xie, M. L. Nai, C. K. Wong, and L. C. Lee, "Low temperature wafer anodic bonding," *Journal of Micromechanics and Microengineering*, vol. 13, no. 2, pp. 217–222, jan 2003. [Online]. Available: https://doi.org/10.1088%2F0960-1317%2F13%2F2%2F308

[34] H. C. Lin, K. L. Chang, K. C. Hsieh, K. Y. Cheng, and W. H. Wang, "Metallic wafer bonding for the fabrication of long-wavelength vertical-cavity surface-emitting lasers," *Journal of Applied Physics*, vol. 92, no. 7, pp. 4132–4134, oct 2002. [Online]. Available: https://doi.org/10.1063/1.1502200

[35] G. Crosnier, D. Sanchez, S. Bouchoule, P. Monnier, G. Beaudoin, I. Sagnes, R. Raj, and F. Raineri, "Hybrid indium phosphide-on-silicon nanolaser diode," *Nature Photonics*, vol. 11, no. 5, pp. 297–300, apr 2017. [Online]. Available: https://doi.org/10.1038/nphoton.2017.56

[36] H. Park, Y. hao Kuo, A. W. Fang, R. Jones, O. Cohen, M. J. Paniccia, and J. E. Bowers, "A hybrid AlGaInAs-silicon evanescent preamplifier and photodetector," *Optics Express*, vol. 15, no. 21, p. 13539, 2007. [Online]. Available: https://doi.org/10.1364/oe.15.013539

[37] K. Chen, Q. Huang, J. Zhang, J. Cheng, X. Fu, C. Zhang, K. Ma, Y. Shi, D. V. Thourhout, G. Roelkens, L. Liu, and S. He, "Wavelength-multiplexed duplex transceiver based on III-v/si hybrid integration for off-chip and on-chip optical interconnects," *IEEE Photonics Journal*, vol. 8, no. 1, pp. 1–10, feb 2016. [Online]. Available: https://doi.org/10.1109/jphot.2016.2516903

[38] E. Menard, K. J. Lee, D.-Y. Khang, R. G. Nuzzo, and J. A. Rogers, "A printable form of silicon for high performance thin film transistors on plastic substrates," *Applied Physics Letters*, vol. 84, no. 26, pp. 5398–5400, jun 2004. [Online]. Available: https://doi.org/10.1063/1.1767591

[39] M. A. Meitl, Z.-T. Zhu, V. Kumar, K. J. Lee, X. Feng, Y. Y. Huang, I. Adesida, R. G. Nuzzo, and J. A. Rogers, "Transfer printing by kinetic control of adhesion to an elastomeric stamp," *Nature Materials*, vol. 5, no. 1, pp. 33–38, dec 2005. [Online]. Available: https://doi.org/10.1038/nmat1532

[40] H. Yang, D. Zhao, S. Chuwongin, J.-H. Seo, W. Yang, Y. Shuai, J. Berggren, M. Hammar, Z. Ma, and W. Zhou, "Transfer-printed stacked nanomembrane

lasers on silicon," *Nature Photonics*, vol. 6, no. 9, pp. 615–620, jul 2012. [Online]. Available: https://doi.org/10.1038/nphoton.2012.160

[41] A. J. Trindade, B. Guilhabert, D. Massoubre, D. Zhu, N. Laurand, E. Gu, I. M. Watson, C. J. Humphreys, and M. D. Dawson, "Nanoscale-accuracy transfer printing of ultra-thin AlInGaN light-emitting diodes onto mechanically flexible substrates," *Applied Physics Letters*, vol. 103, no. 25, p. 253302, dec 2013. [Online]. Available: https://doi.org/10.1063/1.4851875

[42] N. Ye, G. Muliuk, J. Zhang, A. Abbasi, A. J. Trindade, C. Bower, D. V. Thourhout, and G. Roelkens, "Transfer print integration of waveguide-coupled germanium photodiodes onto passive silicon photonic ICs," *Journal of Lightwave Technology*, vol. 36, no. 5, pp. 1249–1254, mar 2018. [Online]. Available: https://doi.org/10.1109/jlt.2017.2777509

[43] C. A. Bower, E. Menard, and P. E. Garrou, "Transfer printing: An approach for massively parallel assembly of microscale devices," in *2008 58th Electronic Components and Technology Conference*. IEEE, may 2008. [Online]. Available: https://doi.org/10.1109/ectc.2008.4550113

[44] C. A. Bower, E. Menard, S. Bonafede, J. W. Hamer, and R. S. Cok, "Transfer-printed microscale integrated circuits for high performance display backplanes," *IEEE Transactions on Components, Packaging and Manufacturing Technology*, vol. 1, no. 12, pp. 1916–1922, dec 2011. [Online]. Available: https://doi.org/10.1109/tcpmt.2011.2128324

[45] J. Yoon, S.-M. Lee, D. Kang, M. A. Meitl, C. A. Bower, and J. A. Rogers, "Heterogeneously integrated optoelectronic devices enabled by micro-transfer

printing," *Advanced Optical Materials*, vol. 3, no. 10, pp. 1313–1335, sep 2015. [Online]. Available: https://doi.org/10.1002/adom.201500365

[46] N. Ye, G. Muliuk, A. J. Trindade, C. Bower, J. Zhang, S. Uvin, D. V. Thourhout, and G. Roelkens, "High-alignment-accuracy transfer printing of passive silicon waveguide structures," *Optics Express*, vol. 26, no. 2, p. 2023, jan 2018. [Online]. Available: https://doi.org/10.1364/oe.26.002023

[47] P. L. Stiles, "Direct deposition of micro- and nanoscale hydrogels using dip pen nanolithography (DPN)," *Nature Methods*, vol. 7, no. 8, pp. i–ii, aug 2010. [Online]. Available: https://doi.org/10.1038/nmeth.f.309

[48] J.-W. Jang, A. Smetana, and P. Stiles, "Multi-ink pattern generation by dip-pen nanolithographyâ®," *Scanning*, pp. n/a–n/a, 2010. [Online]. Available: https://doi.org/10.1002/sca.20163

[49] Y. Wang, D. Maspoch, S. Zou, G. C. Schatz, R. E. Smalley, and C. A. Mirkin, "Controlling the shape, orientation, and linkage of carbon nanotube features with nano affinity templates," *Proceedings of the National Academy of Sciences*, vol. 103, no. 7, pp. 2026–2031, feb 2006. [Online]. Available: https://doi.org/10.1073/pnas.0511022103

[50] Y. Y. Huang, W. Zhou, K. J. Hsia, E. Menard, J.-U. Park, J. A. Rogers, and A. G. Alleyne, "Stamp collapse in soft lithography," *Langmuir*, vol. 21, no. 17, pp. 8058–8068, Aug. 2005. [Online]. Available: https://doi.org/10.1021/la0502185

[51] W. J. Westerveld, S. M. Leinders, K. W. A. van Dongen, H. P. Urbach, and M. Yousefi, "Extension of marcatilis analytical approach for rectangular silicon

optical waveguides," *Journal of Lightwave Technology*, vol. 30, no. 14, pp. 2388–2401, Jul. 2012. [Online]. Available: https://doi.org/10.1109/jlt.2012.2199464

[52] E. A. J. Marcatili, "Dielectric rectangular waveguide and directional coupler for integrated optics," *Bell System Technical Journal*, vol. 48, no. 7, pp. 2071–2102, Sep. 1969. [Online]. Available: https://doi.org/10.1002/j.1538-7305.1969.tb01166.x

[53] C. R. Doerr, L. L. Buhl, Y. Baeyens, R. Aroca, S. Chandrasekhar, X. Liu, L. Chen, and Y.-K. Chen, "Packaged monolithic silicon 112-gb/s coherent receiver," *IEEE Photonics Technology Letters*, vol. 23, no. 12, pp. 762–764, Jun. 2011. [Online]. Available: https://doi.org/10.1109/lpt.2011.2132699

[54] T. Pfau, R. Peveling, J. Hauden, N. Grossard, H. Porte, Y. Achiam, S. Hoffmann, S. K. Ibrahim, O. Adamczyk, S. Bhandare, D. Sandel, M. Porrmann, and R. Noe, "Coherent digital polarization diversity receiver for real-time polarization-multiplexed QPSK transmission at 2.8 gb/s," *IEEE Photonics Technology Letters*, vol. 19, no. 24, pp. 1988–1990, Dec. 2007. [Online]. Available: https://doi.org/10.1109/lpt.2007.909897

[55] H. Huang, K. Liu, B. Qi, and V. J. Sorger, "Re-analysis of single-mode conditions for silicon rib waveguides at 1550 nm wavelength," *Journal of Lightwave Technology*, vol. 34, no. 16, pp. 3811–3817, aug 2016. [Online]. Available: https://doi.org/10.1109/jlt.2016.2579163

[56] L. Li, Y. Zou, H. Lin, J. Hu, X. Sun, N.-N. Feng, S. Danto, K. Richardson, T. Gu, and M. Haney, "A fully-integrated flexible photonic platform for chip-to-chip optical interconnects," *Journal of Lightwave*

Technology, vol. 31, no. 24, pp. 4080–4086, dec 2013. [Online]. Available: https://doi.org/10.1109/jlt.2013.2285382

[57] A. W. Poon, X. Luo, F. Xu, and H. Chen, "Cascaded microresonator-based matrix switch for silicon on-chip optical interconnection," *Proceedings of the IEEE*, vol. 97, no. 7, pp. 1216–1238, Jul. 2009. [Online]. Available: https://doi.org/10.1109/jproc.2009.2014884

[58] M. Baaske and F. Vollmer, "Optical resonator biosensors: Molecular diagnostic and nanoparticle detection on an integrated platform," *ChemPhysChem*, vol. 13, no. 2, pp. 427–436, Dec. 2011. [Online]. Available: https://doi.org/10.1002/cphc.201100757

[59] M. Pu, H. Hu, L. Ottaviano, E. Semenova, D. Vukovic, L. K. Oxenløwe, and K. Yvind, "Ultra-efficient and broadband nonlinear AlGaAs-on-insulator chip for low-power optical signal processing," *Laser & Photonics Reviews*, vol. 12, no. 12, p. 1800111, oct 2018. [Online]. Available: https://doi.org/10.1002/lpor.201800111

[60] W. Bogaerts, P. D. Heyn, T. V. Vaerenbergh, K. D. Vos, S. K. Selvaraja, T. Claes, P. Dumon, P. Bienstman, D. V. Thourhout, and R. Baets, "Silicon microring resonators," *Laser & Photonics Reviews*, vol. 6, no. 1, pp. 47–73, sep 2011. [Online]. Available: https://doi.org/10.1002/lpor.201100017

[61] J. Heebner, R. Grover, and T. Ibrahim, *Optical Microresonators: Theory, Fabrication and Applications*. Springer, 2008.

[62] A. Yariv, "Critical coupling and its control in optical waveguide-ring resonator systems," *IEEE Photonics Technology Letters*, vol. 14, no. 4, pp. 483–485, Apr. 2002. [Online]. Available: https://doi.org/10.1109/68.992585

[63] ——, "Universal relations for coupling of optical power between microresonators and dielectric waveguides," *Electronics Letters*, vol. 36, no. 4, p. 321, 2000. [Online]. Available: https://doi.org/10.1049/el:20000340

[64] L. Rayleigh, "CXII. the problem of the whispering gallery," *The London, Edinburgh, and Dublin Philosophical Magazine and Journal of Science*, vol. 20, no. 120, pp. 1001–1004, Dec. 1910. [Online]. Available: https://doi.org/10.1080/14786441008636993

[65] A. A. Savchenkov, A. B. Matsko, V. S. Ilchenko, I. Solomatine, D. Seidel, and L. Maleki, "Tunable optical frequency comb with a crystalline whispering gallery mode resonator," *Physical Review Letters*, vol. 101, no. 9, aug 2008. [Online]. Available: https://doi.org/10.1103/physrevlett.101.093902

[66] D. K. Armani, T. J. Kippenberg, S. M. Spillane, and K. J. Vahala, "Ultra-high-q toroid microcavity on a chip," *Nature*, vol. 421, no. 6926, pp. 925–928, Feb. 2003. [Online]. Available: https://doi.org/10.1038/nature01371

[67] L. He, Ş. K. Özdemir, and L. Yang, "Whispering gallery microcavity lasers," *Laser & Photonics Reviews*, vol. 7, no. 1, pp. 60–82, Feb. 2012. [Online]. Available: https://doi.org/10.1002/lpor.201100032

[68] G. C. Righini, Y. Dumeige, P. Feron, M. Ferrari, G. N. Conti, D. Ristic, and S. Soria, "Whispering gallery mode microresonators: Fundamentals and

applications," *La Rivista del Nuovo Cimento*, vol. 34, no. 7, p. 435488, Jun. 2011. [Online]. Available: http://doi.org/10.1393/ncr/i2011-10067-2

[69] J.-B. Jager, V. Calvo, E. Delamadeleine, E. Hadji, P. Noé, T. Ricart, D. Bucci, and A. Morand, "High-qsilica microcavities on a chip: From microtoroid to microsphere," *Applied Physics Letters*, vol. 99, no. 18, p. 181123, Oct. 2011. [Online]. Available: https://doi.org/10.1063/1.3658389

[70] N. Lin, L. Jiang, S. Wang, H. Xiao, Y. Lu, and H.-L. Tsai, "Design and optimization of liquid core optical ring resonator for refractive index sensing," *Applied Optics*, vol. 50, no. 20, p. 3615, jul 2011. [Online]. Available: https://doi.org/10.1364/ao.50.003615

[71] A. J. Trindade, B. Guilhabert, E. Y. Xie, R. Ferreira, J. J. D. McKendry, D. Zhu, N. Laurand, E. Gu, D. J. Wallis, I. M. Watson, C. J. Humphreys, and M. D. Dawson, "Heterogeneous integration of gallium nitride light-emitting diodes on diamond and silica by transfer printing," *Optics Express*, vol. 23, no. 7, p. 9329, apr 2015. [Online]. Available: https://doi.org/10.1364/oe.23.009329

[72] D.-H. Kim, J.-H. Ahn, W. M. Choi, H.-S. Kim, T.-H. Kim, J. Song, Y. Y. Huang, Z. Liu, C. Lu, and J. A. Rogers, "Stretchable and foldable silicon integrated circuits," *Science*, vol. 320, no. 5875, pp. 507–511, apr 2008. [Online]. Available: https://doi.org/10.1126/science.1154367

[73] D. Jevtics, A. Hurtado, B. Guilhabert, J. McPhillimy, G. Cantarella, Q. Gao, H. H. Tan, C. Jagadish, M. J. Strain, and M. D. Dawson, "Integration of semiconductor nanowire lasers with polymeric waveguide devices on a

mechanically flexible substrate," *Nano Letters*, vol. 17, no. 10, pp. 5990–5994, sep 2017. [Online]. Available: https://doi.org/10.1021/acs.nanolett.7b02178

[74] C. Di, W. Yan, S. Hu, D. Yin, and C. Ma, "Moiré-based absolute interferometry with large measurement range in wafer-mask alignment," *IEEE Photonics Technology Letters*, vol. 27, no. 4, pp. 435–438, feb 2015. [Online]. Available: https://doi.org/10.1109/lpt.2014.2377037

[75] L. Jiang, G. Pandraud, P. J. French, S. M. Spearing, and M. Kraft, "A novel method for nanoprecision alignment in wafer bonding applications," *Journal of Micromechanics and Microengineering*, vol. 17, no. 7, pp. S61–S67, jun 2007. [Online]. Available: https://doi.org/10.1088/0960-1317/17/7/s01

[76] E. Anderson, "Sub-pixel alignment for direct-write electron beam lithography," *Microelectronic Engineering*, vol. 73-74, pp. 74–79, jun 2004. [Online]. Available: https://doi.org/10.1016/s0167-9317(04)00076-0

[77] K. Docherty, S. Thoms, P. Dobson, and J. Weaver, "Improvements to the alignment process in a commercial vector scan electron beam lithography tool," *Microelectronic Engineering*, vol. 85, no. 5-6, pp. 761–763, may 2008. [Online]. Available: https://doi.org/10.1016/j.mee.2008.01.081

[78] S. W. Golomb and G. Gong, *Signal Design for Good Correlation*. Cambridge University Press, 2005. [Online]. Available: https://doi.org/10.1017/cbo9780511546907

[79] A. Dupont, K. Stirnnagel, D. Lindemann, and D. Lamb, "Tracking image correlation: Combining single-particle tracking and image correlation,"

Biophysical Journal, vol. 104, no. 11, pp. 2373–2382, jun 2013. [Online]. Available: https://doi.org/10.1016/j.bpj.2013.04.005

[80] K. Nandakumar and A. K. Jain, "Local correlation-based fingerprint matching," in *ICVGIP*, 2004.

[81] S. H. Lee, K.-N. Chen, and J. J.-Q. Lu, "Wafer-to-wafer alignment for three-dimensional integration: A review," *Journal of Microelectromechanical Systems*, vol. 20, no. 4, pp. 885–898, aug 2011. [Online]. Available: https://doi.org/10.1109/jmems.2011.2148161

[82] K. Docherty, K. Lister, J. Romijn, and J. Weaver, "High robustness of correlation-based alignment with penrose patterns to marker damage in electron beam lithography," *Microelectronic Engineering*, vol. 86, no. 4-6, pp. 532–534, apr 2009. [Online]. Available: https://doi.org/10.1016/j.mee.2008.11.037

[83] S. Thoms, D. S. Macintyre, K. E. Docherty, and J. M. Weaver, "Alignment verification for electron beam lithography," *Microelectronic Engineering*, vol. 123, pp. 9–12, jul 2014. [Online]. Available: https://doi.org/10.1016/j.mee.2014.02.005

[84] 1953.

[85] J. Juvert, T. Cassese, S. Uvin, A. de Groote, B. Snyder, L. Bogaerts, G. Jamieson, J. V. Campenhout, G. Roelkens, and D. V. Thourhout, "Integration of etched facet, electrically pumped, c-band fabry-pérot lasers on a silicon photonic integrated circuit by transfer printing," *Optics*

Express, vol. 26, no. 17, p. 21443, aug 2018. [Online]. Available: https://doi.org/10.1364/oe.26.021443

[86] J. Illingworth and J. Kittler, "The adaptive hough transform," *IEEE Transactions on Pattern Analysis and Machine Intelligence*, vol. PAMI-9, no. 5, pp. 690–698, Sep. 1987.

[87] B. Guilhabert, J. McPhillimy, S. May, C. Klitis, M. D. Dawson, M. Sorel, and M. J. Strain, "Hybrid integration of an evanescently coupled AlGaAs microdisk resonator with a silicon waveguide by nanoscale-accuracy transfer printing," *Optics Letters*, vol. 43, no. 20, p. 4883, oct 2018. [Online]. Available: https://doi.org/10.1364/ol.43.004883

[88] B. Guilhabert, A. Hurtado, D. Jevtics, Q. Gao, H. H. Tan, C. Jagadish, and M. D. Dawson, "Transfer printing of semiconductor nanowires with lasing emission for controllable nanophotonic device fabrication," *ACS Nano*, vol. 10, no. 4, pp. 3951–3958, mar 2016. [Online]. Available: https://doi.org/10.1021/acsnano.5b07752

[89] J. A. Alanis, D. Saxena, S. Mokkapati, N. Jiang, K. Peng, X. Tang, L. Fu, H. H. Tan, C. Jagadish, and P. Parkinson, "Large-scale statistics for threshold optimization of optically pumped nanowire lasers," *Nano Letters*, vol. 17, no. 8, pp. 4860–4865, jul 2017. [Online]. Available: https://doi.org/10.1021/acs.nanolett.7b01725

[90] W. Bogaerts, S. K. Selvaraja, P. Dumon, J. Brouckaert, K. D. Vos, D. V. Thourhout, and R. Baets, "Silicon-on-insulator spectral filters fabricated with CMOS technology," *IEEE Journal of Selected Topics in*

Quantum Electronics, vol. 16, no. 1, pp. 33–44, 2010. [Online]. Available: https://doi.org/10.1109/jstqe.2009.2039680

[91] Q. Xu, B. Schmidt, S. Pradhan, and M. Lipson, "Micrometre-scale silicon electro-optic modulator," *Nature*, vol. 435, no. 7040, pp. 325–327, may 2005. [Online]. Available: https://doi.org/10.1038/nature03569

[92] T.-Y. Liow, K.-W. Ang, Q. Fang, J.-F. Song, Y.-Z. Xiong, M.-B. Yu, G.-Q. Lo, and D.-L. Kwong, "Silicon modulators and germanium photodetectors on SOI: Monolithic integration, compatibility, and performance optimization," *IEEE Journal of Selected Topics in Quantum Electronics*, vol. 16, no. 1, pp. 307–315, 2010. [Online]. Available: https://doi.org/10.1109/jstqe.2009.2028657

[93] P. Dong, X. Liu, S. Chandrasekhar, L. L. Buhl, R. Aroca, and Y.-K. Chen, "Monolithic silicon photonic integrated circuits for compact 100+gb/s coherent optical receivers and transmitters," *IEEE Journal of Selected Topics in Quantum Electronics*, vol. 20, no. 4, pp. 150–157, Jul. 2014. [Online]. Available: https://doi.org/10.1109/jstqe.2013.2295181

[94] F. P. Payne and J. P. R. Lacey, "A theoretical analysis of scattering loss from planar optical waveguides," *Optical and Quantum Electronics*, vol. 26, no. 10, pp. 977–986, Oct 1994. [Online]. Available: https://doi.org/10.1007/BF00708339

[95] M. Gnan, S. Thoms, D. Macintyre, R. D. L. Rue, and M. Sorel, "Fabrication of low-loss photonic wires in silicon-on-insulator using hydrogen silsesquioxane electron-beam resist," *Electronics Letters*, vol. 44, no. 2, p. 115, 2008. [Online]. Available: https://doi.org/10.1049/el:20082985

[96] S. J. McNab, N. Moll, and Y. A. Vlasov, "Ultra-low loss photonic integrated circuit with membrane-type photonic crystal waveguides," *Opt. Express*, vol. 11, no. 22, pp. 2927–2939, Nov 2003. [Online]. Available: http://www.opticsexpress.org/abstract.cfm?URI=oe-11-22-2927

[97] T. Ikeda, Y. Kanamori, and K. Hane, "Si photonic nano-wire tunble micro-ring resonator composed of triply-liked variable couplers," in *2012 IEEE 25th International Conference on Micro Electro Mechanical Systems (MEMS)*. IEEE, jan 2012. [Online]. Available: https://doi.org/10.1109/memsys.2012.6170273

[98] M. J. Strain, C. Lacava, L. Meriggi, I. Cristiani, and M. Sorel, "Tunable q-factor silicon microring resonators for ultra-low power parametric processes," *Optics Letters*, vol. 40, no. 7, p. 1274, mar 2015. [Online]. Available: https://doi.org/10.1364/ol.40.001274

[99] Y. Fink, "A dielectric omnidirectional reflector," *Science*, vol. 282, no. 5394, pp. 1679–1682, nov 1998. [Online]. Available: https://doi.org/10.1126/science.282.5394.1679

[100] A. Fang, B. Koch, R. Jones, E. Lively, D. Liang, Y.-H. Kuo, and J. Bowers, "A distributed bragg reflector silicon evanescent laser," *IEEE Photonics Technology Letters*, vol. 20, no. 20, pp. 1667–1669, oct 2008. [Online]. Available: https://doi.org/10.1109/lpt.2008.2003382

[101] E. F. Schubert, Y.-H. Wang, A. Y. Cho, L.-W. Tu, and G. J. Zydzik, "Resonant cavity light-emitting diode," *Applied Physics Letters*, vol. 60, no. 8, pp. 921–923, feb 1992. [Online]. Available: https://doi.org/10.1063/1.106489

[102] S. Mariani, A. Andronico, A. Lemaître, I. Favero, S. Ducci, and G. Leo, "Second-harmonic generation in AlGaAs microdisks in the telecom range," *Optics Letters*, vol. 39, no. 10, p. 3062, may 2014. [Online]. Available: https://doi.org/10.1364/ol.39.003062

[103] F. Vollmer and S. Arnold, "Whispering-gallery-mode biosensing: label-free detection down to single molecules," *Nature Methods*, vol. 5, no. 7, pp. 591–596, jul 2008. [Online]. Available: https://doi.org/10.1038/nmeth.1221

[104] S. L. McCall, A. F. J. Levi, R. E. Slusher, S. J. Pearton, and R. A. Logan, "Whispering-gallery mode microdisk lasers," *Applied Physics Letters*, vol. 60, no. 3, pp. 289–291, jan 1992. [Online]. Available: https://doi.org/10.1063/1.106688

[105] M. Ghulinyan, R. Guider, G. Pucker, and L. Pavesi, "Monolithic whispering-gallery mode resonators with vertically coupled integrated bus waveguides," *IEEE Photonics Technology Letters*, vol. 23, no. 16, pp. 1166–1168, aug 2011. [Online]. Available: https://doi.org/10.1109/lpt.2011.2157487

[106] M. Borselli, T. J. Johnson, and O. Painter, "Beyond the rayleigh scattering limit in high-q silicon microdisks: theory and experiment," *Opt. Express*, vol. 13, no. 5, pp. 1515–1530, Mar 2005. [Online]. Available: http://www.opticsexpress.org/abstract.cfm?URI=oe-13-5-1515

[107] P. Kultavewuti, V. Pusino, M. Sorel, and J. S. Aitchison, "Low-power continuous-wave four-wave mixing wavelength conversion in AlGaAs-nanowaveguide microresonators," *Optics Letters*, vol. 40, no. 13, p. 3029, jun 2015. [Online]. Available: https://doi.org/10.1364/ol.40.003029

[108] M. Pu, L. Ottaviano, E. Semenova, and K. Yvind, "Efficient frequency comb generation in AlGaAs-on-insulator," *Optica*, vol. 3, no. 8, p. 823, jul 2016. [Online]. Available: https://doi.org/10.1364/optica.3.000823

[109] A. C. Turner, M. A. Foster, A. L. Gaeta, and M. Lipson, "Ultra-low power parametric frequency conversion in a silicon microring resonator," *Optics Express*, vol. 16, no. 7, p. 4881, mar 2008. [Online]. Available: https://doi.org/10.1364/oe.16.004881

[110] M. Ferrera, D. Duchesne, L. Razzari, M. Peccianti, R. Morandotti, P. Cheben, S. Janz, D.-X. Xu, B. E. Little, S. Chu, and D. J. Moss, "Low power four wave mixing in an integrated, micro-ring resonator with q = 12 million," *Optics Express*, vol. 17, no. 16, p. 14098, jul 2009. [Online]. Available: https://doi.org/10.1364/oe.17.014098

[111] D. J. Moss, R. Morandotti, A. L. Gaeta, and M. Lipson, "New CMOS-compatible platforms based on silicon nitride and hydex for nonlinear optics," *Nature Photonics*, vol. 7, no. 8, pp. 597–607, aug 2013. [Online]. Available: https://doi.org/10.1038/nphoton.2013.183

[112] C. Lacava, S. Stankovic, A. Z. Khokhar, T. D. Bucio, F. Y. Gardes, G. T. Reed, D. J. Richardson, and P. Petropoulos, "Si-rich silicon nitride for nonlinear signal processing applications," *Scientific Reports*, vol. 7, no. 1, Feb. 2017. [Online]. Available: https://doi.org/10.1038/s41598-017-00062-6

[113] U. D. Dave, B. Kuyken, F. Leo, S.-P. Gorza, S. Combrie, A. D. Rossi, F. Raineri, and G. Roelkens, "Nonlinear properties of dispersion engineered InGaP photonic wire waveguides in the telecommunication wavelength range,"

Optics Express, vol. 23, no. 4, p. 4650, feb 2015. [Online]. Available: https://doi.org/10.1364/oe.23.004650

[114] C. Lacava, M. J. Strain, P. Minzioni, I. Cristiani, and M. Sorel, "Integrated nonlinear mach zehnder for 40 gbit/s all-optical switching," *Optics Express*, vol. 21, no. 18, p. 21587, sep 2013. [Online]. Available: https://doi.org/10.1364/oe.21.021587

[115] R. Salem, M. A. Foster, D. F. Geraghty, A. L. Gaeta, A. C. Turner, and M. Lipson, "Low-power optical regeneration using four-wave mixing in a silicon chip," in *OFC/NFOEC 2008 - 2008 Conference on Optical Fiber Communication/National Fiber Optic Engineers Conference*. IEEE, feb 2008. [Online]. Available: https://doi.org/10.1109/ofc.2008.4528727

[116] K. Dolgaleva, W. C. Ng, L. Qian, and J. S. Aitchison, "Compact highly-nonlinear AlGaAs waveguides for efficient wavelength conversion," *Optics Express*, vol. 19, no. 13, p. 12440, jun 2011. [Online]. Available: https://doi.org/10.1364/oe.19.012440

[117] D. K. Schroder, R. N. Thomas, and J. C. Swartz, "Free carrier absorption in silicon," *IEEE Journal of Solid-State Circuits*, vol. 13, no. 1, pp. 180–187, Feb 1978.

[118] R. W. Boyd, *Nonlinear Optics, Third Edition*, 3rd ed. Orlando, FL, USA: Academic Press, Inc., 2008.

[119] I. D. Rukhlenko, M. Premaratne, and G. P. Agrawal, "Effective mode area and its optimization in silicon-nanocrystal waveguides," *Optics*

Letters, vol. 37, no. 12, p. 2295, Jun. 2012. [Online]. Available: https://doi.org/10.1364/ol.37.002295

[120] G. P. Agrawal, "Nonlinear fiber optics," in *Nonlinear Science at the Dawn of the 21st Century*. Springer Berlin Heidelberg, pp. 195–211. [Online]. Available: https://doi.org/10.1007/3-540-46629-0_9

[121] J. J. Wathen, P. Apiratikul, C. J. K. Richardson, G. A. Porkolab, G. M. Carter, and T. E. Murphy, "Efficient continuous-wave four-wave mixing in bandgap-engineered AlGaAs waveguides," *Optics Letters*, vol. 39, no. 11, p. 3161, may 2014. [Online]. Available: https://doi.org/10.1364/ol.39.003161

[122] V. Van, T. Ibrahim, K. Ritter, P. Absil, F. Johnson, R. Grover, J. Goldhar, and P.-T. Ho, "All-optical nonlinear switching in GaAs-AlGaAs microring resonators," *IEEE Photonics Technology Letters*, vol. 14, no. 1, pp. 74–76, jan 2002. [Online]. Available: https://doi.org/10.1109/68.974166

[123] J. Aitchison, D. Hutchings, J. Kang, G. Stegeman, and A. Villeneuve, "The nonlinear optical properties of AlGaAs at the half band gap," *IEEE Journal of Quantum Electronics*, vol. 33, no. 3, pp. 341–348, mar 1997. [Online]. Available: https://doi.org/10.1109/3.556002

[124] J. Leuthold, C. Koos, and W. Freude, "Nonlinear silicon photonics," *Nature Photonics*, vol. 4, no. 8, pp. 535–544, jul 2010. [Online]. Available: https://doi.org/10.1038/nphoton.2010.185

[125] G. Cantarella and M. Strain, "A micro-processor-based feedback stabilization scheme for high-q, non-linear silicon resonators," *Applied Sciences*, vol. 6,

no. 11, p. 316, oct 2016. [Online]. Available: https://doi.org/10.3390/app6110316

[126] X. Cai, J. Wang, M. J. Strain, B. Johnson-Morris, J. Zhu, M. Sorel, J. L. O'Brien, M. G. Thompson, and S. Yu, "Integrated compact optical vortex beam emitters," *Science*, vol. 338, no. 6105, pp. 363–366, Oct. 2012. [Online]. Available: https://doi.org/10.1126/science.1226528

[127] P. Del'Haye, A. Schliesser, O. Arcizet, T. Wilken, R. Holzwarth, and T. J. Kippenberg, "Optical frequency comb generation from a monolithic microresonator," *Nature*, vol. 450, no. 7173, pp. 1214–1217, Dec. 2007. [Online]. Available: https://doi.org/10.1038/nature06401

[128] C. H. Bennett and D. P. DiVincenzo, "Quantum information and computation," *Nature*, vol. 404, no. 6775, pp. 247–255, Mar. 2000. [Online]. Available: https://doi.org/10.1038/35005001

[129] H. Clevenson, M. E. Trusheim, C. Teale, T. Schröder, D. Braje, and D. Englund, "Broadband magnetometry and temperature sensing with a light-trapping diamond waveguide," *Nature Physics*, vol. 11, no. 5, pp. 393–397, Apr. 2015. [Online]. Available: https://doi.org/10.1038/nphys3291

[130] M. Davanco, J. Liu, L. Sapienza, C.-Z. Zhang, J. V. D. M. Cardoso, V. Verma, R. Mirin, S. W. Nam, L. Liu, and K. Srinivasan, "Heterogeneous integration for on-chip quantum photonic circuits with single quantum dot devices," *Nature Communications*, vol. 8, no. 1, Oct. 2017. [Online]. Available: https://doi.org/10.1038/s41467-017-00987-6

[131] A. W. Elshaari, I. E. Zadeh, A. Fognini, M. E. Reimer, D. Dalacu, P. J. Poole, V. Zwiller, and K. D. Jöns, "On-chip single photon filtering and multiplexing in hybrid quantum photonic circuits," *Nature Communications*, vol. 8, no. 1, Aug. 2017. [Online]. Available: https://doi.org/10.1038/s41467-017-00486-8

[132] A. Fallahkhair, K. S. Li, and T. E. Murphy, "Vector finite difference modesolver for anisotropic dielectric waveguides," *J. Lightwave Technol.*, vol. 26, no. 11, pp. 1423–1431, Jun 2008. [Online]. Available: http://jlt.osa.org/abstract.cfm?URI=jlt-26-11-1423